A STUDY OF HIGH TRANSVERSE MOMENTUM ELECTRONS PRODUCED IN HIGH ENERGY PROTON-ANTIPROTON COLLISIONS

by
David Robinson

A thesis submitted for the degree of Doctor of Philosophy
and the Diploma of Membership of Imperial College

January 1988

Imperial College
London

Abstract

This thesis describes a study of high transverse momentum electron production using data taken by the UA1 experiment at the CERN SPS collider. The data were taken at a centre of mass energy of 546 GeV and 630 GeV, and correspond to an integrated luminosity of 690nb^{-1}. The fluctuation of a QCD jet into a single charged pion and neutral particles forms the dominant background to electron identification. The second source of background is the asymmetric conversion of high-P_t photons into electron-positron pairs within the material of the UA1 apparatus. The cuts used to enhance the electron signal are listed and the methods of estimating the background contributions are described. The rate and properties of the data have been compared directly with Monte Carlo predictions for the Drell-Yan process, J/ψ and Υ production, the leptonic decays of the W and Z Intermediate Vector Bosons, and the semileptonic decays of heavy flavours. The data sample is in good agreement with Monte Carlo predictions without the need to include contributions from top quark production. However, statistics are poor because the cuts impose a bias against all processes except for W and Z production, and the non-IVB processes are not easily distinguishable because the cuts impose a topological bias. In particular, the electron sample is unsuited to studies of J/ψ, Υ and heavy flavour production, but the sample should be sensitive to the top quark signal given more statistics and if the top mass is not too large.

Acknowledgments

I would like to thank all my colleagues in the High Energy Physics group at Imperial College for their friendliness and help. The many friends I made at Imperial College amongst the students and the technical, computing and academic staff helped to make life a lot of fun during my studentship. I would like to thank G. Hall, C.Seez, I. Siotis, T.S. Virdee and T. Wildish for their help and advice during the past three years. I would particularly like to thank D.M. Binnie for allowing me to join the HEP group and giving me the opportunity to make use of the unique facilities at both Imperial College and CERN.

It would be impossible to list here all the members of the UA1 Collaboration who have been helpful to me during my stay at CERN. I gratefully acknowledge the help of the many colleagues I worked with in the Uranium-scintillator calorimeter prototype group (1985), the Uranium-TMP calorimeter prototype group (1986) and the UA1 trigger group. I would like to thank N. Ellis and M. N. Minard for their suggestions of a suitable thesis topic. I. Wingerter has been particularly helpful during the analysis of electron data for this thesis.

I would also like to acknowledge the financial support of the Science and Engineering Research Council and of Imperial College during my studentship.

Finally, I would like to thank my mother and father for their love and support.

To my Mother and Father

CONTENTS

TABLES

FIGURES

1. INTRODUCTION

1.1 History of the UA1 Experiment

The traditional mode of operation of the Super Proton Synchrotron (SPS) at CERN is to accelerate protons to a momentum of 450 GeV/c and then release them on to a fixed target giving a centre of mass energy ($\sqrt{s}$) available for new particle creation of only about 29 GeV. In 1976 a proposal [1] was made to run the SPS as a proton-antiproton collider in which bunches of protons collide at various regions around the SPS ring with counter-rotating bunches of antiprotons. For colliders the centre of mass energy is equal to the sum of the energies of the two incident particles, so the SPS in a collider mode could potentially reach a $\sqrt{s}$ of 900 GeV. It was therefore hoped that the SPS as a collider would lead to an exploration of several crucial issues of the time, such as the predicted existence of the W and Z weak bosons which were thought to have masses of up to 100 GeV. In a pulsed mode the SPS beams can indeed reach 450 GeV/c giving a $\sqrt{s}$ of 900 GeV, but from the first short run in December 1981 and up to the end of 1983, continuous running of the collider overheated the SPS guiding magnets and limited the beam momentum to 273 GeV/c giving $\sqrt{s} = 546$ GeV. In the collider runs of 1984 and 1985, cooling to the magnets was improved and a $\sqrt{s}$ of 630 GeV could be attained.

The UA1 (Underground Area One) experiment is situated at one of the proton-antiproton collision points of the SPS ring, and is a general purpose detector designed to investigate the new high energy region of the SPS collider. The UA1 detector is shown in Figure 1.

In the UA1 proposal [2] several physics objectives were mentioned, but the principal aim was to search for evidence of the charged ($W^{\pm}$) and neutral (Z^0) Intermediate Vector Bosons (IVBs). The existence of the IVBs was firmly established during the collider runs of 1982 and 1983 by the discovery of candidates of their leptonic decays to electrons or muons. The discovery has proved to be perhaps the greatest success of the collider

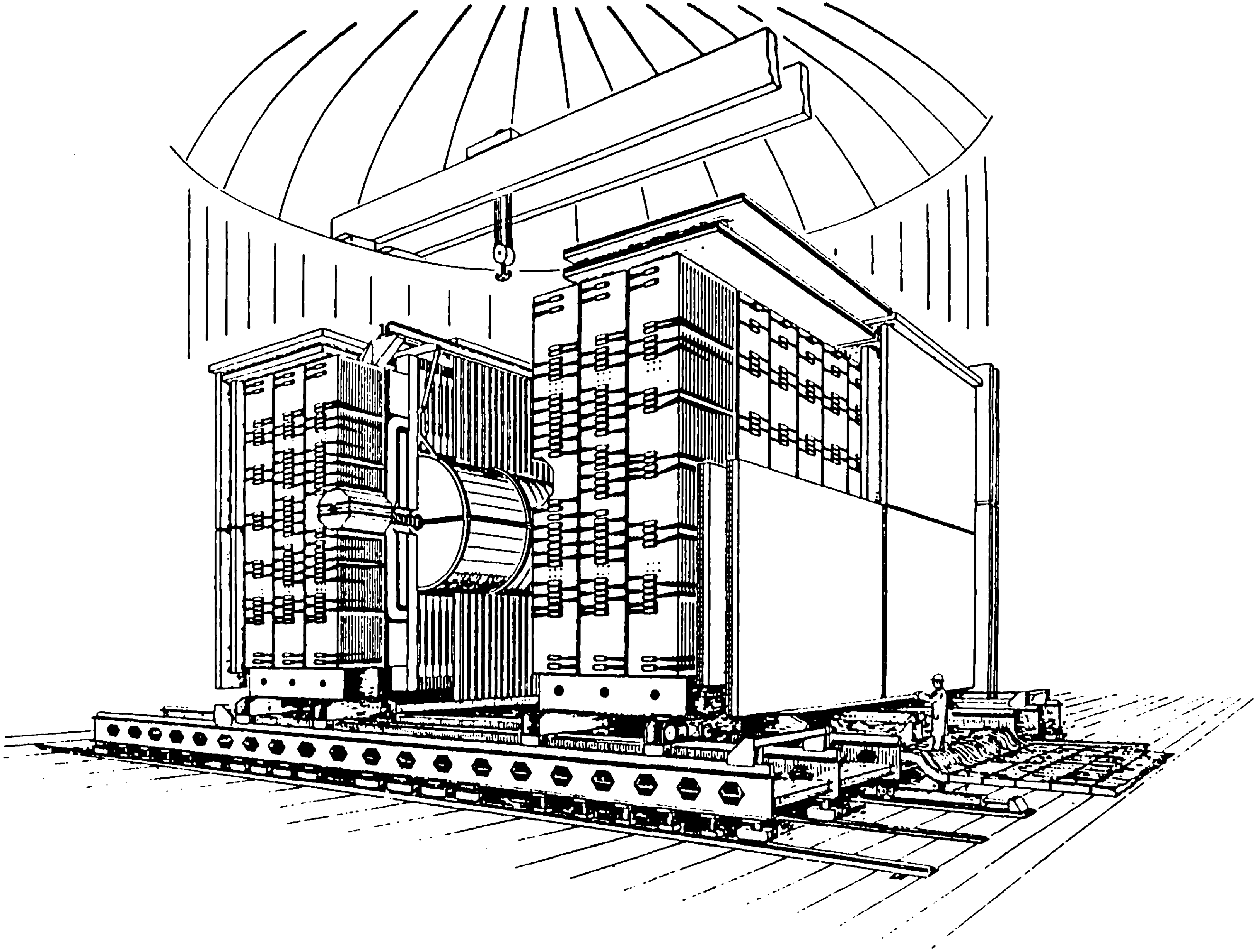

Figure 1: The UA1 Experiment

project, and has provided powerful evidence in support of the electroweak theory [3] which combines the electromagnetic and weak interactions. By the end of the collider run in 1985, both UA1 and UA2 (a second $p\bar{p}$ experiment on the SPS ring) had accumulated large numbers of $W^{\pm}$ and Z^0 candidates, and the masses of the IVBs and their kinematical properties could be determined with reasonable statistics.

Another physics objective for the SPS collider was the extrapolation of strong interaction data taken from pp collisions at the CERN Intersecting Storage Ring (ISR) taken at $\sqrt{s} = 63$ GeV. A striking feature of the new high energy region of $p\bar{p}$ collisions was the emergence of sprays, or jets, of particles with a large component of their momentum transverse to the beam axis. The SPS collider has proved to be a rich source of strong interaction physics because at the collider energies the proton and antiproton can be considered as systems consisting of quarks, antiquarks and gluons (collectively called partons). There is no evidence of any substructure to quarks, so the $p\bar{p}$ collisions can be described in terms of the scattering between two partons which subsequently fragment to form jets of particles in the final state. Studies of jet production properties have therefore provided valuable tests of perturbative QCD that were not possible at the ISR because the low energy 2-jet structure was obscured by the debris from the fragmentation of other partons in the event.

There was also hope that the heavy top quark might be discovered at the SPS collider provided the mass of the quark is not too large. However, it was recognised that the signal for top quark production would be difficult to extract from the data, and an analysis of the full UA1 data sample has not revealed any clear evidence for top production. A diversity of other physics topics have been investigated by the UA1 Collaboration, but a discussion of all these studies would be beyond the scope of this thesis. Central to many of these achievements though is a study of the properties of lepton production.

1.2 This Thesis

This thesis details the author's contributions to the analysis of data from the UA1 experiment. The cross-section for high energy parton-parton scattering is dominated by the QCD production of two jets in the final state, and it is therefore difficult to distinguish different physics processes purely by a study of jet production. The best hope of distinguishing between different processes is to search for evidence of their leptonic decay modes. The thesis describes an inclusive study of events containing an isolated, high transverse momentum electron candidate in the data taken by the UA1 experiment during the CERN SPS collider runs of 1983, 1984 and 1985. The motivation for this study is to determine whether the number of electron candidates and their properties are in agreement with expectations from the Standard Model processes.

Chapter 2 reviews some basic principles of particle physics as an introduction to the physics of proton-antiproton collisions. In particular the sources of high transverse momentum lepton production are discussed.

Chapter 3 introduces the complex array of detectors that together comprise the UA1 experiment. The operation of the detectors and the processing of data is described.

Chapter 4 describes the procedure for identifying electron candidates in the UA1 data and discusses the cuts that are necessary to optimise the electron signal. The methods of estimating the background to the electron signal from electron misidentification are described.

Chapter 5 details the analysis of UA1 events that pass the electron selection criteria. A Monte Carlo prediction of the properties and rates of known processes that lead to electron production from $p\bar{p}$ collisions is described. Features of the inclusive data in various kinematical distributions are then compared directly with Monte Carlo predictions, and an attempt is made to distinguish between candidates of each of the Standard Model electron production channels.

During his studentship, the author worked predominantly on the program of upgrading the UA1 electromagnetic calorimeters [4]. In 1985 the author worked on the design, construction and testing in CERN test-beams of a photodiode-scintillator position detector prototype [5] [6], and was a member of the team responsible for testing a Uranium-scintillator calorimeter prototype [7]. Throughout 1986 the author worked on the testing and calibration of Uranium-TMP calorimeter prototypes in CERN test-beams [8]. However, the details of these projects have been published elsewhere and have therefore not been included in this thesis.

2. THEORETICAL BACKGROUND

2.1 Introduction

There are many detailed reviews of the physics of high energy proton-antiproton collisions [9] [10] [11]. This chapter presents a largely qualitative summary of the physics processes relevant to high transverse momentum lepton production in $p\bar{p}$ collisions. It is instructive to begin with a review of some basic principles of particle physics. As an introduction to $p\bar{p}$ collisions, the structure of the proton and the parton model are discussed. An attempt is then made to show how perturbative QCD can be used to calculate cross-sections for inclusive particle production. Finally, the sources of lepton production in $p\bar{p}$ collisions are reviewed.

2.2 Basic Principles in Particle Physics

2.2.1 Quarks and Colour

There is now overwhelming experimental evidence (partly discussed in section 2.3) that hadrons are made from smaller particles called quarks. Historically, the idea of quarks dates back to 1964 when Gell-Mann [12] and Zweig [13] proposed an underlying SU(3) symmetry whereby baryons are made up from bound states of three quarks or antiquarks (qqq or $\overline{qqq}$) and mesons are made up from bound states of a quark and an antiquark ($q\bar{q}$). For example, the proton and the π^+ meson are composed of the uud and $u\bar{d}$ bound states repectively, where u and d refer to the 'up' and 'down' quark flavours. The additive quantum numbers of the quarks must match the conserved quantum numbers of the parent hadron, so the quarks have fractional charge ($Q(u)=2/3, Q(d)=-1/3$) and baryon number ($B = 1/3$). Moreover, the hypothesis that quarks are fermions with $J = 1/2$ accomodates the observed separation of hadrons into baryons ($J = 1/2$ or $J = 3/2$ qqq fermion states) and mesons ($J = 0$ or 1 $q\bar{q}$ boson states).

However, the quark scheme ran into difficulties in the attempt to explain the Δ^{++} baryon, a uuu bound state, because the $J=3/2$ nature of the Δ^{++} forces the quark scheme to combine the three u quarks in a completely symmetric ground state, which is forbidden by Fermi-Dirac statistics. There were other discrepancies in the quark hypothesis: the quark scheme did not exclude bound states like qq or $\overline{qq}$, but these have never been observed by experiment. All these apparent discrepancies were resolved by the introduction of a new property called 'colour'. Quarks have three primary colours, sometimes called red, green and blue (R,G,B). The Δ^{++} is in fact a bound state of $u_R u_G u_B$: the three quarks are therefore distinguishable according to the rules of Fermi-Dirac statistics. The colour scheme excludes non-observed states like qq by asserting that all particles observable by experiment are colourless or 'white'. Baryons are colourless because they contain a red, a blue and a green quark (the proton is a $u_R u_G d_B$ state with permutations in RGB), and mesons of course carry both colour and anticolour (the π is a $R\bar{R}+B\bar{B}+G\bar{G}$ state).

2.2.2 The Strong and Electromagnetic Interactions

Forces of nature are explained by Quantum Field Theory in terms of particle exchange. Figure 2 depicts two electrons repelled via the exchange of a photon.

One of the electrons emits the photon and recoils in order to conserve momentum. However, energy is not conserved and the photon is 'virtual' in the sense that it can only live for a short time governed by the uncertainties inherent in quantum mechanics, given by $\tau \leq \hbar/\Delta E$ where ΔE is the photon energy. The second electron absorbs the virtual photon and is recoiled, the net result being an exertion of a force between the two electrons.

Analogous to the electromagnetic process described above, the interaction between two quarks proceeds via the exchange of a virtual gluon as depicted in Figure 3(a). Gluons are the quanta of the colour field, the so-called strong force, that binds quarks

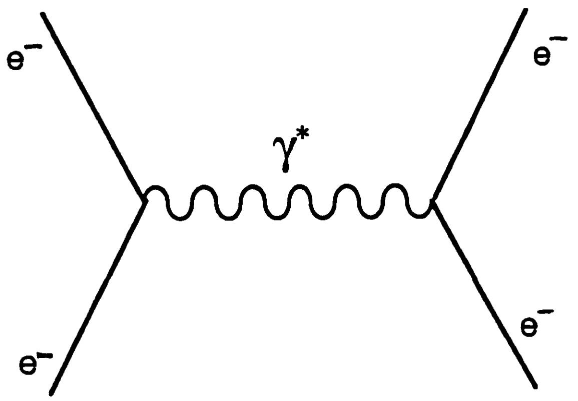

Figure 2: Repulsion of two electrons via exchange of virtual photon

together. Gluons are bi-coloured ($g = \bar{G}R$ in the example of Figure 3(b)) and exchange colour between quarks. It then follows from Figure 4 that, unlike the virtual photon which has zero electric charge, the colour content of the gluon enables it to couple directly with other gluons.

The quantization of the electromagnetic and strong interactions has been accomplished by the theories of Quantum Electrodynamics (QED) and Quantum Chromodynamics (QCD) respectively. The scattering between two particles can be represented by Feynman diagrams, which form a basis for calculating the amplitude and thus the probability for the two particles to interact. A Feynman diagram depicting the exchange of a gluon between two quarks is shown in Figure 5.

Each vertex in a Feynman diagram is characterised by a coupling, α. The probability of the interaction is given by the square of the amplitude for the diagram, and is proportional to the product of the couplings at each vertex. Feynman diagrams may contain extra vertices, so the total probability for the process is obtained by forming diagrams in

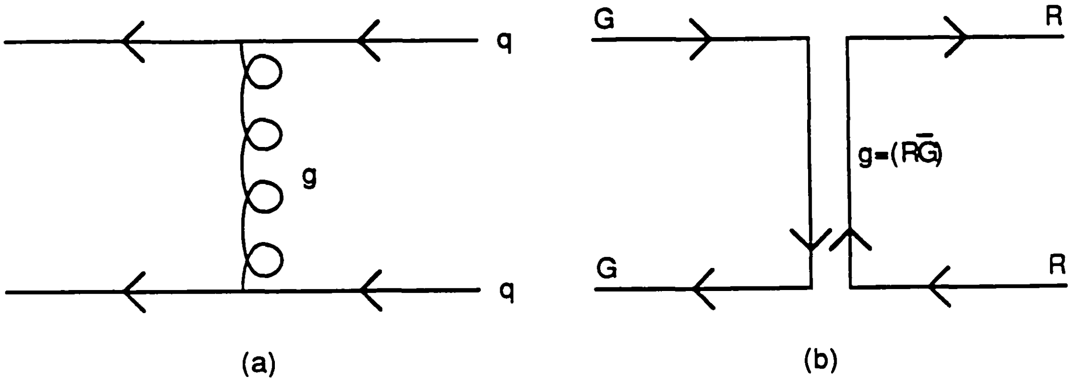

Figure 3: Exchange of a virtual gluon between two quarks

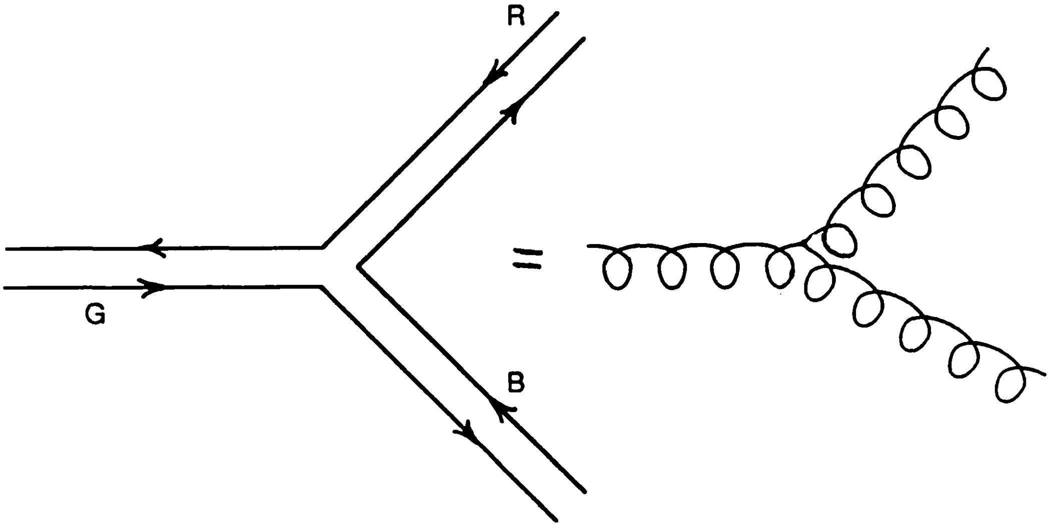

Figure 4: The gluon-gluon coupling

which the two primary vertices are connected in all possible ways, and squaring the sum of the amplitudes from each diagram. There can be an infinite number of such diagrams,

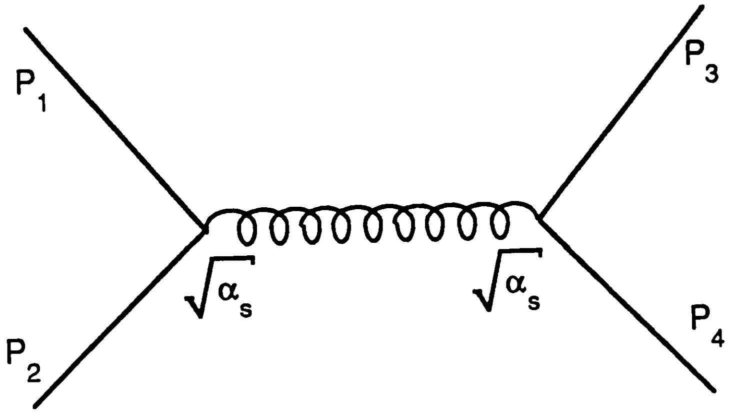

Figure 5: A lowest order Feynman diagram

but in QED the electromagnetic coupling is small ($\alpha_{em} \simeq 1/137$) so the total amplitude for, say, e^+e^- scattering can be accurately calculated by considering only a few diagrams.

In contrast, the coupling of the strong interaction, α_s, is large and it is difficult to make an accurate calculation of amplitudes. However the phenomenon known as 'asymptotic freedom' permits perturbative calculations that can provide workable approximations.

2.2.3 Asymptotic Freedom

There are significant differencies between QED and QCD in the effects of charge screening. In Quantum Field Theory the electric field surrounding an electron can be envisaged as the large scale manifestation of the emission and re-absorption of virtual photons. The photons can themselves produce virtual electron-positron pairs, so the original electron is surrounded by a cloud of polarised e^+e^- pairs in which the positrons tend to be aligned towards the electron. The charge of the electron is therefore screened. In Figure 6, an attempt is made to determine the electron charge by measuring the force exerted on a test charge. The charge measured is dependent on the distance between the electron and test charge: as the test charge approaches the electron and penetrates deeper into the polarised cloud of e^+e^- pairs, the effects of charge screening are reduced and the measured electron charge is larger. In other words, the electromagnetic coupling, α_{em}, is large for high-energy, short distance probes, but with decreasing energy and increasing interaction distance, α_{em} asymptotically approaches a constant value ($\simeq 1/137$).

In close analogy with the screening of the electron charge, the colour charge of a quark is screened by a cloud of virtual gluons and $q\bar{q}$ pairs. However, an important consequence of the fact that gluons can couple into gg as well as $q\bar{q}$ pairs is that the QED results are reversed: the polarisation of the colour vacuum is such that a red charge is preferentially surrounded by other red charges. Therefore it is the low energy, long distance probes for which the strong coupling, α_s, is large. As the energy of the test charge is increased and it probes shorter distancies, α_s asymptotically approaches a small value. This phenomenon whereby at high energy two quarks interact with reduced strength and therefore appear to be free is known as asymptotic freedom.

2.2.4 Quark Confinement

Colour screening also provides an explanation for why free quarks have never been observed by experiment. A consequence of the ability of gluons to interact discretely with other gluons is that the colour field lines between two quarks are squeezed into a tube-like shape (Figure 7). This contrasts with the electric field between an e^+e^- pair (Figure 8) in which the photons have no self-coupling and the field lines are spread out. Separating the two quarks increases the strong coupling between them, and if the colour tube has a constant energy density per unit length, the potential energy between the two quarks will increase with separation. Quarks (and gluons) are therefore confined, a phenomenon known as infra-red slavery.

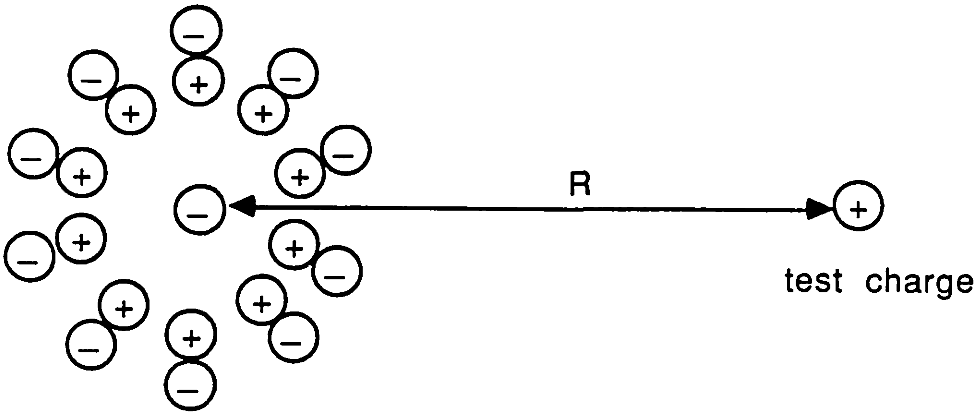

(a) Using a long-distance (low energy) probe

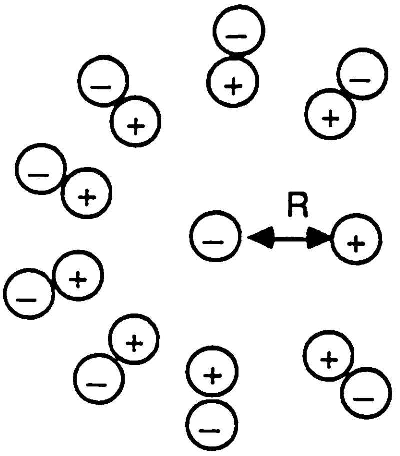

(b) Using a short-distance (high energy) probe

Figure 6: Measuring the electric charge of an electron

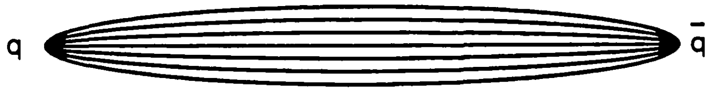

Figure 7: The field lines between two quarks

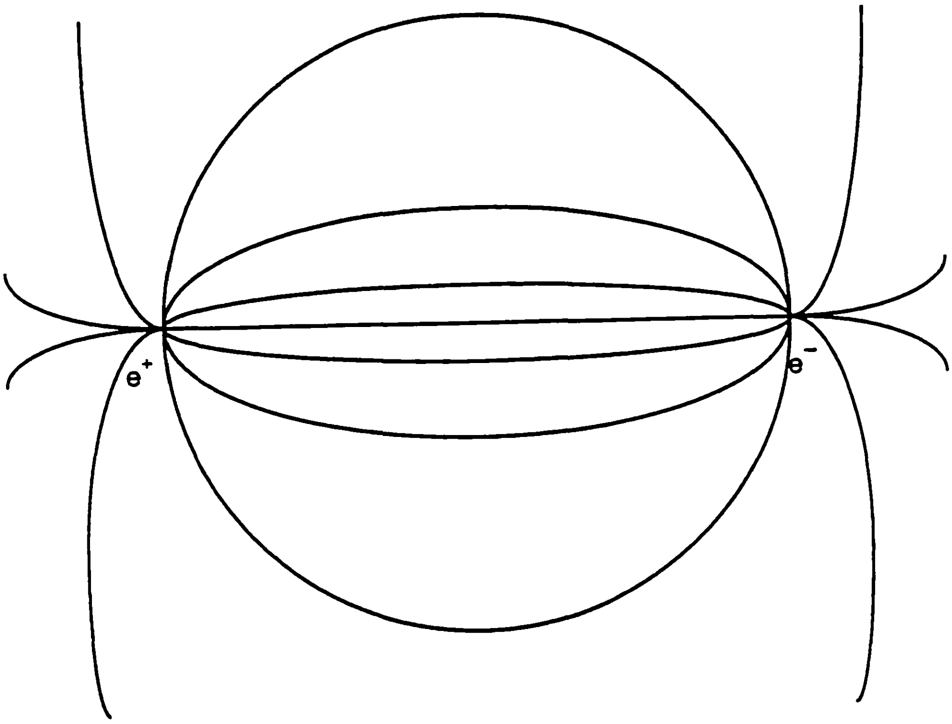

Figure 8: The field lines between an electron and a positron

If two quarks are given sufficient energy to separate such that α_s between them becomes large, the quarks can manifest themselves as experimentally observable sprays, or jets, of hadrons. The process is represented by Figure 9.

As the quarks separate, the increasing potential energy in the colour tube becomes sufficient to create a $q\bar{q}$ pair. The new $q\bar{q}$ pair effectively cuts the tube into two shorter tubes with a lower net energy. If there is sufficient energy, the colour field lines are stretched further and more $q\bar{q}$ pairs are created until the kinetic energy of the original $q\bar{q}$ pair has been used up. The net result is clusters of quarks and gluons, each with zero net colour, that can form jets of hadrons observable by experiment.

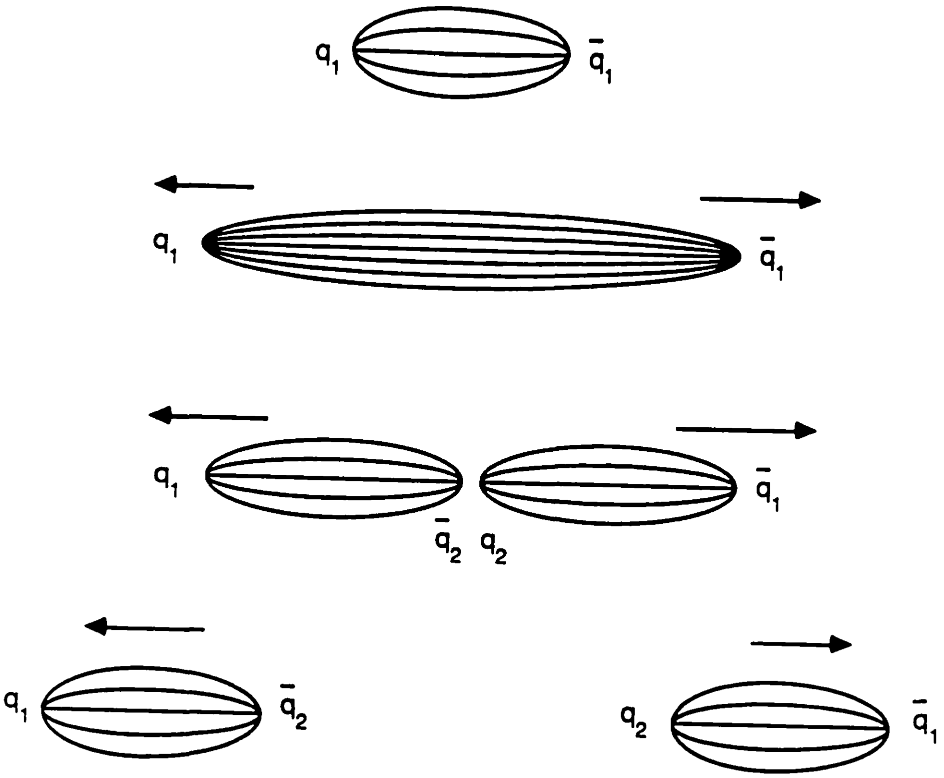

Figure 9: The quark confinement mechanism

2.2.5 Weak Interactions

The increase of the value of α_S with increasing distance between two strongly interacting particles suggest a characteristic range, or scale, to the strong interaction of about 1 fermi (10^{-13}cm). For example, the lifetime of the Δ^{++} resonance (which is formed by $p\pi^+$ scattering and decays via the strong interaction back to a p and π^+) is the time that the p and π^+ take to separate by about 1 fermi, given by

$$\tau = R/c \sim 10^{-23} \text{ seconds}$$

The scale of an interaction therefore characterises decay lifetimes. The scale of the strong interaction defines the lifetime of strong decays to be typically 10^{-23} secs. In contrast, electromagnetic decays have much longer lifetimes ($\sim 10^{-16}$ secs) because of the larger range of the electromagnetic interaction.

The existence of the weak interaction is experimentally evident by the very long lifetimes of radioactive decays (for example the neutron decay $n \rightarrow p + e^- + \bar{\nu}$ has a 15 minute lifetime). The weak interaction was parameterised at low energies by Fermi in the 1930s, and quantised at high energies by the electroweak theory [3]. The quanta of the weak interaction are the $W^{\pm}$ and Z^0, the so-called Intermediate Vector Bosons. Weak interactions can exchange electric charge, and change the flavour of the interacting particles.

The electroweak theory has unified the electromagnetic and weak interactions, and the nature of the weak field can be visualised as being essentially the same as that for the electromagnetic interaction. The difference is that the weak quanta are massive ($M \sim 100$ GeV/c^2). The virtual IVBs are therefore re-absorbed quickly and have a very short range.

2.2.6 The Elementary Fermions and Forces of Nature

To conclude this section, the elementary fermions and the forces of nature are listed in Tables 1 and 2 respectively. The existence of the heaviest flavour, top, is yet to be verified experimentally. Gravity has been included in Table 2 for completeness though it is too weak to have any relevance to the work in this thesis.

2.3 The Parton Model

The first experimental evidence that the proton has a substructure consisting of a number of point-like particles came from deep inelastic lepton scattering. Experiments were performed at SLAC in the 1960s that involved scattering electrons off protons in liquid hydrogen, in which the electron interacts with the proton via the exchange of a virtual photon (Figure 10).

Table 1: The elementary fermions

Charge	The Family of Quarks		
$+2/3$	u(up)	c(charm)	t(top)
$-1/3$	d(down)	s(strange)	b(bottom)

Charge	The Family of Leptons		
-1	e^-(electron)	μ^-(muon)	τ^-(tau)
0	ν_e	ν_μ	ν_τ

Table 2: The forces of nature

Force	Quanta	Typical Coupling(α)
Strong	Gluon	1
Electromagnetic	Photon	10^{-2}
Weak	$W^\pm,Z^0$	10^{-6}
Gravity	Graviton	10^{-38}

At low energy the virtual photon can do little more then determine that the proton has a charge and a magnetic moment. With increasing energy the photon begins to resolve the cloud of virtual pions that surrounds the proton, which then appears as a composite object. At still higher energy, the photon wavelength becomes sufficiently short to resolve the quarks within the proton. The structure function of the proton then becomes independent of any increasing energy transfer (but see section on QCD corrections), and is a function only of the dimensionless fraction of the proton energy carried by the struck quark. This phenomenon is called Bjorken scaling.

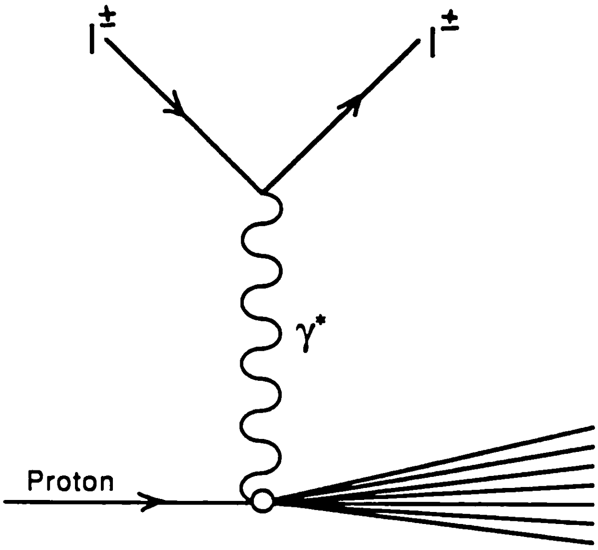

Figure 10: Deep inelastic lepton scattering

A quantitative treatment of deep inelastic lepton scattering can be made using the parton model, which asserts that the proton contains point-like 'partons' that each carry a different fraction x of the parent proton's energy and momentum. The parton momentum distribution, defined as $f_i(x) = dP_i/dx$, describes the probability that a struck parton i carries a fraction x of the proton momentum. The sum of the fractions x must add to 1:

$$\sum_i \int_0^1 dx\ x f_i(x) = 1$$

In the parton model, the interaction time between the photon and parton is much shorter than the time scale in which partons can interact with one another. This is implicit in the assumption by the parton model that the parton motion transverse to the proton direction of motion is negligible and the proton is moving with infinite momentum.

Relativistic time dilation therefore slows down the rate at which partons interact with each other. This picture is valid provided the energy transfer of the virtual photon is large.

The partons that can interact with the photon are of course physically associated with the three valence quarks (uud), and a sea of $q\bar{q}$ pairs that are created in the rapidly fluctuating colour fields. The quark structure functions can be extracted from an analysis of deep inelastic scattering data, and are shown for different flavours in Figure 11(a) [10]. Figure 11(b) shows the sum of contributions from all valence and sea quarks.

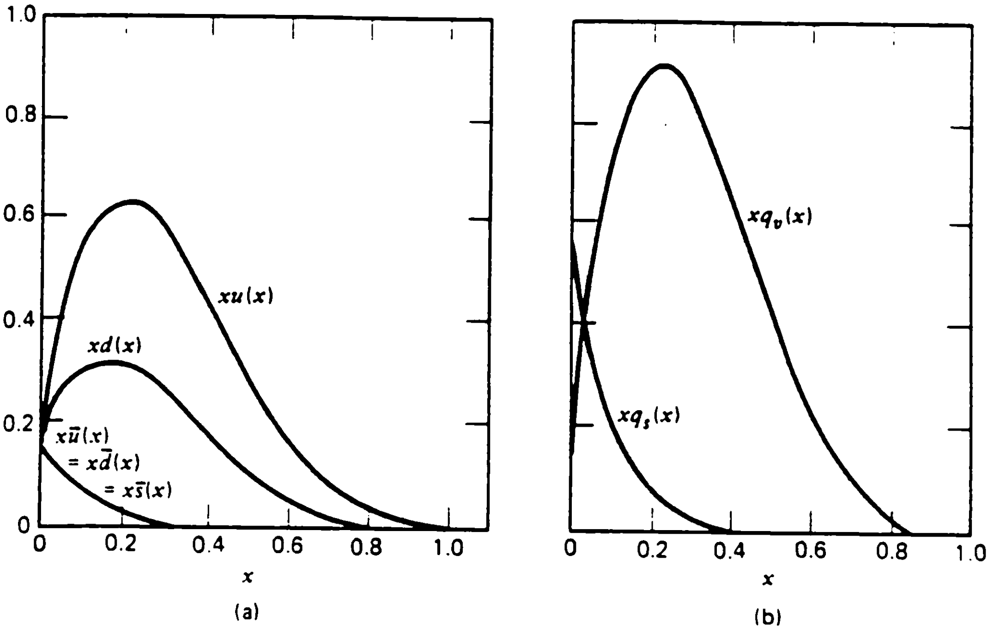

Figure 11: Quark structure functions inside the proton

The structure functions for the 3 valence quarks have a peak towards x = 1/3, but are smeared out because the quarks can exchange momenta via the exchange of gluons. The slow debris of sea quarks forms a peak towards zero in x. Gluons are invisible to the electromagnetic interaction, but integrating over the structure functions shows that gluons carry about 50% of the proton momentum.

2.4 Proton-Antiproton Collisions

2.4.1 Parton-Parton Scattering

In order to make any quantitative predictions about the QCD scattering of two particles, it is important that the interaction takes place over a short distance so that α_s is small enough to use perturbation theory. The parton model represents the lowest order $O(\alpha_s^2)$ approximation to QCD: a large energy transfer is needed to ensure that the time scale of the interaction is short and the effects of the spectator partons (those partons not involved with the scatter) can be ignored.

The subprocess in high energy inelastic proton-antiproton collisions consists of a scatter between two constituent partons. The fact that the $p\bar{p}$ collision is at high energy does not necessarily imply that perturbative QCD is valid, because the partons only carry a fraction of the parent protons energy. However, a small value of α_s can be ensured by demanding that final state particles from the scatter have a high momentum transverse (high-P_t) to the proton-antiproton beam axis.

The basic subprocess diagram for high-P_t hadron production from $p\bar{p}$ collisions is shown in Figure 12, where A and B are the proton and antiproton in collision, and C is some high transverse momentum hadron in the final state. The partons i and j carry a fraction x_i and x_j of the momentum of hadrons A and B, described by the structure functions $F_A{}^i(x_i)$ and $F_B{}^j(x_j)$ respectively. The partons i and j scatter via the strong interaction to produce partons k and l. In their centre-of-mass frame, the produced partons separate with equal and opposite momentum, α_s becomes large and the partons hadronize to form two back-to-back jets which are roughly collinear with their parent parton directions. The spectator partons from A and B also hadronize to form a spray of low-P_t particles.

The lowest order differential cross-section for the QCD subprocess $i+j \rightarrow k+l$ has been calculated [14] and is defined by

$$\frac{d\bar{\sigma}}{d\bar{t}} = \frac{\pi\alpha_s|A|^2}{\bar{s}^2}$$

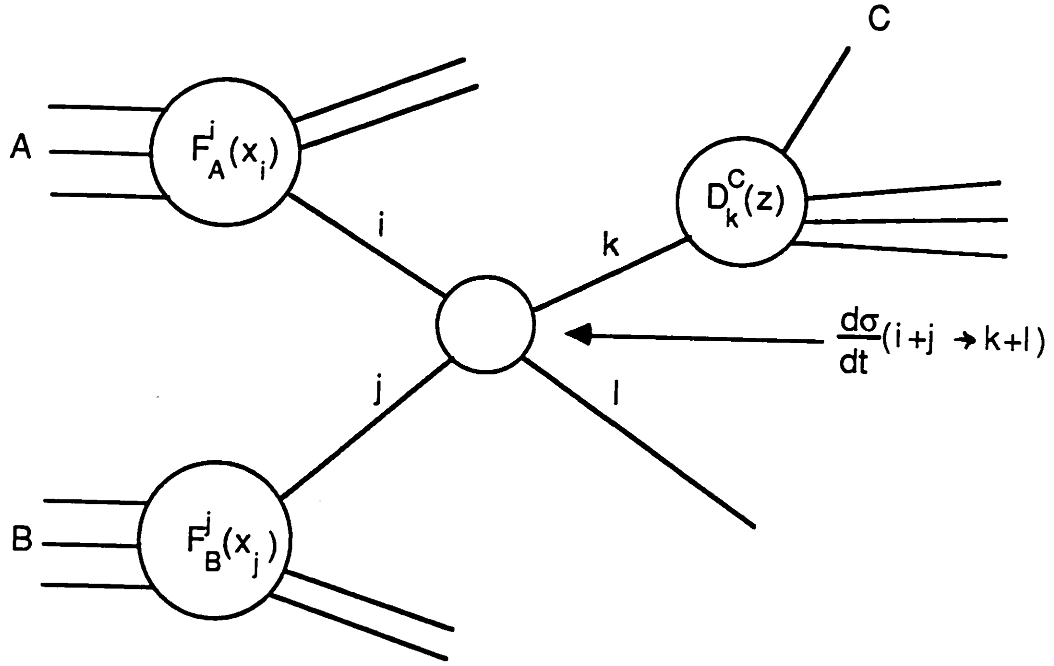

Figure 12: Basic diagram for parton-parton scattering

where $\bar{s}$ and $\bar{t}$ are two of the Mandelstam variables

$$\bar{s} = x_i x_j s$$
$$\bar{t} = -x_i x_k s$$
$$\bar{u} = -x_j x_k s$$

where s is the square of the proton-antiproton centre-of-mass energy,

$|A|^2$ is the amplitude of the subprocess $i+j \rightarrow k+l$. The QCD subprocesses and their amplitudes are listed in Table 3.

The contributions of the different QCD subprocesses

	Subprocesses	$\|A\|^2$
1	$q_iq_j \to q_iq_j,\ q_i\bar{q}_j \to q_i\bar{q}_j\ (i \neq j)$	$\frac{4}{9}(\hat{s}^2+\hat{u}^2)/\hat{t}^2$
2	$q_iq_i \to q_iq_i$	$\frac{4}{9}\left(\frac{\hat{s}^2+\hat{u}^2}{\hat{t}^2}+\frac{\hat{s}^2+\hat{t}^2}{\hat{u}^2}\right)-\frac{8}{27}\frac{\hat{s}^2}{\hat{u}\hat{t}}$
3	$q_i\bar{q}_i \to q_i\bar{q}_i$	$\frac{4}{9}\left(\frac{\hat{s}^2+\hat{u}^2}{\hat{t}^2}+\frac{\hat{t}^2+\hat{u}^2}{\hat{s}^2}\right)-\frac{8}{27}\frac{\hat{u}^2}{\hat{s}\hat{t}}$
4	$q_i\bar{q}_i \to gg$	$\frac{32}{27}\left(\frac{\hat{u}^2+\hat{t}^2}{\hat{u}\hat{t}}\right)-\frac{8}{3}\left(\frac{\hat{u}^2+\hat{t}^2}{\hat{s}^2}\right)$
5	$gg \to q_i\bar{q}_i$	$\frac{1}{6}\left(\frac{\hat{u}^2+\hat{t}^2}{\hat{u}\hat{t}}\right)-\frac{3}{8}\left(\frac{\hat{u}^2+\hat{t}^2}{\hat{s}^2}\right)$
6	$q_ig \to q_ig$	$-\frac{4}{9}\left(\frac{\hat{u}^2+\hat{s}^2}{\hat{u}\hat{s}}\right)+\left(\frac{\hat{u}^2+\hat{s}^2}{\hat{t}^2}\right)$
7	$gg \to gg$	$\frac{9}{2}\left(3-\frac{\hat{u}\hat{t}}{\hat{s}^2}-\frac{\hat{u}\hat{s}}{\hat{t}^2}-\frac{\hat{s}\hat{t}}{\hat{u}^2}\right)$

Table 3: *Amplitudes of the lowest order QCD subprocesses*

Given the sum of differential cross-sections for all subprocesses, the probability distributions in x_i and x_j and the probability that k hadronizes to form C (described by the fragmentation function $D_k{}^C(z)$ discussed in the next section), the invariant cross-section for A + B → C + X can be written as

$$E_c \frac{d\sigma}{d^3 p_c} = \sum_{ijkl} \int_0^1 dx_i \int_0^1 dx_j \; x_i f_A(x_i) x_j f_B(x_j) \frac{d\sigma}{dt}(i+j \rightarrow k+l) \frac{1}{\pi} z_c D_k^C(z)$$

2.4.2 Fragmentation

Fragmentation is the process whereby partons materialise as colourless hadrons in the final state. The fragmentation function $D_k{}^h(z)$ describes the probability of finding a hadron h with a fraction z of the energy of its parent parton k. In the first approximation, fragmentation is a scaling phenomenon because it depends only on the dimensionless fraction $z = E_h/E_k$. Energy conservation implies that

$$\sum_h \int_0^1 z D_q^h(z) dz = 1$$

The process of fragmentation occurs over a large time scale compared to the hard scatter. As the two partons separate, α_s becomes large and a perturbative approach fails. Several phenomenological models have therefore been developed in the absence of any complete calculation.

It is instructive to discuss the model of Independent Fragmentation (IF) by Field and Feynman [15] because this model is used in this thesis as part of the Monte Carlo generation of $p\bar{p}$ collisions. The IF model is represented by Figure 13. The colour field surrounding a quark creates a $q_1\bar{q}_1$ pair, and the original quark forms a meson with the created $\bar{q}_1$. The process is then repeated using q_1 as a starting point. The IF model assumes that each step in the fragmentation chain is independent of any previous step, and that all distributions scale to depend only on the fraction of hadron to quark momenta.

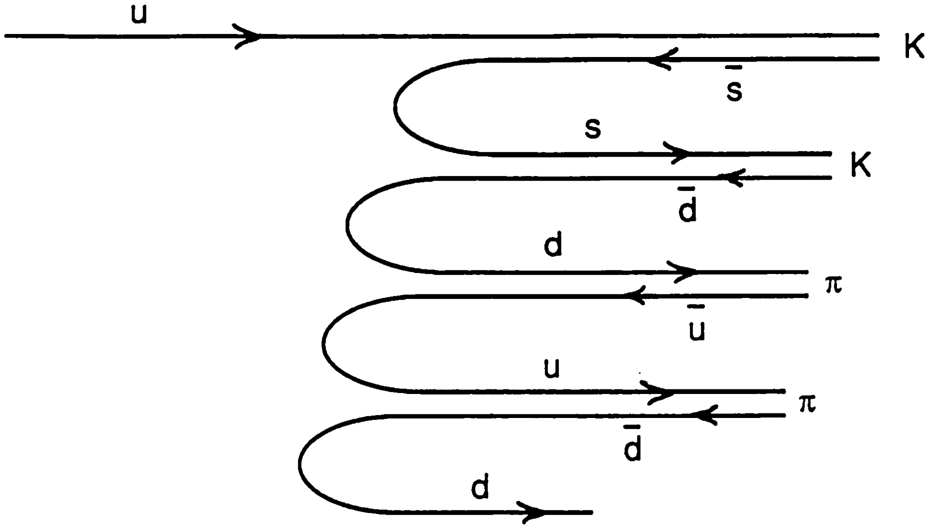

Figure 13: The Independent Model of fragmentation

There are some conceptual and theoretical inconsistencies with the IF model. For example the model fails to conserve flavour (there is some uncertainty about how to treat the last quark in the cascade) and fails to conserve energy. Energy conservation has to be imposed after the cascade is generated by boosting the final state hadrons to a rest frame, rescaling the 3-momenta and then recalculating the energy.

2.4.3 QCD Corrections to the Parton Model

The parton model ignores the role of the gluon as the mediator of the strong interaction, so QCD departs from the parton model when the next highest order corrections in α_S are implemented. In QCD, partons can radiate gluons both before and after the hard scatter as depicted by Figure 14.

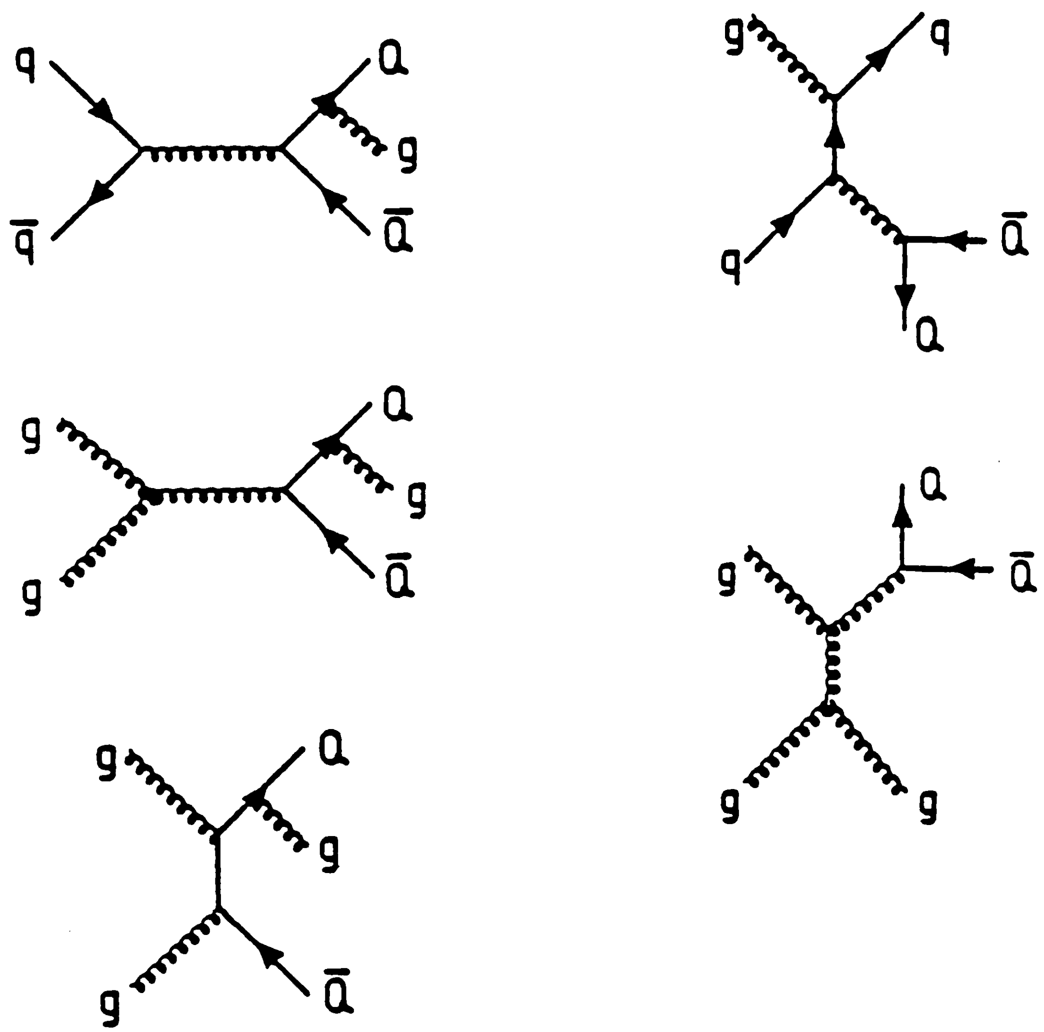

Figure 14: Examples of $O(\alpha_s^3)$ QCD diagrams

To the first approximation, the probability that a parton of virtuality Q^2 will radiate a gluon is a function of $\log(Q^2)$, the so-called leading log approximation. Initial state gluon bremsstrahlung decreases the energy of the parton prior to the hard scatter, so the structure functions become Q^2-dependent ($f(x) \rightarrow f(x,Q^2)$). Similarly, final state gluon bremsstrahlung introduces a Q^2-dependence into the fragmentation functions ($D(z) \rightarrow D(z,Q^2)$).

Experimental evidence of gluon bremsstrahlung is provided by observed scaling violations in both structure and fragmentation functions at high interaction energies. In addition, a sufficiently hard gluon bremsstrahlung can fragment to produce a jet in the final state. The cross-section for gluon bremsstrahlung diverges when $P_g \to 0$ and $\theta_g \to 0$, where P_g is the gluon momentum and θ_g is the angle of emission of the gluon with respect to the parent quark or gluon direction of motion. This becomes evident in $p\bar{p}$ collisions because the angular distribution of jets from initial state bremsstrahlung is peaked towards 1 in $|\cos\theta^*|$, where θ^* is the angle between the jet axis and the proton-antiproton beam axis.

2.4.4 The Drell-Yan Process

The process of lepton pair production in $p\bar{p}$ collisions via the Drell-Yan mechanism can be simply interpreted in terms of the parton model. Figure 15 shows the lowest order $O(\alpha^2)$ Drell-Yan process $q\bar{q} \to \gamma^* \to \ell^+\ell^-$.

The experimental signature of the lowest order Drell-Yan mechanism is that of two oppositely charged leptons back-to-back in the plane transverse to the $p\bar{p}$ beam axis. The next highest order correction ($O(\alpha^2\alpha_S)$) to the basic Drell-Yan diagram as shown in Figure 16 can diminish the back-to-back topology of the leptons because the virtual photon can be imparted with a significant momentum transverse to the beam axis. The expected final state topology of the events of Figure 16 is therefore that of two oppositely charged leptons back-to-back in azimuth with a jet.

The Drell-Yan process in $p\bar{p}$ collisions has played an important role in testing the parton model and its QCD corrections because the cross-section for pointlike scattering is well understood from QED. In $p\bar{p}$ collisions the cross-section must be corrected for the quark structure functions and the fractional charge of quarks.

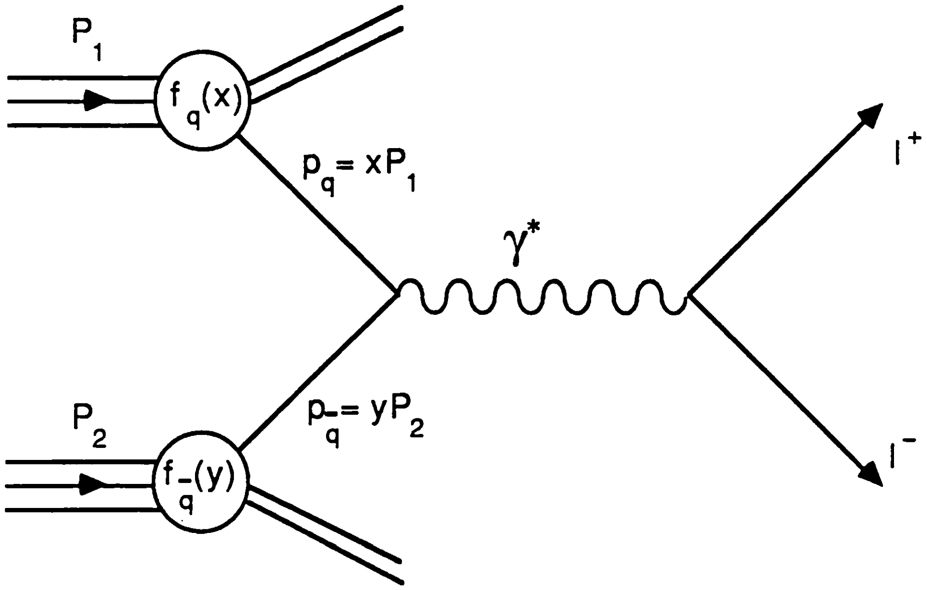

Figure 15: The Drell-Yan mechanism

2.4.5 Intermediate Vector Boson Production

Provided there is sufficient energy available (the $W^{\pm}$ and Z^0 have rest masses of about 83 GeV/c^2 and 93 GeV/c^2 respectively), the $W^{\pm}$ and Z^0 Intermediate Vector Bosons (IVBs) can be produced in p$\bar{p}$ collisions via the Drell-Yan process of Figure 17.

The cross-sections for IVB production can be calculated using the Drell-Yan mechanism with the vertex describing the IVB creation characterised by the weak coupling. Cross-sections for $W^{\pm}$ and Z^0 production are therefore very small (less than 10^{-8} of the total p$\bar{p}$ cross-section). Although the IVBs can decay hadronically to form two jets of hadrons in the final state, it is difficult to extract the signal from the larger number of QCD produced 2-jet events. Therefore the best chance of detecting IVBs in p$\bar{p}$ collisions is via their leptonic decays to electrons or muons:

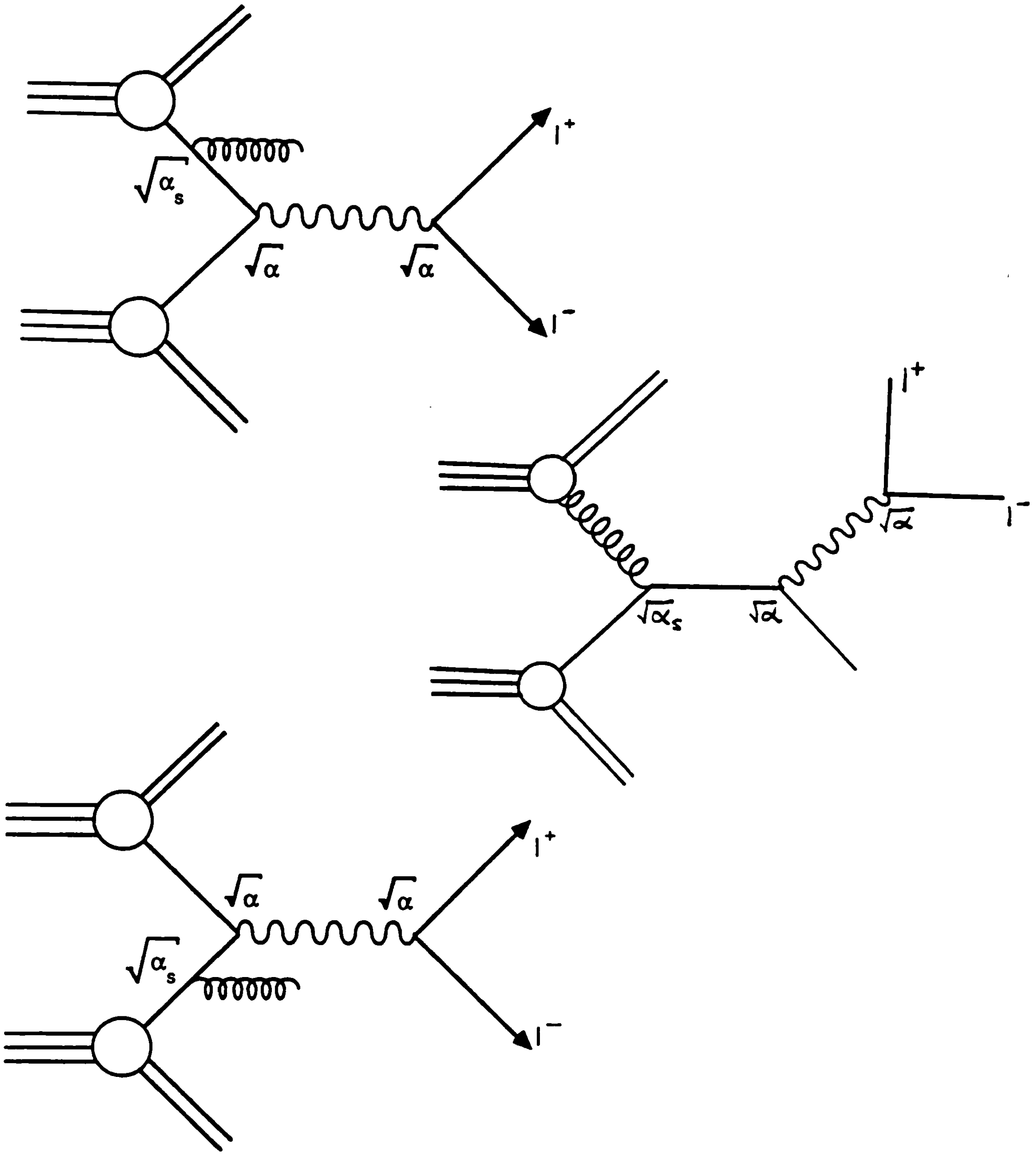

Figure 16: Higher order corrections to the Drell-Yan process

$$p\bar{p} \rightarrow W^{\pm}X \rightarrow \ell^{\pm}\nu X$$

$$p\bar{p} \rightarrow Z^0X \rightarrow \ell^{+}\ell^{-}X$$

The experimental signature for leptonic decays of the $W^{\pm}$ is a lepton with a large component of momentum, P_t, transverse to the $p\bar{p}$ beam axis. Although the neutrino cannot be detected experimentally, a consequence of the $W \rightarrow \ell\nu$ two-body decay is that

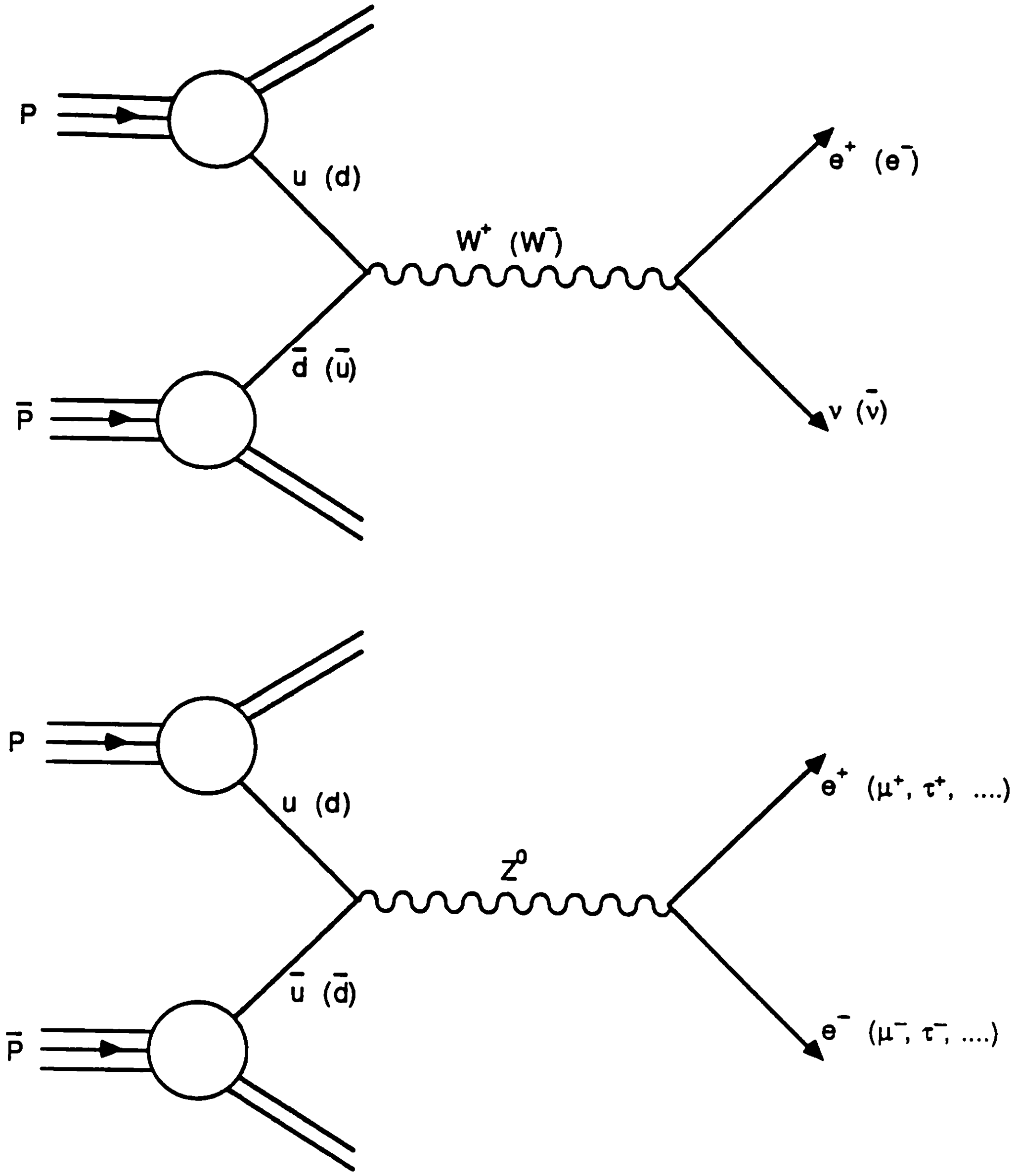

Figure 17: W and Z production via the Drell-Yan mechanism

the lepton has a Jacobian peak in its P_t distribution near $P_t = M_W/2$. This follows directly from Figure 18 if the transverse energy of the W is negligible.

Occasionally W and Z candidates may contain a jet in the final state which arises from the $O(\alpha_s)$ corrections to the Drell-Yan mechanism as shown in Figure 16.

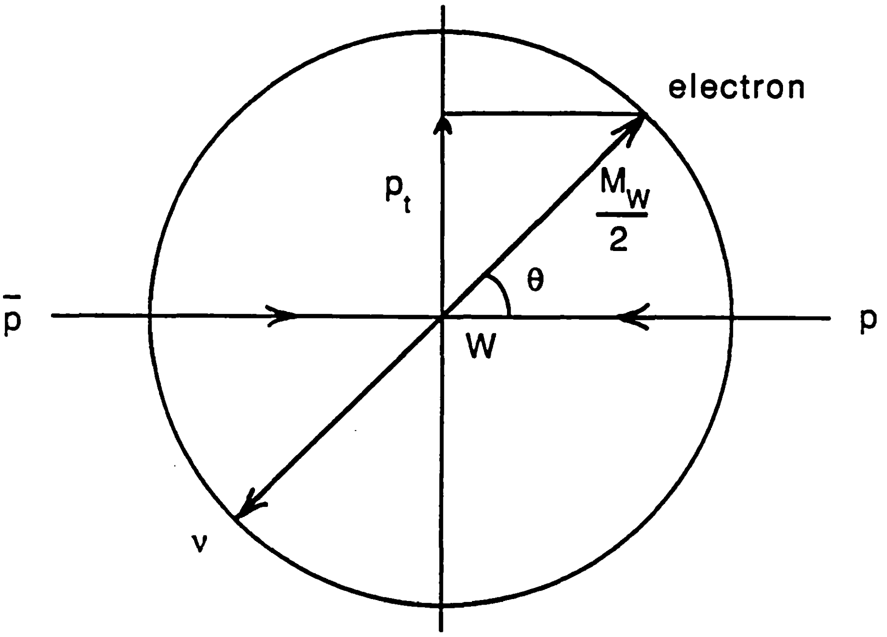

$$\frac{d\sigma}{dp_t} = \frac{d\sigma}{d\cos\theta}\,\frac{d\cos\theta}{dp_t} = \frac{2p_t}{M_W\sqrt{\frac{1}{4}M_W^2 - p_t^2}}\,\frac{d\sigma}{d\cos\theta}$$

Figure 18: The 2-body W→eν decay

2.4.6 Heavy Flavour Production

There are two important sources of heavy flavour production in high energy $p\bar{p}$ colliders:

1. Production via the weak bosons

$$W^+ \rightarrow t\bar{b}, c\bar{s} \text{ and } W^- \rightarrow b\bar{t}, s\bar{c}$$

$$Z^0 \rightarrow c\bar{c}, b\bar{b}, t\bar{t}$$

2. QCD flavour creation

$$gg, q\bar{q} \rightarrow Q\bar{Q} \quad Q=c,b,t$$

Production via the weak bosons provides a better calibrated event sample because calculations of production rates can be normalised to measured values of $\sigma(p\bar{p} \rightarrow W^{\pm}X \rightarrow \ell^{\pm}\nu X)$ and $\sigma(p\bar{p} \rightarrow Z^{0}X \rightarrow \ell^{+}\ell^{-}X)$. However, the low rate of W and Z production and the difficulty of extracting a signal means that this source of heavy flavour production is not important except for searches of the top quark.

The more dominant source of heavy flavour production is via QCD processes. The QCD production of heavy flavours implies that the interaction energy is large so that perturbative QCD calculations based on the QCD 2→2 Feynman diagrams of Figure 19 are expected to be valid.

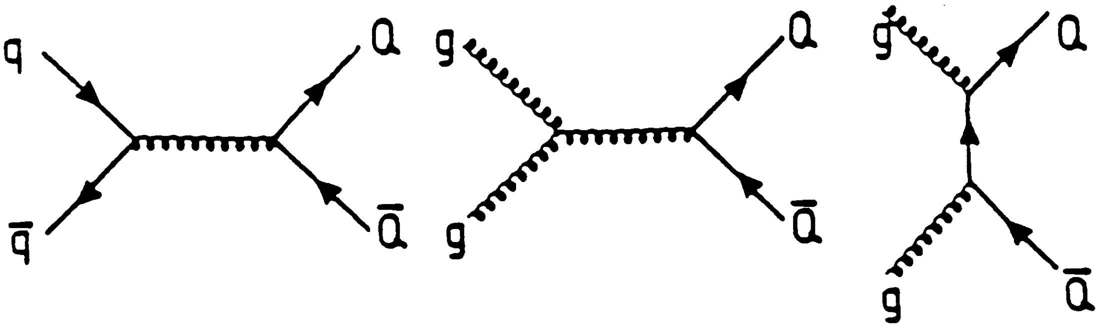

Figure 19: Lowest order QCD processes for heavy flavour production

However, gluon splitting ($g \rightarrow Q\bar{Q}$) in the QCD 2→3 processes of Figure 14 can also make a significant contribution, particularly for charm production when the virtuality of the gluon is not too large.

Again, the best hope of distinguishing heavy flavour production in $p\bar{p}$ collisions is to search for candidates of their semileptonic decays:

$$t \rightarrow b\ell\nu, \quad b \rightarrow c\ell\nu, \quad c \rightarrow s\ell\nu$$

A schematic diagram of the semileptonic decay of the predicted top quark is shown in Figure 20.

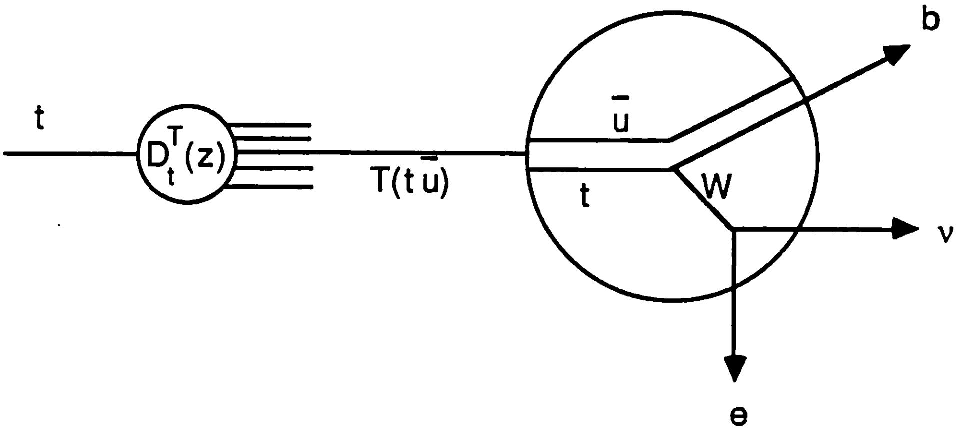

Figure 20: The semileptonic decay of heavy flavours

In Figure 20, a light u quark (created in the fragmentation cascade) pairs with the parent top quark to form the meson T. However, the fragmentation of heavy quarks behaves differently from that of light quarks: the top quark is heavy and therefore carries a large momentum, so the T meson has a momentum close to that of the parent top quark. Heavy quarks therefore have 'hard' fragmentation functions, because the heavy flavour meson carries most of the parent quark momentum. The fragmentation functions $D_Q^h(z)$ for heavy flavours (Q = c,b) have been parameterised by Peterson et al [16] using data taken at e^+e^- colliders, and takes the form

$$D(z) = \frac{4\sqrt{\varepsilon}}{\pi z\left(1 - \frac{1}{z} - \frac{\varepsilon}{(1-z)}\right)^2}$$

where ε is a parameter which depends on the quark mass. The $D_Q^h(z)$ distributions become increasingly hard with increasing quark mass, with $<z> \simeq .7, .85$ and ≤ 1 for c, b and t quarks respectively.

The second stage of Figure 20 represents the semileptonic decay of the t quark via the emission of a W boson. The daughter quark (for example the b in Figure 20) fragments to form a jet in the final state. The separation of the jet from the lepton is dependent on the parent quark mass: the lepton is expected to be imbedded within the jet for semileptonic decays of the c or b quarks, but will in general be separated from the jet in semileptonic decays of top.

3. THE UA1 DETECTOR

3.1 Introduction

The search for the leptonic decays of the Intermediate Vector Bosons provided important guidelines on the design of the UA1 detector. In particular, the detector was designed to:

1. Identify electrons and muons, and measure their energy by both calorimetry and curvature in a magnetic field;
2. Measure the missing transverse energy and infer the presence of neutrinos;
3. Cover the greatest possible solid angle (~4π steradians) to reduce bias.

Figure 21 shows a section through the centre of the UA1 apparatus in the vertical (XY) plane.

The Central Detector (CD) is a cylindrical drift chamber that tracks charged particles, and measures their momentum by the curvature of their tracks in a horizontal dipole magnetic field. A dipole field is used in preference to a solenoidal field because it offers superior bending power to the high multiplicity of tracks surrounding the beam axis that arise from the spectator system of the $p\bar{p}$ collision. The CD is surrounded by the central electromagnetic calorimeters which are used to measure the energy and position of incident electrons and photons. The electrons or photons deposit most or all of their energy by interacting with the material of the calorimeters to form a shower of increasing numbers of smaller energy particles. Most of the energy is dissipated in the form of heat, but a very small fraction of the energy is converted into a measurable signal (scintillator light) which is proportional to the energy of the incident particle. Surrounding the central electromagnetic calorimeters is a large iron box which acts as the return yoke of the dipole magnet and is also instrumented to act as a hadronic calorimeter. The hadronic calorimeter is used to measure the energy and position of strongly interacting particles. Arrays of

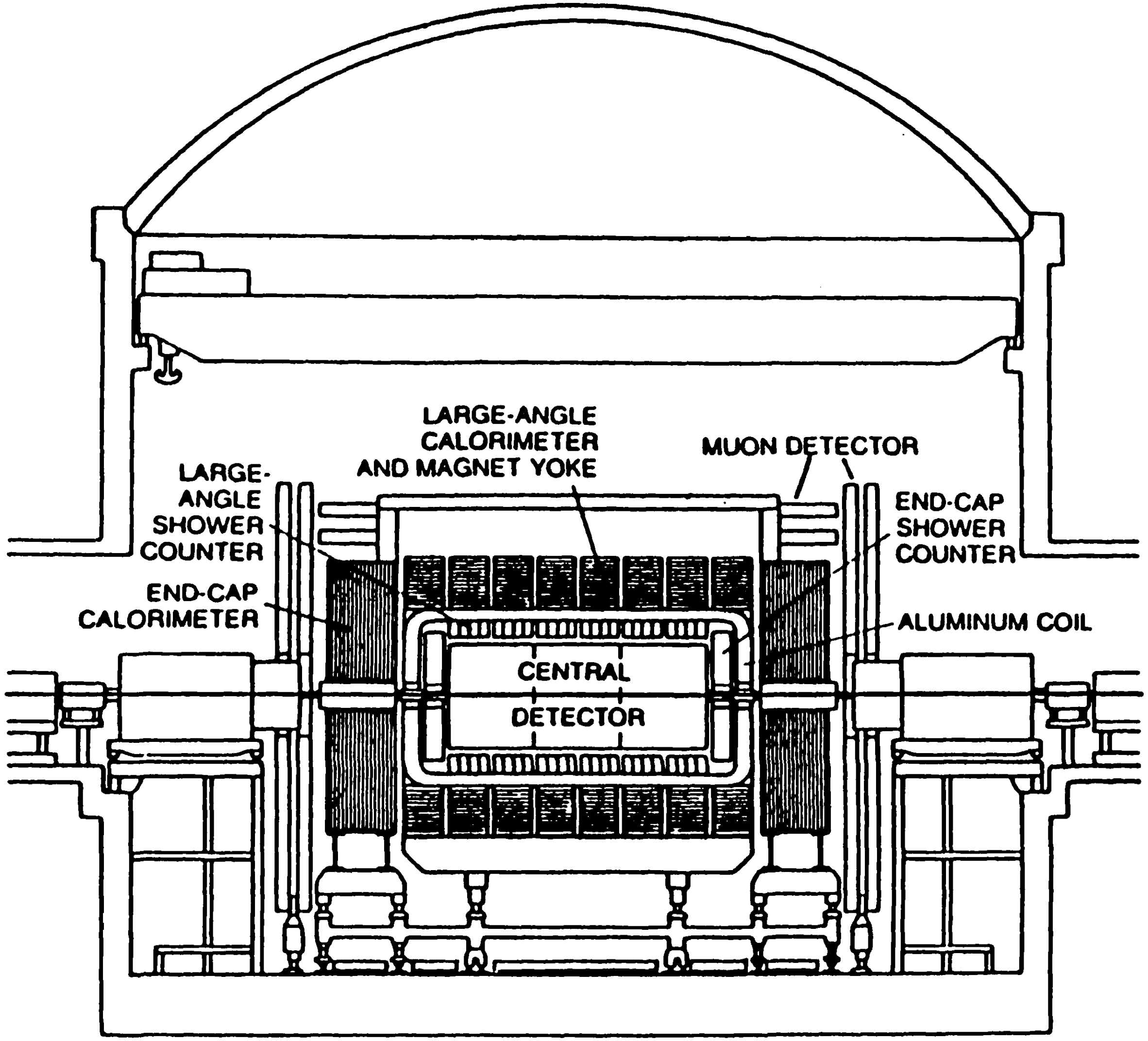

Figure 21: Section through the centre of the UA1 detector in the vertical plane

drift tubes surround the iron box to track escaping muons. There are additional calorimeters and drift chambers surrounding the beam pipe outside of the magnet which are used to detect particles produced at very low angles with respect to the beam axis.

This chapter describes the parts of the UA1 apparatus that are relevant to an inclusive study of electron production, including the operation of the UA1 detector and the subsequent processing of the data. The cartesian coordinate system which is used to describe the UA1 detector is defined in Appendix A.

3.2 The SPS Collider

The SPS is 2.2 km in diameter and produces $p\bar{p}$ collisions to within 0.3m of the centre of the UA1 detector. A detailed description of the CERN accelerator complex is clearly beyond the scope of this thesis, though a general summary of the $p\bar{p}$ injection procedure is given below.

The CERN accelerator complex is shown in Figure 22.

Protons are accelerated in the Proton Synchrotron (PS) up to a momentum of 26 GeV/c and are then released on to a copper target. A magnetic horn selects antiprotons with about 3.5 GeV/c momentum (the momentum at which the maximum yield of $\bar{p}$s occurs) amongst the spray of secondary particles and injects them into the Antiproton Accumulator (AA). About 10^7 antiprotons are selected with each pulse (1 antiproton per $\sim 10^6$ incident protons). As well as accumulating the antiprotons, the AA reduces the random motion of the antiprotons transverse to the $\bar{p}$ beam direction by the method of stochastic cooling [18]. After about 3 days, $\sim 10^{12}$ $\bar{p}$s have been injected into the AA, and the cooling process has reduced the random motion of the $\bar{p}$s to produce a dense core of $\sim 6\times 10^{11}$ antiprotons. The core is ejected at 3.5 GeV/c into the PS, leaving a residue of some 4×10^{11} antiprotons to start the formation of the next core. The antiprotons in the PS are then accelerated to 26 GeV and injected together with the protons into the SPS where they form bunches which are accelerated to 273 GeV/c or 315 GeV/c.

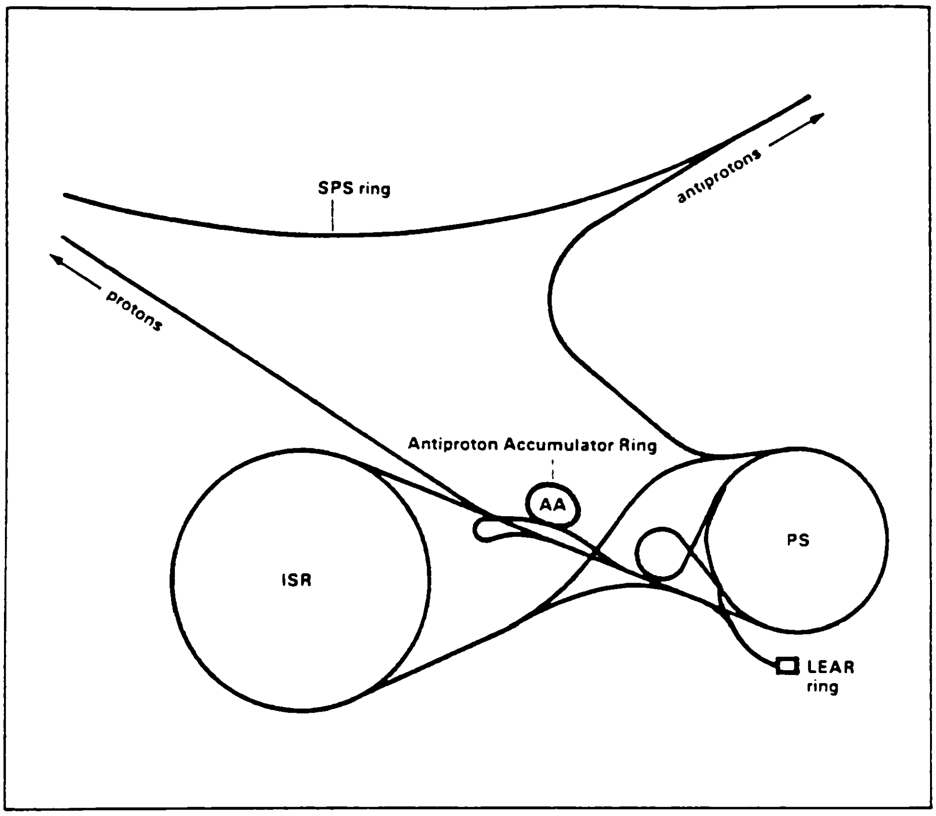

Figure 22: The CERN accelerator complex

The instantaneous luminosity of the collider is given by

$$L = fnN(p)N(\bar{p})/A$$

where

$N(p)$, $N(\bar{p})$ are the numbers of protons and antiprotons per bunch,

f is the revolution frequency,

n is the number of bunches per beam,

and A is the cross-section area of the beam, assuming the beams overlap completely.

The collider was designed to operate with 6 bunches of protons and 6 bunches of anti-protons giving a beam crossing time of 3.8μs and a peak luminosity of 1$\mu b^{-1}s^{-1}$. The SPS has since kept to 3 bunch operation giving a peak luminosity at the UA1 detector of about 0.5$\mu b^{-1}s^{-1}$, though UA1 has kept with the 3.8μs timing for triggering and readout in order to retain the capability of running with 6 bunches should it come into operation.

After the $p\bar{p}$ bunches are injected into the SPS, the luminosity falls with a half life of ~10 hours due to particle interactions within the bunches and with residual gas. A typical beam run lasts one or two days.

3.3 The Central Detector

The central detector is a self-supporting cylindrical drift chamber with electronic image readout which is capable of reconstucting three dimensional images of track trajectories. It covers a solid angle of 3.8π steradians around the beam crossing point, corresponding to an angular coverage of

$$5^0 < \theta < 175^0$$

$$0 < \phi < 2\pi.$$

The detector is 6m long and 2.2m in diameter, and is divided into six semi-cylindrical chambers each of length 2m. To enable a measurement of track momentum, the central detector sits inside a 0.7 Tesla uniform dipole magnetic field. A schematic diagram of the central detector is shown in Figure 23.

Each of the chambers consists of planes of wires separated by 174mm. The planes are alternately anode and cathode as shown in Figure 24, and the electric field between each plane is 1.5kV/cm.

The chambers contain an argon-ethane gas mixture. A charged particle passing through the CD ionizes the gas to produce electrons. The electrons then drift towards the nearest anode plane with a maximum drift-time of 3.6μs which is sufficiently smaller than the minimum proposed beam crossing time of 3.8μs.

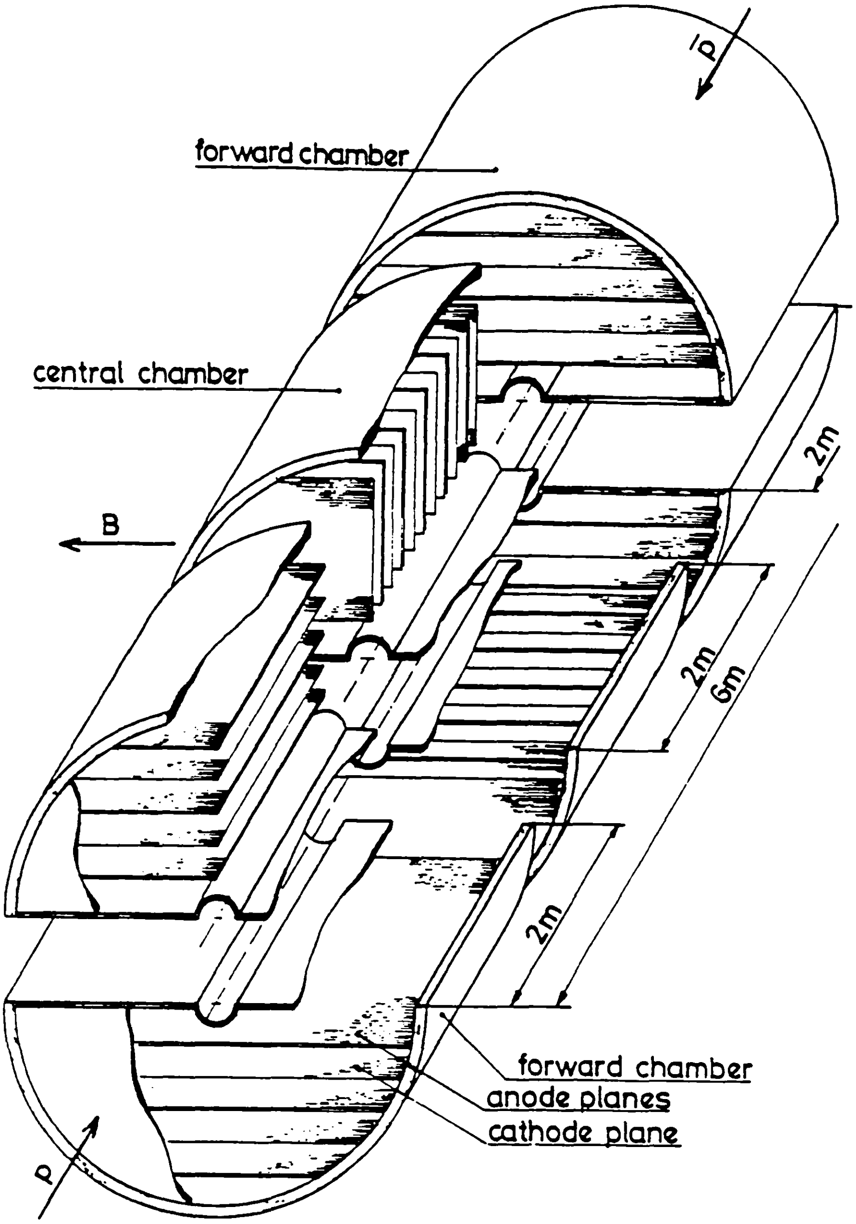

Figure 23: The Central Detector

The configuration of each anode plane is shown in detail in Figure 24. An anode plane in fact consists of two planes of wires which are alternately cathode wires and

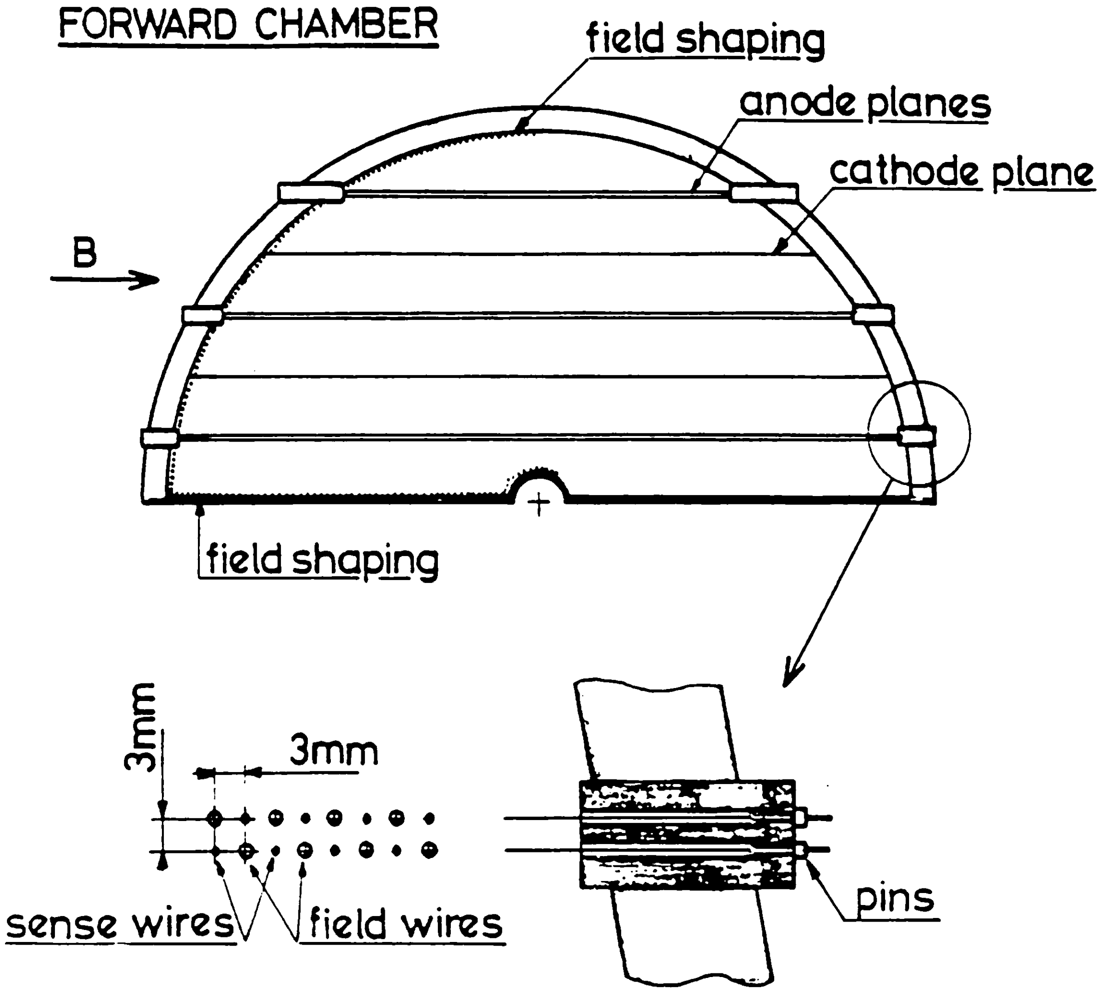

Figure 24: The Wire Layout in the Central Detector

grounded anode sense wires. This configuration ensures that electrons cannot cross the plane and removes left-right ambiguities. The intense electric field that surrounds a sense wire causes the drifting electrons to ionize the gas and start an avalanche which produces a pulse on the wire. Each anode wire is strobed every 32ns and a measurement of charge is made at each end of the wire by two Fast Analogue to Digital Converters (FADCs) and a Time to Digital Converter (TDC). One FADC measures the coordinate along the wire by charge division, the other measures the total charge on the wire to enable a calculation of dE/dx of the ionizing particle. The TDC measures the time of arrival of the pulse with respect to a reference time (eg the $p\bar{p}$ beam crossing trigger). The coordinate of the ionizing particle along the wire together with how close the particle passed to the wire (given by the TDC information) enables the trajectory of the particle to be reconstructed.

In order to make full use of the drift-times for measurements of particle momentum, all sense wires are parallel with the magnetic field. The orientation of the wire planes is also optimised for drift-time measurements: the central chambers have vertical wire planes because central tracks tend to have a large component of their momentum transverse to the beam axis, whereas the forward chambers have horizontal wire planes. There is a region of poor drift-time and charge division measurements within $\pm 10^0$ of the horizontal plane because the track direction is then parallel to the sense wires. However, this represents a negligible fraction of the solid angle, and particles in the horizontal plane are still absorbed by the central calorimeters. The momentum resolution of the central detector is in fact dominated by the measurement error in the track sagitta for high momentum tracks. For a 1m track, the resolution is given by

$$\Delta p/p = 0.005p$$

Particle identification by the CD using the dE/dx information is possible at momenta below about 1 GeV. Figure 25 [19] shows dE/dx as a function of momentum which clearly shows separation between the particles $p, \pi^\pm$ and $K^\pm$ The main use of dE/dx measurements is to help resolve two or more superimposed tracks. The two-track resolution of the CD is summarised in Table 4.

Some technical details of the central detector are summarised in Table 5.

Table 4: Resolution of the Central Detector

0.1-0.3mm	along drift direction
20.0mm	along a wire
5.0mm	in the planes of wires perpendicular to the wire length

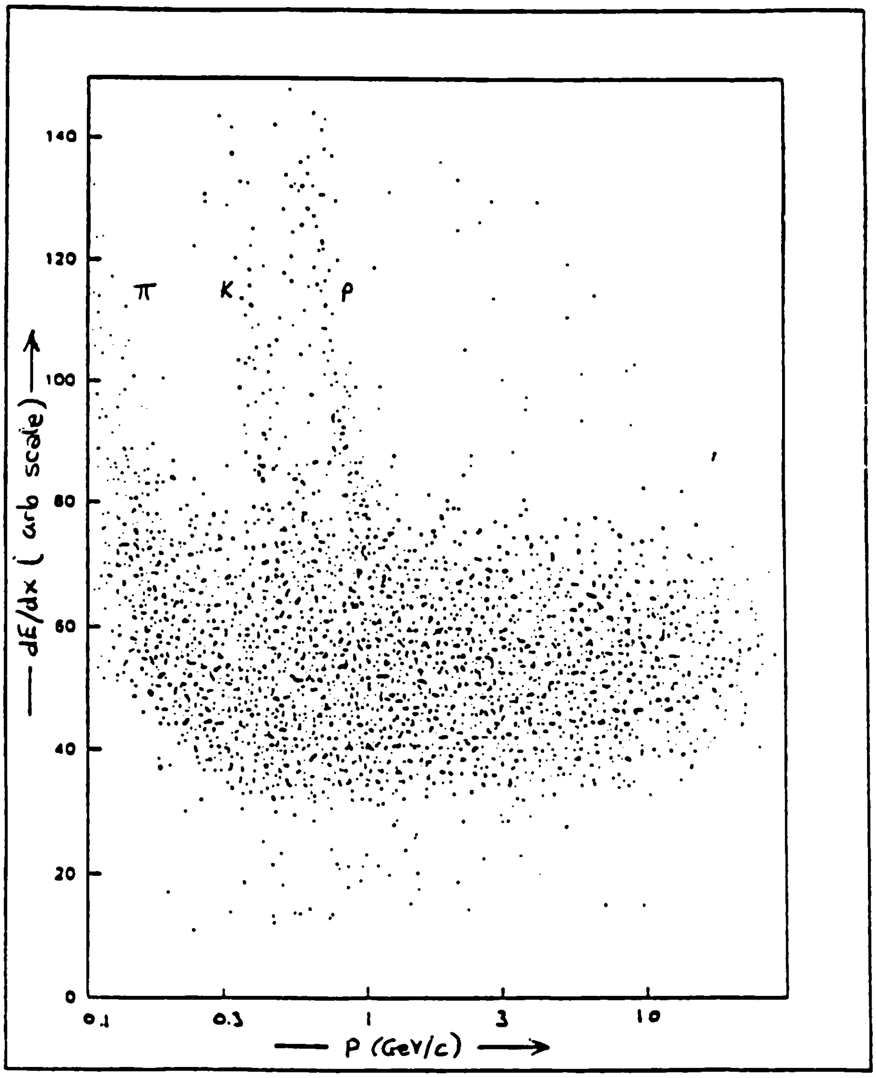

Figure 25: dE/dx for Tracks in the Central Detector

Table 5: Parameters of the Central Detector

Gas Mixture	Argon(40%) + Ethane(60%)
Drift Field and gap length	1.5kV/cm , 0.18cm
Drift Velocity	5.3cm/μs
Drift Angle	23^0 at B = 0.7 Tesla
Anode plane arrangement:	
Dist. between sense wires	10mm
Wire Length	80cm min., 220cm max.
Sense wire charac.	35μm Ni-Cr stretched at 80g
Field wire charac.	100μm gold-plated Cu-Be stretched at 200g
Cathode wire struc:	
Distance between wires	5mm
Wire characteristics	150μm gold-plated Cu-Be stretched at 200g
Total number of wires	22800
Total number of sense wires	6110

3.4 The Central Electromagnetic Calorimeters

The purpose of the electromagnetic calorimeters is to identify incident electrons and photons and to measure their energy. The incident electrons and photons induce electromagnetic showers which develop primarily through bremsstrahlung and e^+e^- pair production. Their longitudinal development is determined by the radiation length, which is related to the mean free path of an electron in the material. The shower increases its multiplicity of secondary particles until the energy of the photons fall below the threshhold for e^+e^- pair production. The number and energy of the secondaries then decreases with a characteristic attenuation length which is determined by the mean free path of a photon which has an energy corresponding to the minimum absorption in the material.

The central part of the electromagnetic calorimetry in UA1 [20] covers the angular range

$$25^0 < \theta < 155^0$$

and consists of two semi-cylindrical parts that fit radially around the outside of the central detector. Each of the two parts consist of 24 individual segments called gondolas. Two gondolas are shown in Figure 26. Each gondola consists of 74 pairs of 2mm thick sheets of lead sandwiched between 2mm thick sheets of plexipop scintillator, which corresponds to 26.4 radiation lengths. The active part of a gondola covers approximately 160^0 in azimuth.

The scintillator sheets are read out at each of their four corners via BBQ wavelength shifter bars which absorb the scintillation light ($\lambda \simeq 420$nm) and re-emit the light isotropically at a longer wavelength ($\lambda \simeq 480$nm). Although there is some loss of light using this technique, there is uniformity of response and the extraction of light from awkward locations is made easier. The light is then transmitted through conventional light guides to photomultipliers which are mounted vertically above and below the gondolas outside the return yoke of the magnet.

The light outputs from each gondola are summed together in depths of 3.3,6.6,9.9 and 6.6 radiation lengths in order to determine the shape of the longitudinal shower profile. The four samplings in depth help to discriminate against early hadronic showers (which are not so unlikely given the 0.8 hadronic interaction lengths of each gondola). The gondolas also measure both the energy of the shower and its azimuthal position; the total light collected is a measure of the energy absorbed by the gondola, and the imbalance in the amplitude of the light pulses between the top and bottom of the gondola gives the azimuthal position.

In addition to the gondolas, there are central electromagnetic calorimeters called bouchons [21]. The bouchons form the end caps of the central electromagnetic calorimeters and cover the angular ranges

$$5^0 < \theta < 25^0 , 155^0 < \theta < 175^0$$

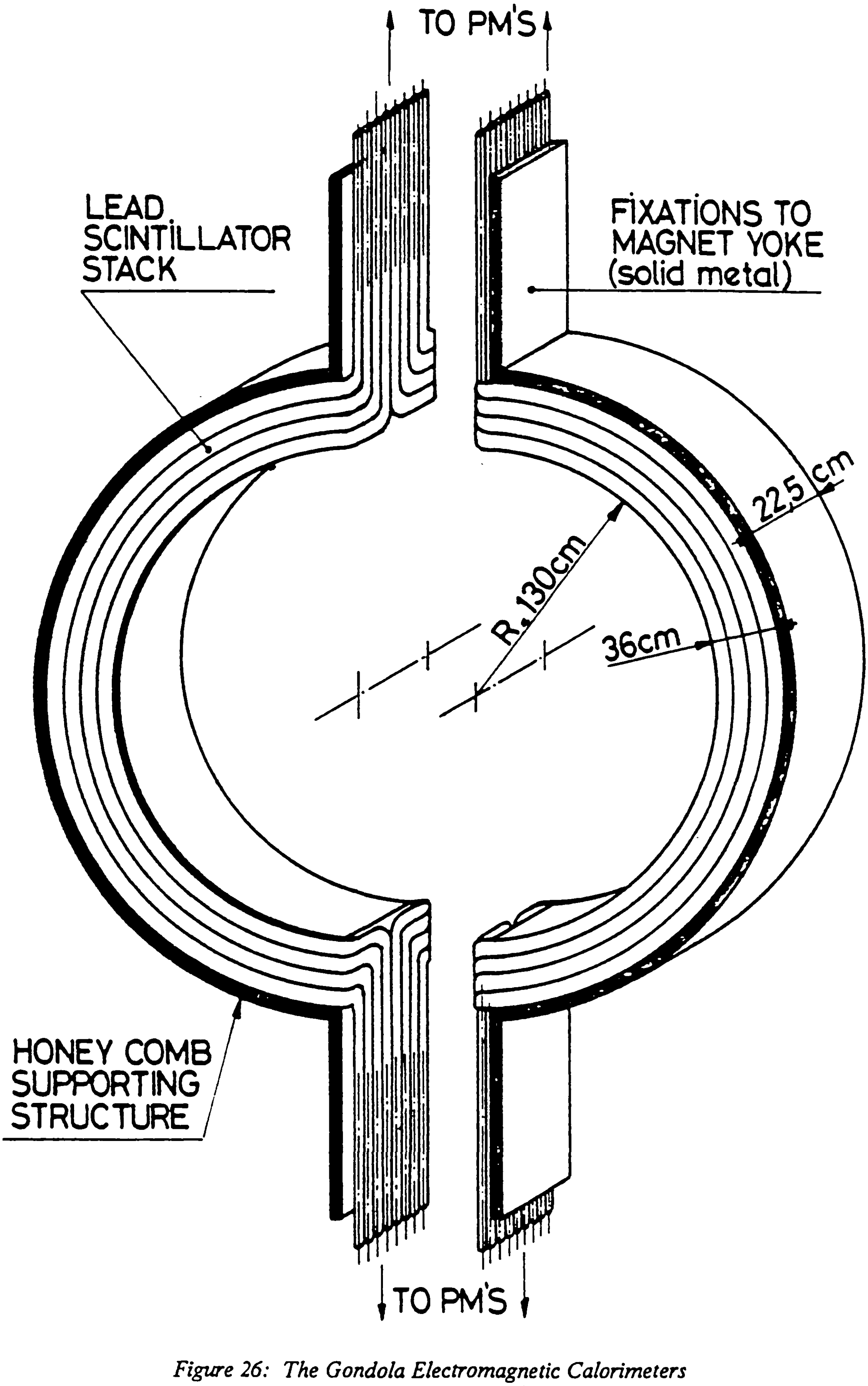

Figure 26: The Gondola Electromagnetic Calorimeters

with respect to the beam crossing point. The bouchons are positioned at each end of the central detector at 3m from the beam crossing point, and are segmented radially into 32 petals of angular size $\delta\theta \times \delta\phi = 20^0 \times 11.2^0$. One of the bouchons is shown in Figure 27. The petals are 26.7 radiation lengths thick and consist of a sandwich of 4mm lead sheets and 6mm plexipop scintillator sheets.

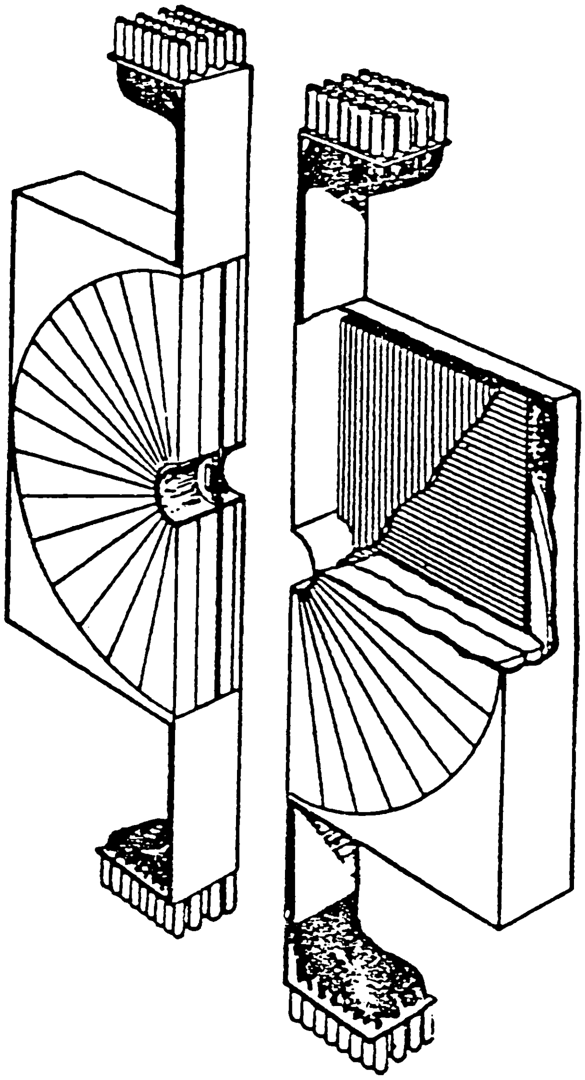

Figure 27: The Bouchon Electromagnetic Calorimeter

Scintillation light is channelled to photomultipliers via BBQ wavelength shifters and light guides that run around the outer edge of the petals. The light is summed together into four samplings in depth of 3.6,7.2,8.7 and 7.2 radiation lengths to provide information on the longitudinal shower profile. In addition to the lead-scintillator sandwich, there is a position detector between the second and third samplings of the bouchons that determines the position of the shower. The position detectors consist of two orthogonal planes of proportional tubes that are used to determine the shower position by charge division.

There are four stages to the absolute calibration and monitoring of the gondolas and bouchons:

1. An absolute calibration at the beginning of each run using a collimated 1.2 MeV γ-beam. The calibration point is in the centre of each petal at a radius of 1m from the beam axis, and in the centre of each gondola. The response of the calorimeters to the source is compared directly with the response from reference modules which are calibrated in a CERN test-beam.

2. The signal from each calorimeter is corrected for attenuation of the scintillation light by measuring the change in photomultiplier current as a function of the position of the Co^{60} source. The petals are mapped as a function of radius and azimuthal angle, $f(r,\phi)$, and the gondolas are mapped as a function of horizontal position and azimuthal angle, $f(x,\phi)$.

3. During a run, the gains of the electronics chain are monitored using a laser system. A laser provides light to diffusion boxes which convey the light via optical fibres to each of the detector photomultipliers and to monitor photomultipliers and photodiodes. The detector signals are compared directly with the signals seen by the monitor system, which is calibrated using Am^{241} sources. Laser runs are taken almost daily between beam periods.

4. There is a measurement using a Co^{60} source before and after each run to determine the effect of scintillator ageing, and the data is subsequently corrected off-line. The total drop in light output from scintillator ageing between 1981 and the end of 1985 was about 50%.

The uncertainty on the absolute energy calibration is about 3%, which mainly arises from the uncertainty on the test-beam energy.

The performance of the central electromagnetic calorimeters has been tested using prototype modules in CERN test-beams. For the gondolas, the resolution in energy and azimuthal shower position has been measured to be

$$\sigma(E)/E = 15\%/\sqrt{E} \text{ (E in GeV)}$$

$$\sigma(\phi) = 24\%/\sqrt{E} \text{ (E in GeV)}$$

For the bouchons,

$$\sigma(E)/E = 20\%/\sqrt{E} \text{ (E in GeV)}$$

The position detectors can be used to reconstruct the transversal electromagnetic shower profile by measuring the total charge collected by the proportional chambers. The energy resolution of the tubes is

$$\sigma(E)/E = 170\%/\sqrt{E} \text{ (E in GeV).}$$

The resolution on the measured position of a localised electromagnetic shower using the position detectors varies from 1cm at 5 GeV to 0.3cm at 92 GeV.

3.5 The Central Hadron Calorimeters

Hadronic showers are induced by strongly interacting incident particles, and are considerably more complex than electromagnetic showers. The longitudinal development of hadronic showers is determined by the interaction length, related to the mean free path of a strongly interacting particle in the calorimeter material. Hadronic calorimeters have a poor energy resolution because of two intrinsic features of hadronic showers [17]:

1. A large fraction of the energy of the hadronic shower cannot be measured because it is used in the breakup or excitation of nuclei. This process has large event-to-event fluctuations.

2. The hadronic shower produces large numbers of π^0s which do not interact strongly, and there are large event-to-event fluctuations in their numbers.

In UA1, the iron return yoke of the dipole magnet is instrumented to act as a hadron calorimeter [22]. The central hadron calorimeters consist of two parts called the C's and the I's in reference to their shape. Figure 28 shows a C module, and details the magnet coil, the gondola electromagnetic calorimeters and the locations of the gondola and C module photomultipliers. Figure 29 details one of the I modules. The C's are situated behind the gondolas and cover the angular region $25^0 < \theta < 155^0$ whereas the I's are behind the bouchons and cover the ranges $5^0 < \theta < 25^0$ and $155^0 < \theta < 175^0$. There are a total of 16 C's (8 on each side) and 12 I's (6 at each end).

The C's and I's both consist of 1cm thick sheets of scintillator sandwiched between 5cm sheets of iron. There are 16 such layers in the C's (5 interaction lengths) and 23 layers in the I's (7 interaction lengths). The I's have more iron because there is a greater flux of particles at small angles with respect to the beam axis. The size of the scintillator plates effectively divides the hadron calorimeters into cells, and the size of these cells (0.9m × 0.8m in the C's; 0.9m × 0.9m for $\theta > 15^0$, 0.5m × 0.4m for $\theta < 15^0$ in the I's) determines the position resolution of the hadronic depositions. The I's have an improved granularity below $\theta < 15^0$ because of the larger flux of particles in this region. The scintillator sheets are read out at two opposite edges (except for the 0.5m × 0.4m sheets of the I's which are read out along one edge only because of lack of space) via BBQ wavelength-shifters, and transmitted by waveguides to photomultipliers which are mounted on the back face of the iron. The scintillation light is summed together to form two samplings in depth, which helps give an indication of the penetrating power of particles and is useful in muon identification.

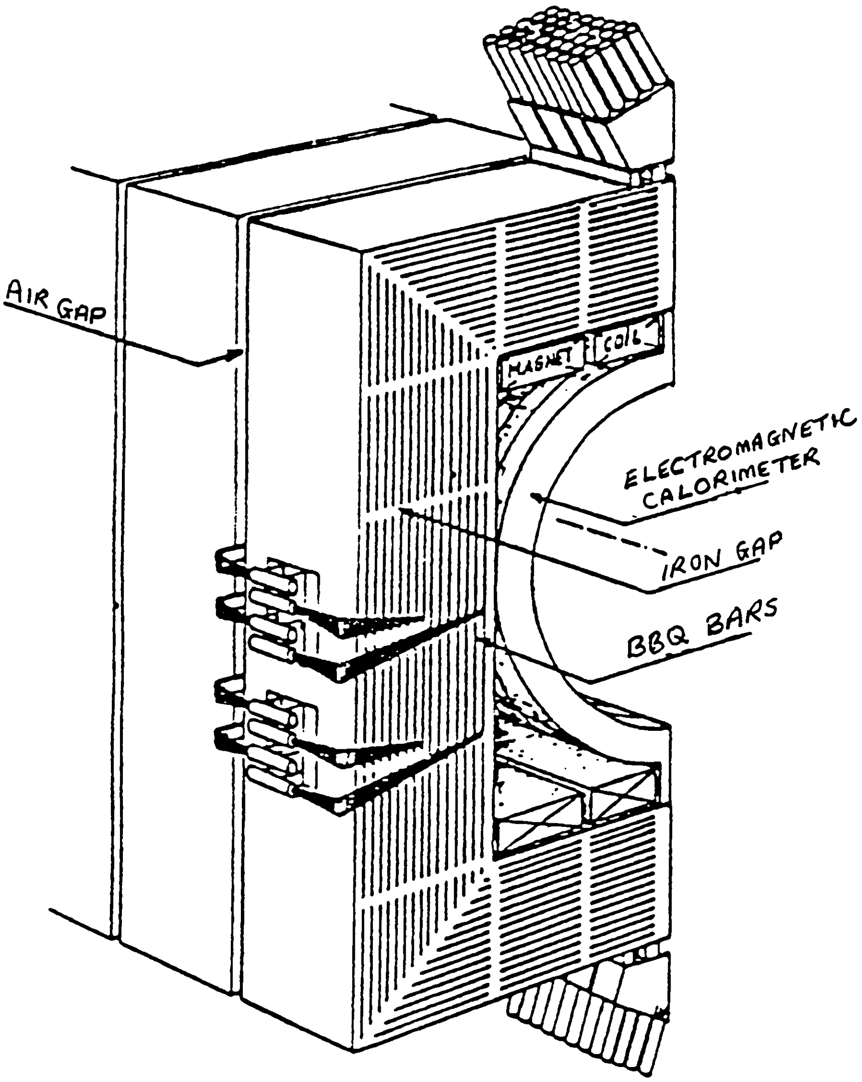

Figure 28: The C Hadron Calorimeters

Each of the modules were originally calibrated using both accelerator muons and cosmic rays. During these tests the gains of the electronics channels were set by exposing the scintillators to Ru^{106} radioactive sources. After their installation as part of the UA1 detector, the gains of the electronics channels were reset using the Ru^{106} sources so that

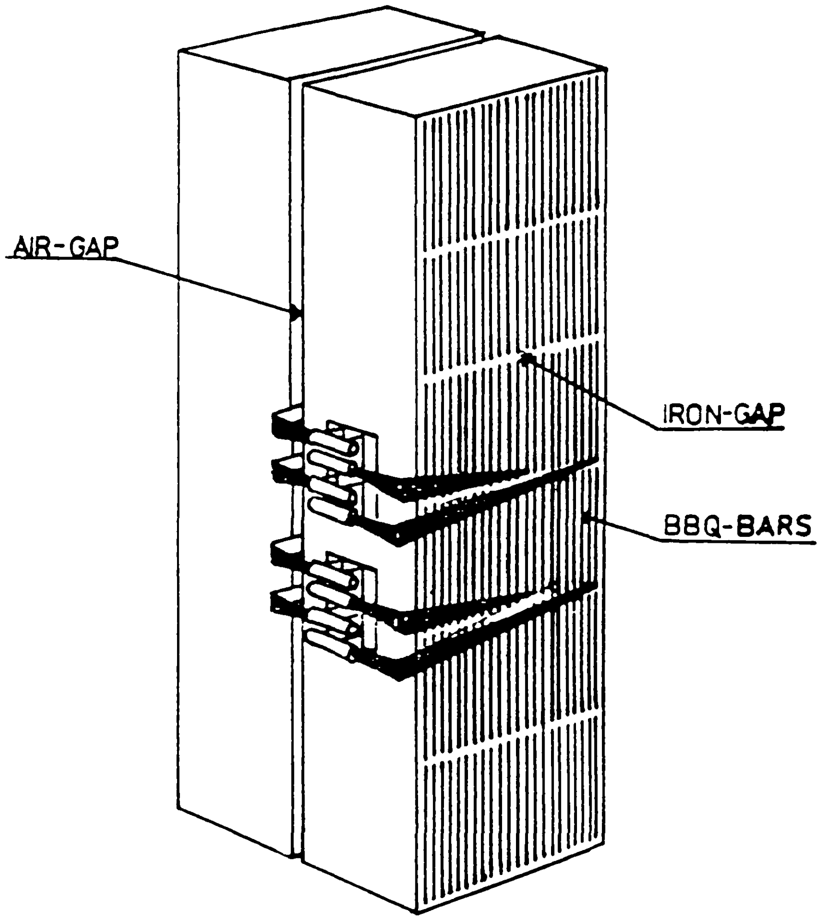

Figure 29: The I Hadron Calorimeters

the calibration constants are still valid. All subsequent monitoring of the response of the modules has been performed by passing light from a UV nitrogen laser along quartz fibres to the centre of each plate. The laser light enters the scintillator plates via prisms made of UV transmitting perspex, which were fixed to the centre of each plate before they were wrapped and inserted into slots in the iron. During a laser run, the detector signals are compared with the signals from reference photomultipliers and plates underneath the UA1 detector which are attached to both the lasers and to radioactive sources. The performance of the hadron calorimeters has been measured using small test modules in CERN test-beams. The energy resolution of the hadron calorimeters is

$$\sigma(E)/E = 80\%/\sqrt{E} \text{ (E in GeV)}$$

3.6 The Muon Chambers

Beyond the return yoke of the dipole magnet is 60cm of iron which acts as a further filter for the muon chambers. The muon chambers cover a total area of 500m^2 around the outside of the iron, and consist of large drift chambers arranged in four pairs of orthogonal planes as shown in Figure 30.

Due to space restrictions there are only two pairs of parallel planes underneath the UA1 detector. The drift chambers comprise a total of 5200 sense wires with a length of 6m and a maximum drift length of 7.5cm. The 62cm between the two sets of drift chambers provides a lever arm from which the trajectory of the muon track can be projected back. The momentum of the muon is measured by the magnetic curvature of its track in the central detector. The spatial resolution of the muon chambers is ~300μm.

In UA1, muon acceptance is limited due to the fact that the muon chambers cover only a fraction of the solid angle with respect to the beam crossing point. The azimuthal coverage is about 70% for the central region ($|\eta| < 1$) and about 80% in the forward region ($1 < |\eta| < 2.3$).

3.7 The Forward Region

There are more proportional chambers and calorimeters [23] to cover the angular region below $\theta < 5^0$ as shown in Figure 31. The range $0.7^0 < \theta < 5^0$ is covered by the forward electromagnetic calorimeters. Directly behind the forward electromagnetic calorimeters are two magnets which compensate for the effect of the UA1 dipole magnet on the proton

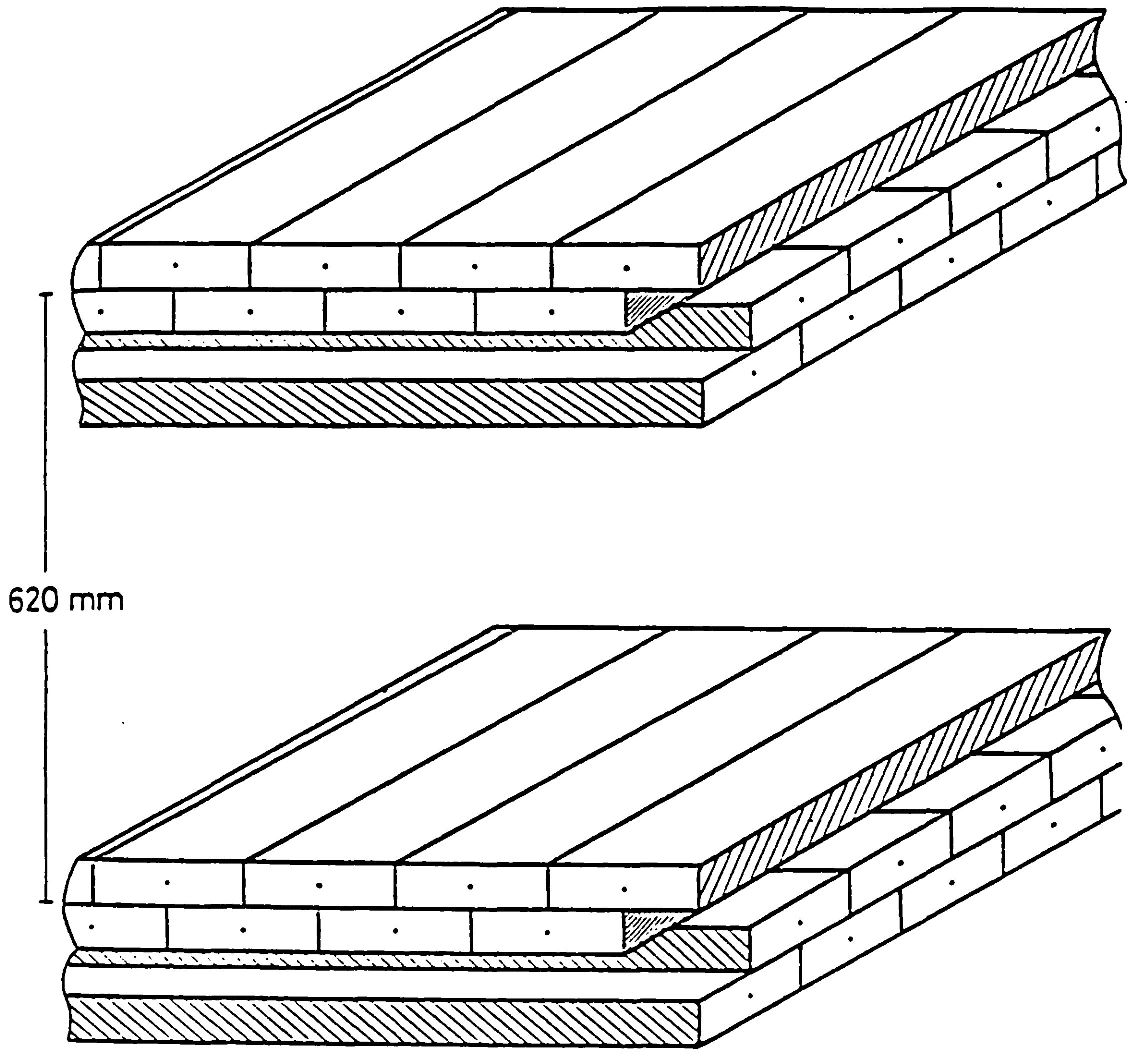

Figure 30: The Muon Chambers

and antiproton orbits. The magnets are instrumented to form hadron calorimeters, and are called calcoms in reference to their double role as both calorimeters and compensating magnets.

The forward electromagnetic calorimeters are divided radially into 8 segments (each with an opening angle of 45^0 in ϕ) and are divided into 4 sections along the beam direc-

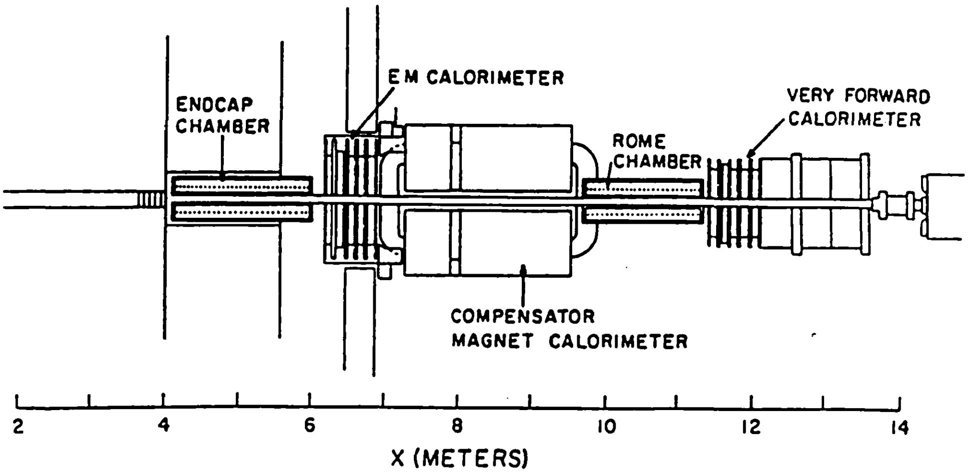

Figure 31: The Forward Region

tion. Each section is 7.5 radiation lengths thick and comprises a sandwich of lead and scintillator sheets, each 3mm thick. The forward electromagnetic calorimetry therefore has a total of 30 radiation lengths. Scintillation light is channelled to photomultipliers via BBQ wavelength-shifters. Between the first and second segments there is a position detector consisting of a set of 4 proportional chambers. The chambers consist of an anode wire plane between two cathode wire planes, and each chamber is tilted at an angle of 45^0 with respect to its neighbour to enable the position of the shower to be determined.

The calcoms are also divided radially into 8 modules, but have 6 segments in depth. Each segment is 1.7 interaction lengths thick, and comprises 8mm thick sheets of scintillator sandwiched between 40mm thick sheets of steel. Readout is again via BBQ wavelength-shifters. Between the first and second segments there are 4 proportional counters identical to those on the forward electromagnetic calorimeters.

The angular region $0.2^0 < \theta < 0.7^0$ is covered by the very forward detectors, which are essentially the same as the forward detectors except that they do not provide a magnetic field.

3.8 The UA1 Trigger

At a luminosity of 10^{29} cm^2s^{-1} the interaction rate of the SPS collider is about 5kHz. Due to the limited speed of the tape drives, the maximum rate at which the ~120-kbyte UA1 events can be written to tape is about 5Hz. Clearly some reduction in the rate of data must be applied at the stage prior to the data-acquisition. Only a fraction of the $p\bar{p}$ cross-section forms potentially interesting physics, so the UA1 trigger was designed [24] to reduce the data down to a manageable rate while maximising the number of events read out that are of particular interest.

The UA1 trigger system in fact consists of 4 parts:

1. The Pretrigger
2. The Calorimeter Trigger Processor
3. The Muon Trigger Processor
4. The Final Level Logic

The layout of the trigger system is shown in Figure 32.

3.8.1 The Pretrigger

The pretrigger is essentially a $p\bar{p}$ interaction trigger which is used to reject backgrounds such as beam-gas interactions and cosmic rays. There are no conditions imposed on the final event topology, so the pretrigger is sometimes called a minimum-bias trigger. The pretrigger also acts as a direct online luminosity monitor.

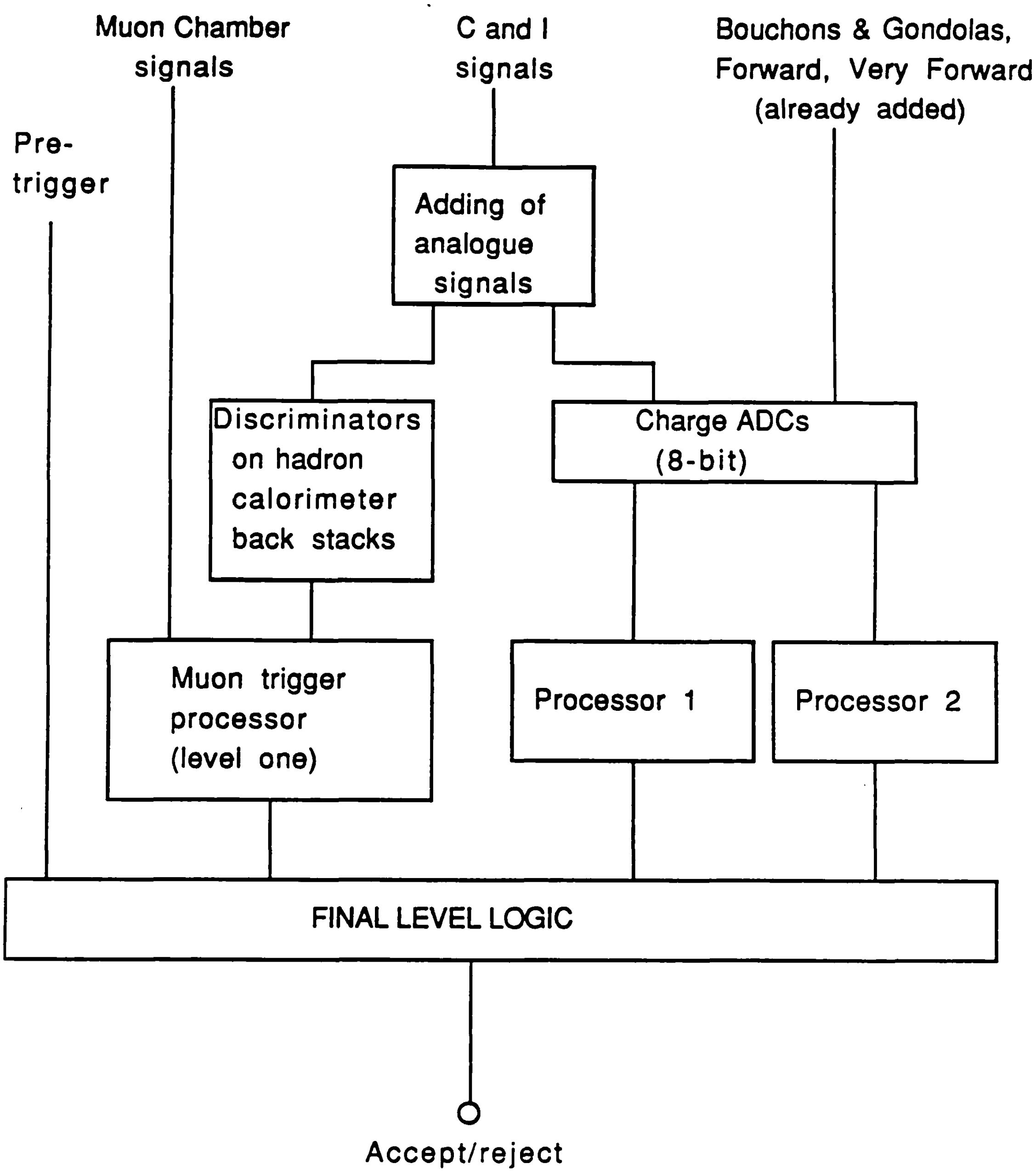

Figure 32: The UA1 Trigger System

Signals for the pretrigger come from four pairs of scintillator hodoscopes which are centred on the beam axis. The angular coverage of the hodoscopes and their distance from the centre of the UA1 detector are summarised in Table 6.

Table 6: The pretrigger hodoscopes

Name	Distance from interaction point	Angular coverage (steradians)
Bouchon	2.9m	1.2 SR
SPS	6.2m	0.015 SR
Calcom	6.3m	0.042 SR
Very Forward	11.0m	0.002 SR

The logic demands that at least one counter in each side of the experiment is fired, with the timing of the AND gate sufficiently tight to reject interactions that do not originate from the centre of the apparatus. The pretrigger is also used as monitor of the beam quality. The beam crossing position and beam-gas contamination is measured directly by a timing display of the SPS hodoscope, using an OR of one arm as a start of the timing pulse and the other arm as a stop.

3.8.2 The Calorimeter Trigger Processor

The calorimeter trigger processor uses two independent processors to trigger on various modes of energy flow within the calorimeters. The signals from the 2440 calorimeter photomultipliers are grouped together into 288 trigger channels which are digitized to 8-bit precision .. One of the processors multiplies the signal from each trigger channel by a calibration constant after pedestal subtraction to convert pulse height to energy. It is sometimes more relevant to look at the energy flow in the plane transverse to the beam axis, so the second trigger processor also weights the trigger channels by $\sin\theta$, where θ is the angle subtended at the interaction point between the relevant calorimeter cell and the beam axis. The energy or transverse energy signals are then added and/or compared within the relevant processor to form the various trigger conditions. Each processor can determine eight different trigger conditions of which some examples are listed below:

1. A total transverse energy trigger in which the scalar sum of transverse energy of all trigger channels (represented by the shaded region of figure 33) must exceed a threshold;

2. An electron trigger which requires the transverse energy in two adjacent electromagnetic trigger channels (two gondolas or petals) to exceed a threshold (see Figure 34);

3. A jet trigger which requires that the transverse energy of a localized deposition in both electromagnetic and hadronic calorimeters (For example in 8 gondolas and the 2 C's behind the gondolas as shown in Figure 35) exceeds a threshold;

4. An electron pair trigger – similar to 2) but requiring a reduced transverse energy threshold;

5. A missing energy trigger which requires that the energy imbalance in the ±z direction is greater than some threshold.

3.8.3 The Muon Trigger Processor

The muon trigger processor attempts to trigger on muons produced directly by the $p\bar{p}$ interaction ('prompt' muons) while vetoing background processes like punchthrough by hadrons, cosmic rays, or muons from decays of the $\pi^{\pm}$ or $K^{\pm}$. Prompt muons are flagged in the UA1 detector by a track in the central detector, a small energy deposition (corresponding to the passage of a minimum ionising particle) in both of the two samplings of the central hadron calorimeters, and a track in the muon chambers which points back to the interaction point.

The hadronic energy deposition and the detection of hits in the muon drift chambers are processed by the so-called first level muon trigger. Trigger events are then passed on to the second level trigger which measures drift-times in the muon chambers and tries to

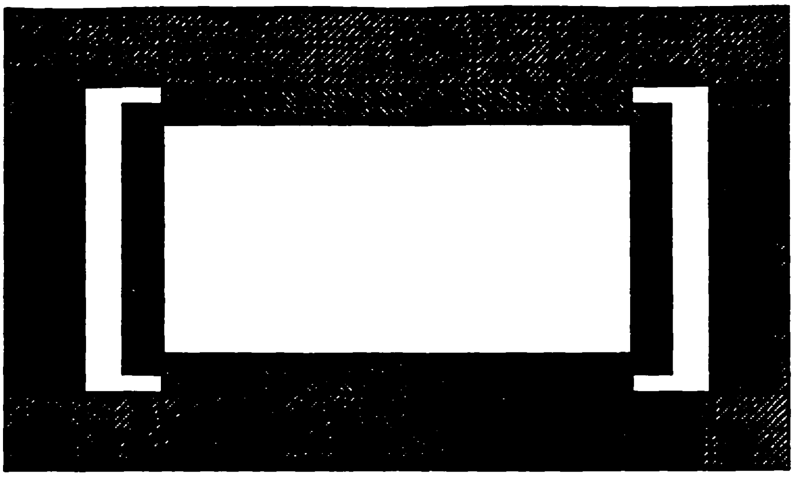

Figure 33: The ΣE_t Trigger

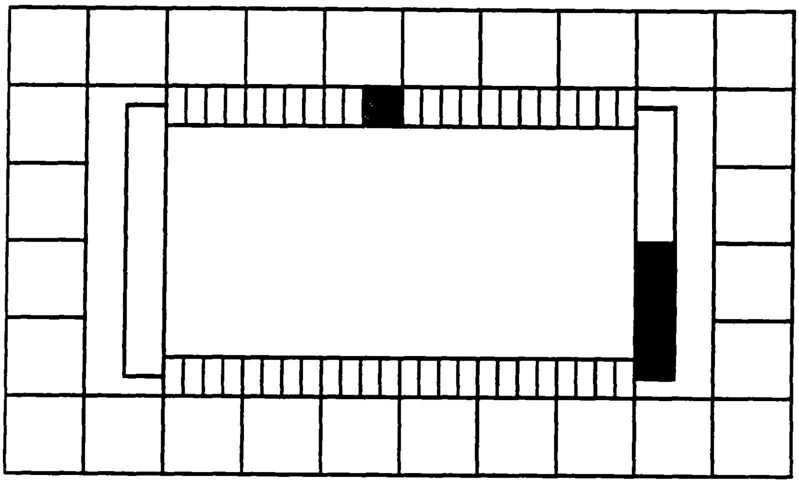

Figure 34: The Electron Trigger

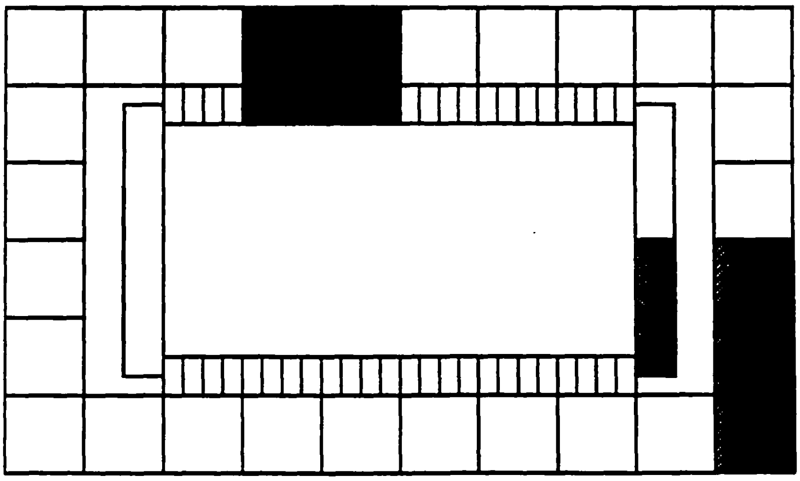

Figure 35: The Jet Trigger

project the track back to the interaction point. The event is selected if the reconstructed track passes close to the origin with a momentum (measured in the central detector) greater than about 3 GeV/c.

3.8.4 The Final Level Logic

In the Final Level Logic, the results of the calorimeter trigger processor, the muon trigger processor, the pretrigger and any other external trigger requirements are ANDed with a trigger bit pattern to determine whether the event should continue to be processed. In addition to the combinations of calorimeter and muon triggers, there are also pion and cosmic ray triggers. The pion triggers are used to select hadronic showers that start early in the central electromagnetic calorimetry, in which the single electron trigger is satisfied but with a punchthrough of energy into the front sampling of the hadronic calorimeters. The pion trigger is useful in calculating the background to electron identification. Cosmic rays are used for calibration and for alignment of the central detector. The cosmic ray trigger demands a coincidence between large counters placed on opposite sides of the UA1 detector.

3.9 The UA1 Data-Acquisition

The data-acquisition system (DAS) in UA1 uses two computing systems which each consist of a Nord-100 processor and a Nord-500 processor. The two systems are identical; the so-called 'A'-machine runs the data-acquisition, and the 'B'-machine runs the bulk of the monitoring jobs. Data is acquired via REMUS, a subset of CAMAC that gives fast operation in multibranch systems.

After the final level trigger logic, there is some further filtering of events by five IBM 168 emulators (originally only four 168E's in the 1983 running). The 168Es process part of the event and are used to flag the more interesting physics (for example Z^0 or $W^\pm$

candidates). There is a sixth emulator which is used to spy on the emulator system and monitors their performance on-line. Events flagged by the 168Es are written to a special tape called the 'Express-line' which takes priority in off-line processing and analysis. The layout of the UA1 data acquisition system is shown in Figure 36.

3.10 The Data Processing Chain

There were some 10^6 electron triggers alone accumulated by the UA1 detector up to the end of 1985. Although only a small percentage of these events were validated and processed, it was still a formidable task in terms of both CPU time and the huge numbers of tapes required. The processing chain for raw data taken by UA1 is shown in Figure 37. Data is written either to express-line or normal tapes. The events written on express-line tapes have been selected by the 168Es as special events (eg $W^{\pm}$, Z^0 candidates) and take priority in processing. The first stage of processing is the PREPRO stage, which

1. orders the data into HYDRA [25] format,
2. subtracts pedestals and applies calibration correction factors to the measurements of calorimeter energies and central detector drift-times,
3. removes zeros in the data from those parts of the detector that were not hit.

After the PREPRO stage, there are ~1000 events per 6250 bpi tape.

The next stage in the processing is BINGO, which essentially reconstructs the event by

1. applying final calibration corrections,
2. performing track-finding in drift chambers,

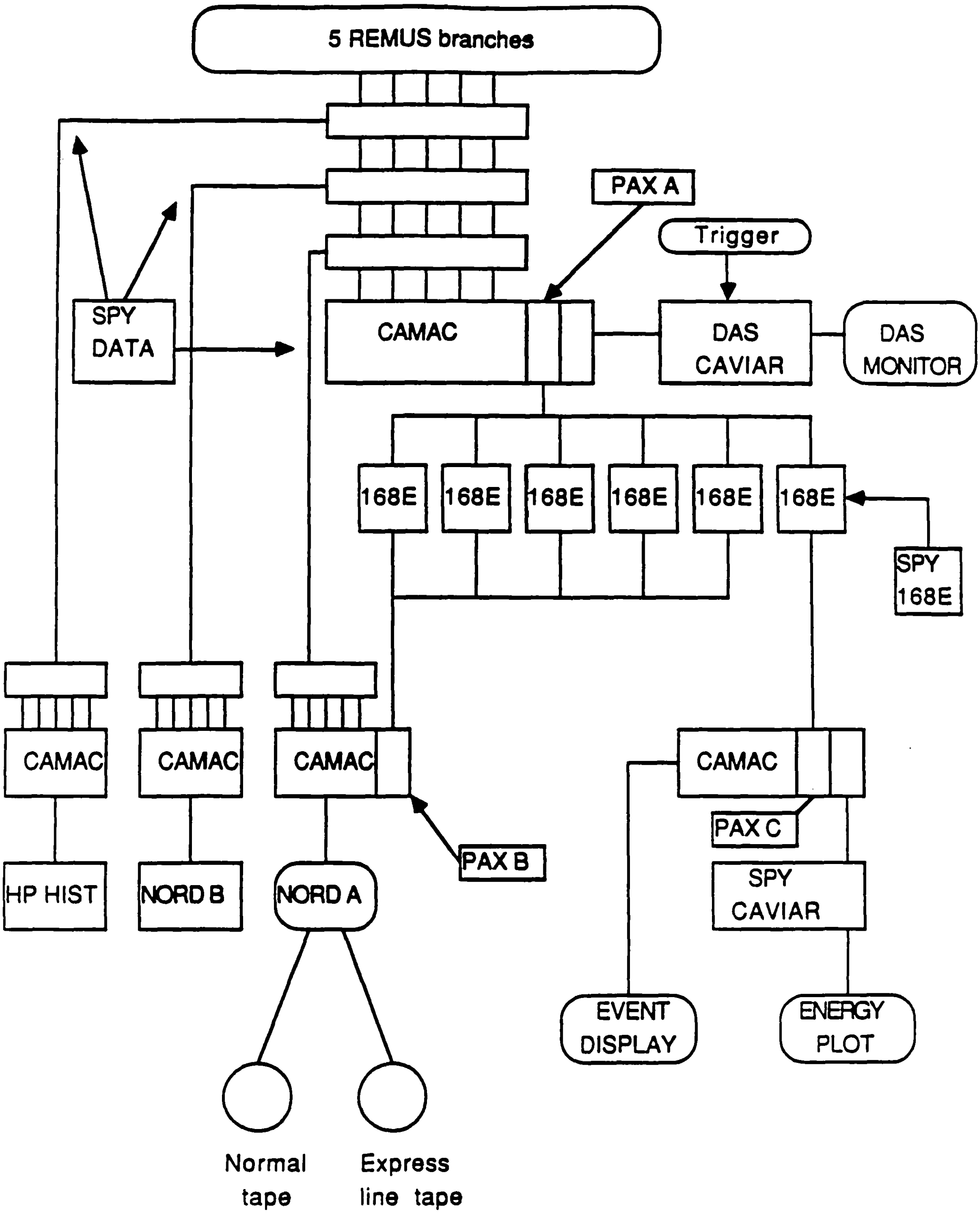

Figure 36: The UA1 Data-Acquisition System

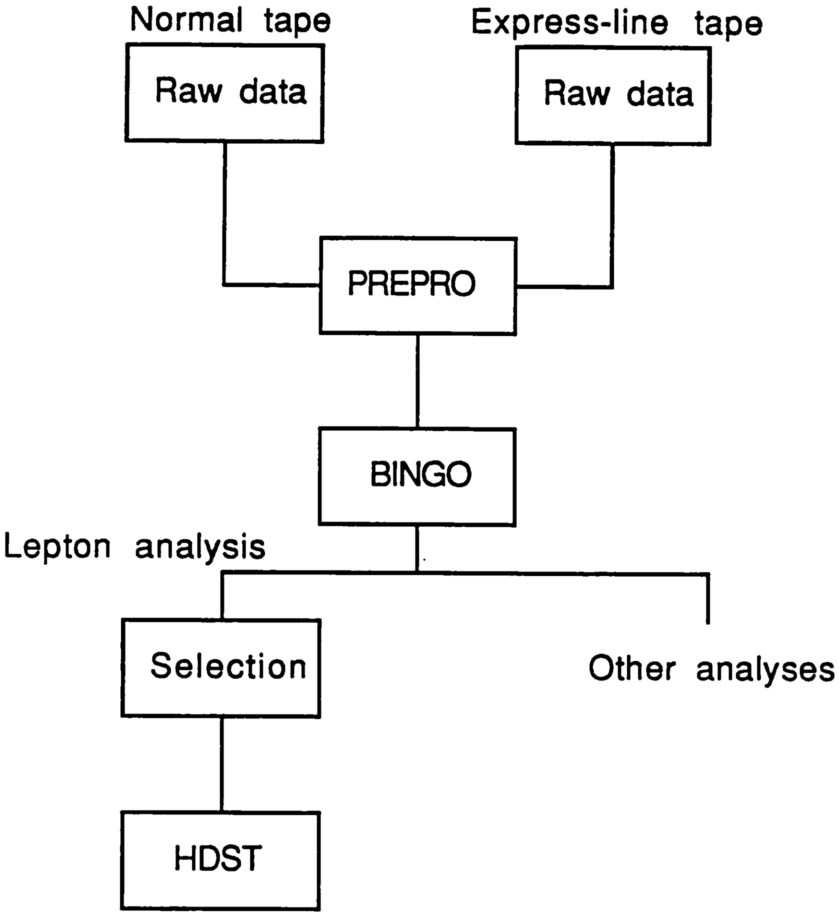

Figure 37: The Data Processing Chain

3. looking for correlations, for example between CD tracks and calorimeter depositions, or between CD tracks and hits in the muon chambers.

The BINGO stage is the most CPU-intensive (~15 CPU seconds per event) and therefore only express-line events and those events recognised at the PREPRO stage as being of interest are BINGO processed. The extra information provided by BINGO increases the event size so only 400-500 events fit on a 6250 bpi tape.

There is in general some further processing after BINGO to ease the subsequent analysis. For example, the selection stage identifies leptons, reconstructs jets, calculates the missing transverse energy etc, and raises new HYDRA banks to provide the extra information. To reduce the number of tapes required the data used for analysis in this thesis was in the form of HDSTs (HYDRA data summary tapes). Not all of the event information provided by BINGO is necessary for the electron analysis, so HDSTs are produced whereby superfluous HYDRA banks are dropped and extra information on electron and jet kinematics is added. There were typically 1000 events per 6250 bpi tape after the HDST stage.

4. THE ELECTRON DATA SAMPLE

4.1 Introduction

Electron identification in UA1 is based on a charged track in the central detector that points to a deposition of energy in the central electromagnetic calorimeters. The electromagnetic shower is expected to be mostly contained within the 27 radiation lengths of the lead/scintillator electromagnetic calorimeter with only a small, if any, residual punchthrough of energy into the hadron calorimeters. However, such a signature is not unique to electrons; a possible source of electron misidentification would be a QCD jet in which the charged particle multiplicity fluctuates down to a single particle. The central electromagnetic calorimeters are 0.8 interactions length thick, so a single charged hadron that arises from a jet fluctuation can shower early in an electromagnetic calorimeter and simulate an electron. The rate at which QCD jets are produced at the SPS collider is several orders of magnitude higher than electron production, so the background to electron identification from jet fluctuations is expected to be substantial. A reduction of the background to a tolerable level ($< 10\%$ of the electron signal) requires the full rejection power of the UA1 detector with very stringent cuts on the transverse momentum, isolation and shower profile of the electron candidates. Moreover, the background from electron misidentification is expected to rise rapidly if any of these cuts are relaxed.

The data sample used for analysis in this thesis is based on events selected by the UA1 electron trigger, which requires that the measured transverse energy in two adjacent cells of the central electromagnetic calorimeters is greater than 10 GeV. An on-line selection using 168E processors (which required a rough isolation from any other depositions of energy in the calorimeter) selected about 10^6 electron triggers during the runs of 1983, 1984 and 1985, which represented an integrated luminosity of $690 \mathrm{nb}^{-1}$ as summarised in Table 7.

Table 7: *Electron data recorded by the UA1 experiment*

Year	$\sqrt{s}$	$\int \mathscr{L} dt$
1983	546 GeV	$120 nb^{-1}$
1984	630 GeV	$263 nb^{-1}$
1985	630 GeV	$307 nb^{-1}$
Total:		$690 nb^{-1}$

The PREPRO stage of off-line processing (described in Chapter 3) determined whether the transverse energy of the calorimeter deposition is greater than 10 GeV after calibration constants are applied, and searched for an associated track in the central detector. The events that passed this validation were then fully processed.

This chapter describes the cuts used on the data sample to enhance the electron signal relative to the background from jet fluctuations. The second part of the chapter summarises the methods used in estimating the background that still remains in the electron sample after these cuts are implemented. A second source of background to the electron signal which arises from the conversion of photons to e^+e^- pairs in the UA1 detector is also discussed.

4.2 Electron Identification in UA1

The electron trigger events that pass the PREPRO stage of data processing contain either genuine electrons or jet fluctuations that give rise to a $\pi^\pm$ which may be accompanied by one or more π^0s. Cuts are imposed on this data sample to enhance the number of electron events. Many of the cuts are based on test-beam results in which the response of central electromagnetic calorimeter modules was measured in both electron and pion test beams. The electron candidates used for analysis in this thesis satisfy the following selection criteria:

1. We require that the electromagnetic transverse energy of the electron candidate satsifies:

   $$E_t^{em} \geq 15 \text{ GeV}$$

   and that the electromagnetic energy deposition is contained within two adjacent gondolas or petals.

2. The energy deposition must be associated with a single track in the Central Detector with

   $$P_t^{CD} \geq 10 \text{ GeV/c}$$

   Sometimes the tracking algorithm can correlate random digitizings in the central detector, or reconstruct a single track fom two unrelated shorter pieces of track. The quality of the tracks of the candidate electrons is checked using the MEGATEK[1] display of Figure 38, which shows a plot of the reconstructed particle trajectory through the track residuals in the XY plane.

   We require a good match between the reconstructed trajectory and the track residuals throughout the length of the track, and require a track length greater than 30 cm with at least 20 digitizings.

3. There must be a good match between the direction of the track and the location of the energy deposition in the calorimeter. The measurement of azimuthal angle, ϕ, from pulse height division of the gondola photomultipliers or of the position of the shower from the bouchon position detectors must agree with the impact of the track to within 3σ.

---

[1] The MEGATEK is an interactive graphics facility on which a 2-dimensional view of a 3-dimensional representation of the UA1 detector can be used to study event topologies etc.

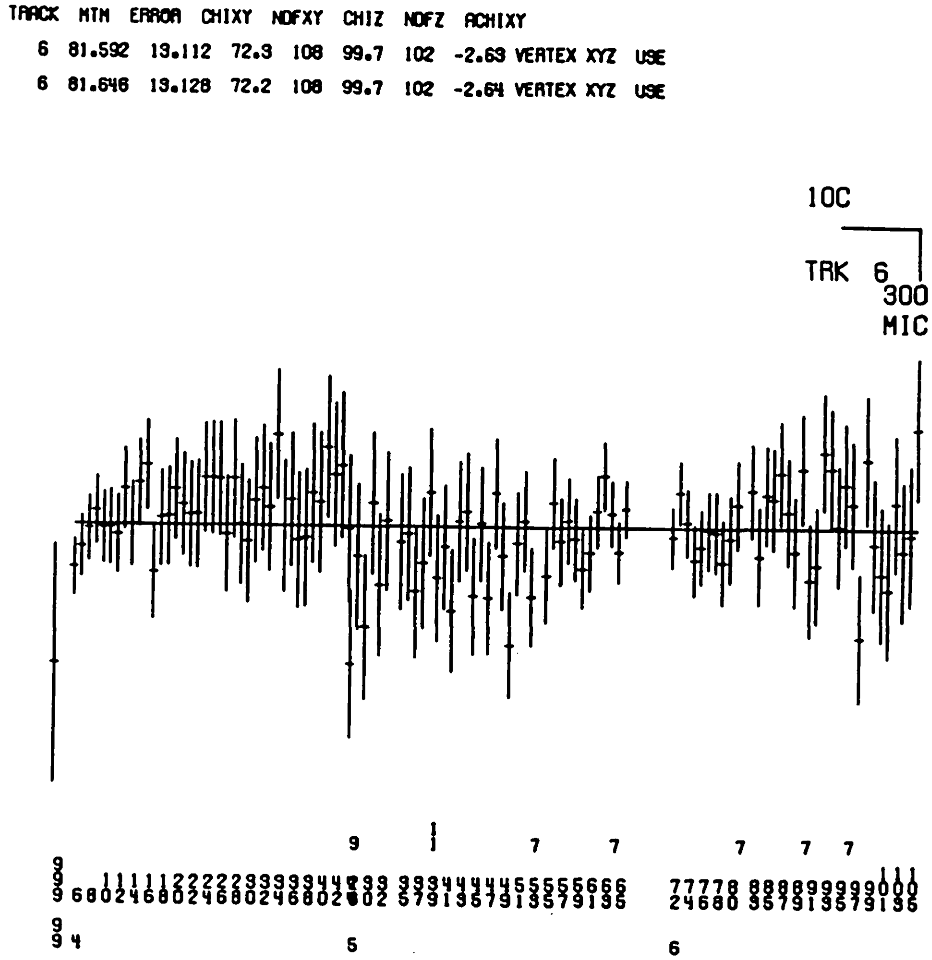

```
TRACK  MTM    ERROR  CHIXY NDFXY CHIZ NDFZ RCHIXY
  6  81.592  13.112  72.3   108  99.7  102  -2.63 VERTEX XYZ  USE
  6  81.646  13.128  72.2   108  99.7  102  -2.64 VERTEX XYZ  USE
```

Figure 38: Residuals of a Central Detector track

4. To ensure that the electromagnetic shower of the electron candidate can be properly reconstructed, the energy deposition of the electron candidate must be well separated from any other hits in the calorimeter. We require:

   $$\Sigma(P_t - P_t^{el}) \leq 2.5 \text{ GeV in two gondolas or petals}$$

   The reconstruction of an electromagnetic shower in the gondolas is checked using the MEGATEK display of Figure 39, which represents a cross-section through four gondolas in the plane transverse to the beam axis.

   The measured energy and azimuthal position of the energy deposition in the four samplings of each gondola is shown. The solid arrow represents a fit to the posi-

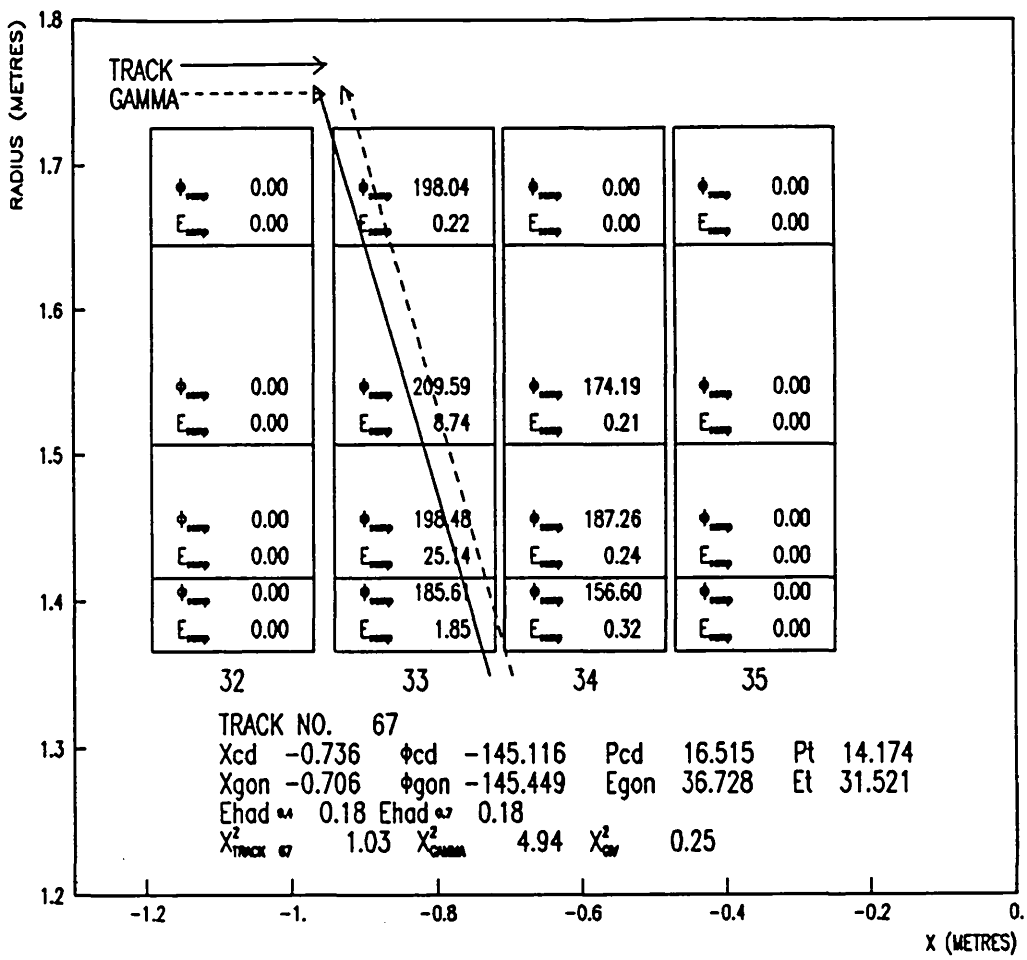

Figure 39: Reconstruction of an electromagnetic shower in the gondolas

tion of the electromagnetic shower, taking into account both calorimeter information and the direction of the central detector track. The dashed arrow only uses the calorimeter information. We require a good χ^2 fit to the shower profile in the gondola, and that the four samplings in depth are compatible in their measurements of the azimuthal shower position:

$$\Delta\phi(\text{between the 4 samplings}) \leq 3\sigma$$

We also require that the width of the electromagnetic shower reconstructed by the bouchon position detectors (see for example Figure 40) satisfies $\sigma_y, \sigma_z \leq$ 6cm.

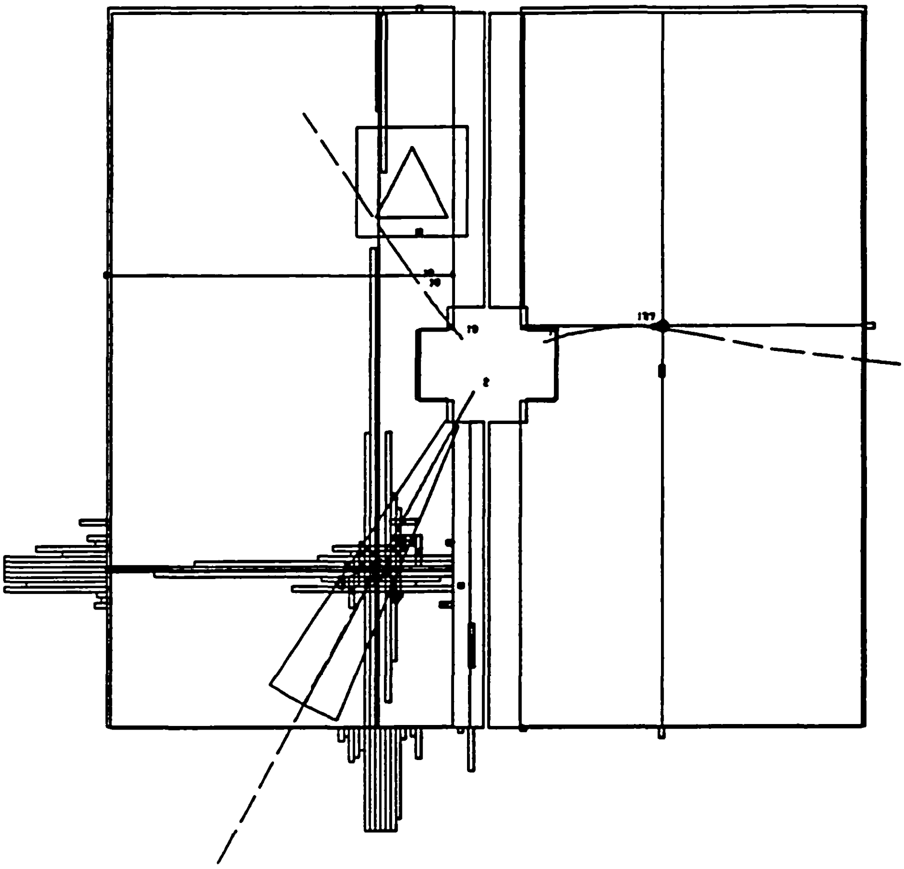

Figure 40: Reconstruction of an electromagnetic shower in a bouchon

5. The hadronic punchthrough of the shower (the energy in the hadronic cell which is crossed by an extrapolation of the CD track) must satisfy

$$E_{had} \leq 200 \text{ MeV}$$

Test beam results using 20 GeV e^- and π^- beams have shown that 94% of electrons satisfy $E_{had} \leq 200$ MeV, and 95% of pions satisfy $E_{had} \geq 1$ GeV [26].

6. A parameter has been developed from an analysis of test-beam data that can help distinguish electromagnetic and hadronic longitudinal shower profiles in a gondola or petal using the energy measurements of the four samplings in depth. $\chi^2{}_R$ is defined as:

$$\chi^2_R = \frac{(E_{S1} - \bar{E}_{S1})^2}{\sigma^2_1} + \ldots\ldots\ldots\ldots + \frac{(E_{S4} - \bar{E}_{S4})^2}{\sigma^2_4}$$

$$+ \frac{(E_{S1+S2} - \bar{E}_{S1+S2})^2}{\sigma^2_{12}} + \ldots\ldots\ldots + \frac{(E_{S3+S4} - \bar{E}_{S3+S4})^2}{\sigma^2_{34}}$$

where

E_{S1} is the energy measured in the first sampling,

$\bar{E}_{S1}$ is the mean energy measured in the first sampling for a given incident electron energy (measured by a test-beam).

Figure 41 [26] shows the distribution of $\chi^2{}_R$ for 20 GeV e^- and π^- test beams. $\chi^2{}_R$ can distinguish between the two beams: 80% of electrons and 20% pions satisfy $\chi^2{}_R \leq 35$.

The very large number of jet events necessitates a stringent cut on $\chi^2{}_R$, and we require that electron candidates in this analysis satisfy:

$$\chi^2{}_R \leq 10.$$

7. To further reduce the background from jet fluctuations, we require that there must not be any tracks of significant momentum close to the track of the electron candidate, and there must not be any significant depositions of energy in the ca-

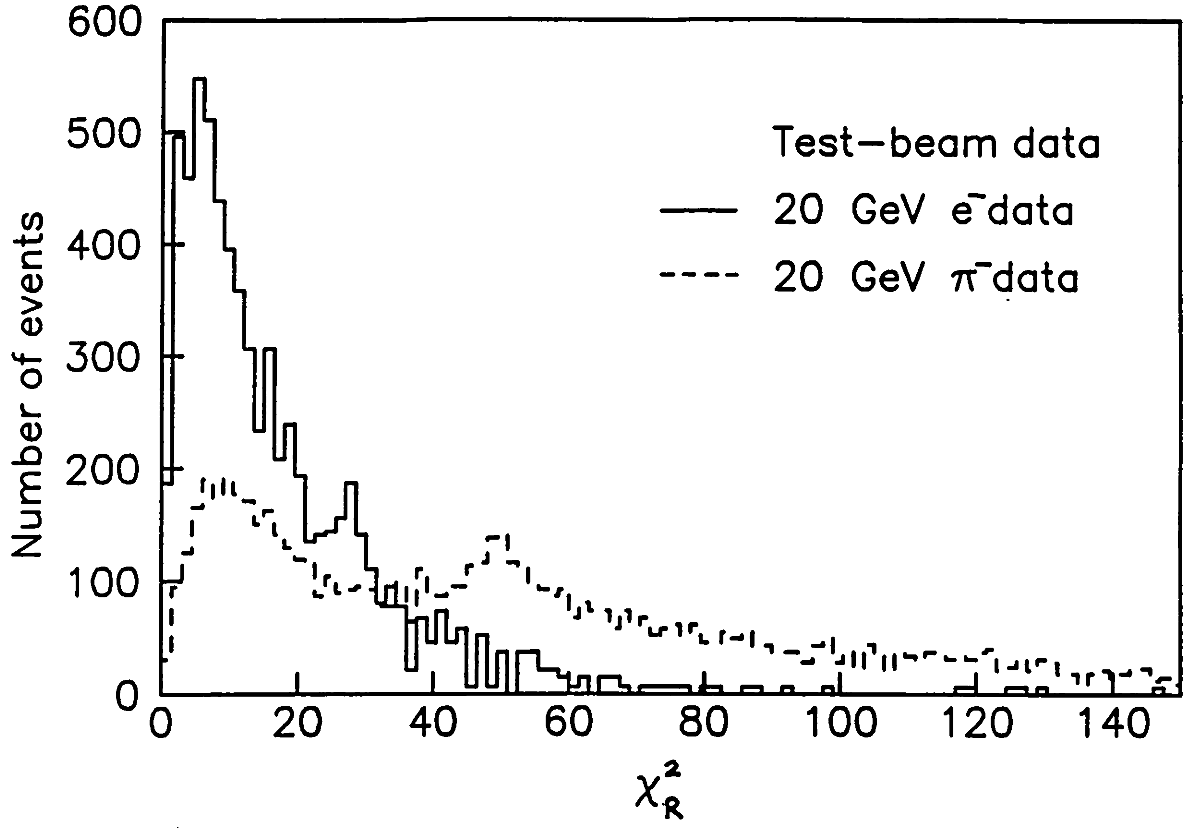

Figure 41: Distribution of $\chi^2{}_R$ *for 20 GeV test-beam data*

lorimeters close to the deposition associated with the electron candidate. The isolation of the electron candidate is measured as a function of the distance in pseudorapidity-phi (η,ϕ) space[2] from the centroid of the energy deposition. We require:

$$\sum_{\Delta R<0.4} (E_t - E_t^{el}) < 1\ \mathrm{GeV} \qquad \sum_{\Delta R<0.7} (E_t - E_t^{el}) < 10\% E_t$$

---

[2] Pseudorapidity and phi are defined in Appendix A

$$\sum_{\Delta R<0.4} (P_t - P_t^{el}) < 1\ \mathrm{GeV} \qquad \sum_{\Delta R<0.7} (P_t - P_t^{el}) < 10\%E_t$$

where $\Delta R = \sqrt{(\delta\eta^2 + \delta\phi^2)}$. The chosen values of ΔR and the degree of isolation have been optimised according to Monte Carlo predictions. The electron isolation is poorly measured because the size of the cone in ΔR is limited by the granularity of the central electromagnetic calorimeters.

8. Finally, we require a good match between the momentum measured in the Central Detector and the energy measured in the calorimeters. The energy deposited in the calorimeters from jet fluctuations will be greater than the momentum measured from the track in the CD because the π^0s accompanying the $\pi^\pm$ are invisible to the CD. We require:

$$\left| \frac{1}{P_{CD}} - \frac{1}{E_{cal}} \right| < 3\sigma$$

where P_{CD} is the momentum of the electron candidate track measured in the Central Detector, $\sigma = \sqrt{\sigma^2(1/p) + \sigma^2(1/E)}$

E_{cal} is the energy of the electron candidate measured by the calorimeters.

After the cuts listed above have been implemented, there are 280 electron candidates remaining.

4.3 Backgrounds to the Electron Signal

There are two sources of background to the high-P_t electron signal in the UA1 detector:

1. The conversions background in which the high-P_t electron originates from the asymmetric conversion of a photon to an e^+e^- pair.
2. The overlap background in which QCD jets fluctuate down to a single $\pi^\pm$ which may be overlapped by one or more π^0s.

In this section the procedures used to calculate these backgrounds are summarised.

4.3.1 The Conversions Background

The conversions background arises from the conversion of photons into an e^+e^- pair in either the beam-pipe or the walls or gas of the central detector. The photons are produced either directly via QCD processes or from the decay of π^0s.

Most conversions can be identified and removed by scanning each event on the MEGATEK. The event is removed from the sample if:

1. The electron is part of an electron pair with a mass compatible with zero,
2. The electron candidate track has twice the dE/dx expected for electrons,
3. The electron candidate track starts far from the vertex, with no track in the central detector between the vertex and the start of the track.

A typical conversion corresponding to process 1) is shown in Figure 42, which shows a MEGATEK display of the reconstructed tracks in the central detector. The $\gamma \rightarrow e^+e^-$ conversion point is marked with a cross.

There were 75 events (out of the 280 events) that were identified as conversions. These events were removed, leaving 205 events in the data sample.

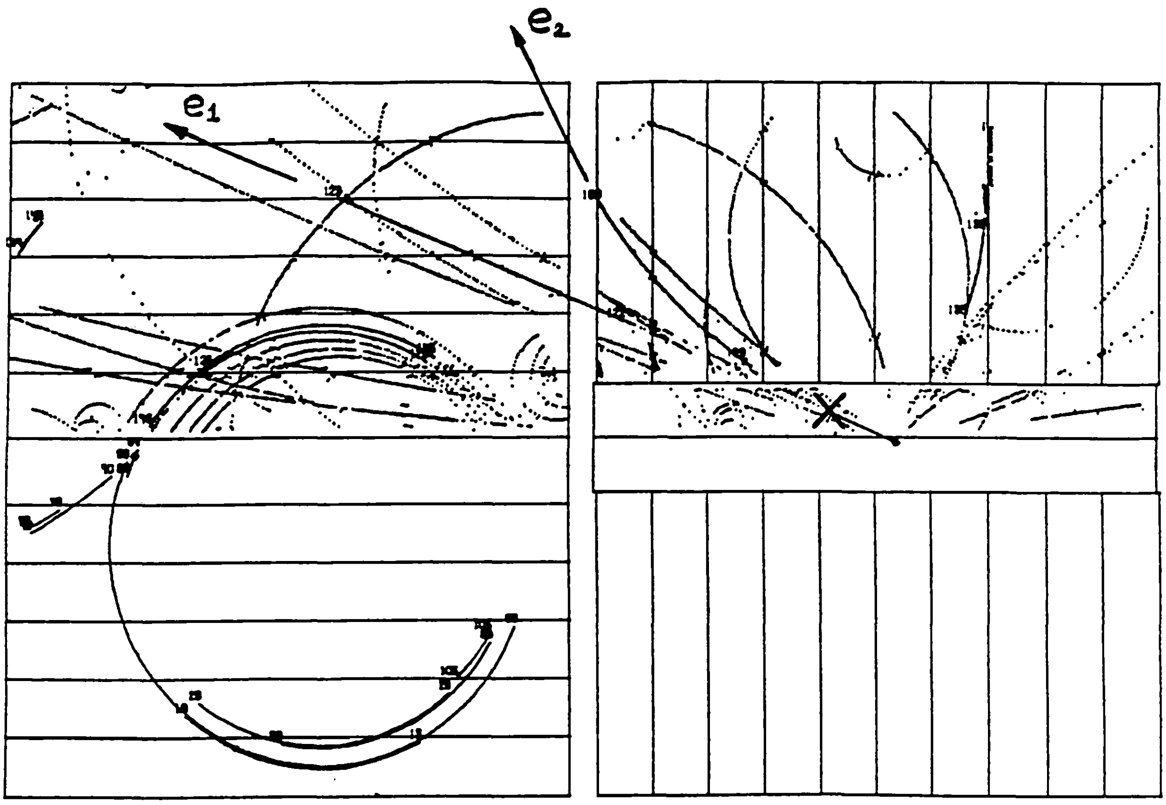

Figure 42: Run/event 18048/73. A $\gamma \rightarrow e^+e^-$ *conversion*

If the photon decays asymmetrically, and the soft electron is invisible inside the central detector (for example if the momentum of the second electron is less than about 50 MeV/c) then the conversion will not be apparent during scanning. There are two independent methods of calculating this background [27]:

1. A Monte Carlo is used to generate π^0s or photons from $p\bar{p}$ collisions, and their conversions to e^+e^- pairs are fully simulated in the UA1 detector. The events are then scanned on the MEGATEK to find the fraction of unseen conversions.

2. The probability of an asymmetric $\gamma \rightarrow e^+e^-$ conversion in the UA1 detector is calculated using the QED description of the interaction of photons with matter. The result is normalised to UA1 data using a sample of high-P_t π^0 candidates re-

corded by UA1. The high-P_t π^0 candidates satisfy a similar selection criteria as for the electron candidates, except for the requirement that there be no track in the Central Detector pointing to the electromagnetic energy deposition.

The two methods independently predict the same number of conversions (within errors), which provides confidence in the validity of the calculations. Method 1 is expected to give the most accurate prediction because it involves a full simulation of the UA1 detector: the method predicts that 2.8 ± 0.9 of the electron candidates in the data sample originate from unseen conversions.

4.3.2 The Overlap Background

In order to calculate the contribution to the data sample from $\pi^{\pm} + n\pi^0$ overlaps, we require the flux of charged pions and the probability that the pions will pass the electron selection criteria. The flux of charged pions is calculated using a sample of charged pion events taken during the 1985 run ($\int \mathscr{L} dt = 307 nb^{-1}$). Details of the pion selection and a comparison with the electron selection is shown in Table 8.

The pion selection yielded 523 events. The $\pi^{\pm} + n\pi^0$ nature of many of the pion candidates is best illustrated by a plot of (1/P) vs (1/E) as shown in Figure 43. The energy deposition measured in the calorimeters is usually greater than the momentum of the $\pi^{\pm}$ track, and is attributed to the neutral energy from the overlap of π^0s.

The pion flux must be corrected for both trigger efficiencies and for the acceptance of the selection cuts.

The E_t^{em} cut for pions is at 10 GeV, but the hardware trigger for E_t^{em} was also 10 GeV which suggests that the hardware trigger efficiency is less than 100%. As with the electron candidates, pion candidates passing the hardware trigger were processed online using the 168Es, which required a rough isolation of the energy deposition in the two gondolas or petals. The efficiencies of the hardware and 168E triggers (ε_{hard} and ε_{168E}

Table 8: Charged pion selection criteria

Parameters	Electrons	Pions
E_t^{em}	$\geq$ 15 GeV	$\geq$ 10 GeV
CD track	$P_t^{CD} \geq 10$ GeV/c $L_{xy} \geq 30$cm, $N_{pts} \geq 20$	As for electrons
Electromagnetic shape	$\chi^2_R \leq 10$ $E_{had} \leq 200$ MeV $\chi^2 \leq 2$	$E_{had} \geq 1$ GeV
Shower Reconstruction	$\Sigma P_t \leq 2.5$ GeV (in 2 gondolas/petals) ϕ matching (samplings)	As for electrons
Isolation	≤ 1 GeV within $\Delta R < 0.4$ $\leq 90\% E_t^e$ within $\Delta R < 0.7$ in both CD + CALO	As for electrons
$1/p - 1/E$	$\lvert 1/P - 1/E \rvert \leq 3\sigma$	No cut

respectively) are a function of E_t^{em}, so the pion flux has to be weighted by a factor $(\epsilon_{hard} \times \epsilon_{168E})^{-1}$ for a given E_t^{em}.

The acceptance of the selection cuts of Table 8 was found using a prototype gondola in a charged pion test-beam. π^0s were superimposed on to the $\pi^\pm$s by a Monte Carlo technique. The efficiency of the pion cuts was calculated as a function of p^π, the momentum of the $\pi^\pm$ as measured in the CD, of E^{π^0}, the energy deposited in the calorimeters by the π^0s, and of θ_{inc}, the angle of incidence of the pion. The energy of the π^0s can be calculated given the e/π response factor of the electromagnetic calorimeter which is known from test-beam data, and is a function of the fraction of energy deposited by the $\pi^\pm$ in the electromagnetic calorimeter.

The total pion flux for the 690 nb^{-1} of data can then be calculated and is given by:

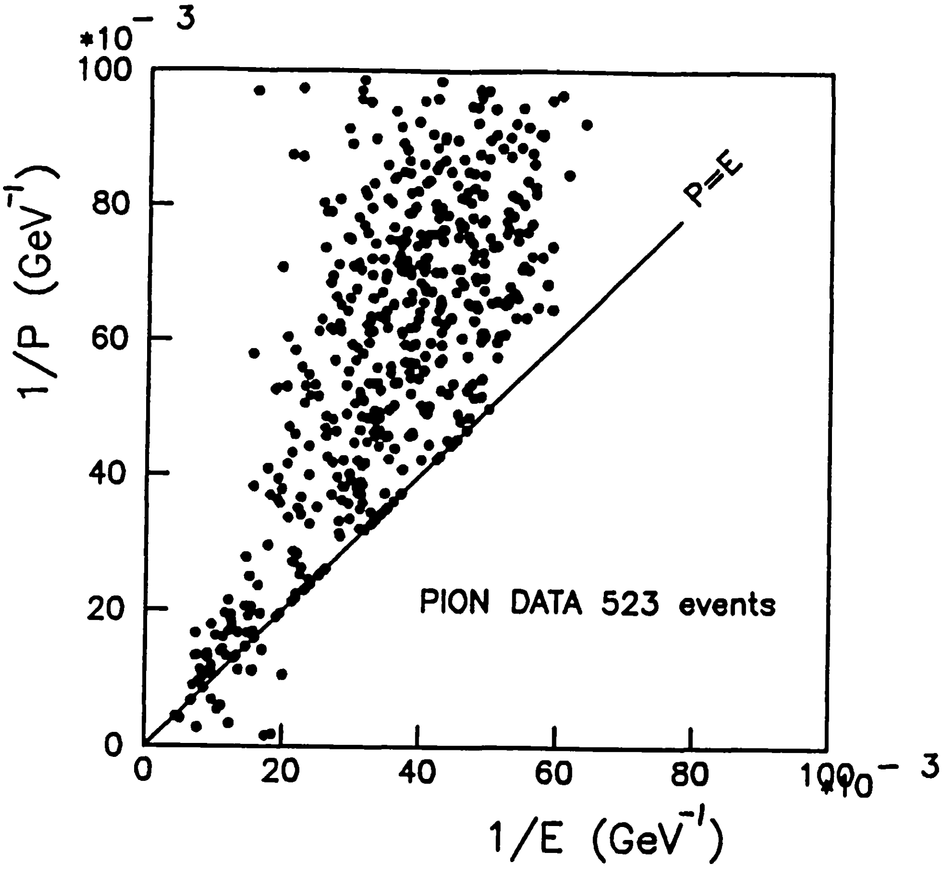

Figure 43: (1/P) vs (1/E) for the pion data

$$N_{\pi}^{tot} = N_{85} \times R / (P_{hard} \times P_{168E} \times P_{cuts})$$

where

N_{85} is the number of pion events selected in the 1985 run,

R normalises the sample to the full luminosity (R = 690/307),

P_{hard} is the probability that the cluster satisfies the hardware trigger,

P_{168E} is the probability that the cluster satisfies the 168E trigger,

P_{cuts} is the probability that the overlap satisfies the pion selection cuts.

The overlap background estimate is calculated by multiplying the total pion flux by the probability of the overlap to satisfy the electron selection, which was computed by imposing the electron cuts on to $\pi^{\pm}$ test beam data with π^0s superimposed by Monte Carlo. The finite momentum resolution of the central detector was simulated in order to find the effect of the $|(1/P)-(1/E)|$ cut. A 4-dimensional probability table is then constructed in P^{π}, E^{π^0}, θ_{inc} and $\sigma(1/P)$ which represents the probability of a pion overlap becoming a background candidate to the electron sample. To obtain the total overlap background to the electron sample, the weight of each event in the pion sample is calculated by computing the four variables and interpolating linearly in the table.

The number of events from the overlap background is predicted to be 8.3±1.3 using this method [28]. The validity of this method has been cross-checked [26] [28] by relaxing part of the selection criteria (for example E_{had}) and comparing the predicted background with the observed data rate in the region where the background contribution is expected to dominate. The data rate is observed to become compatible with predictions for the overlap background as soon as the cuts are relaxed (for example as E_{had} rises above about 600 MeV).

4.4 Summary and Conclusions

Cuts have been imposed on the UA1 electron trigger events to enhance the electron signal with respect to background processes. The dominant source of background is the fluctuation in charged particle multiplicity of a jet to a single charged hadron which may be accompanied by neutral particles. After applying the cuts 205 electron candidates remain, and the predicted contribution from mis-identified pion overlaps has been assessed at 8.3±1.3 events. An additional source of background from the unseen conversion of high-P_t photons to electron-positron pairs has also been assessed at 2.8±0.9 events.

5. THE ANALYSIS

5.1 Introduction

The ability to identify leptons and to measure their energy is a powerful tool in the study of $p\bar{p}$ interactions, for in principle each lepton production channel has a unique signature which can be characterised by one or more kinematical variables. Two isolated leptons of opposite sign is in general a flag for the Drell-Yan mechanism, and for J/ψ, Υ and Z^0 production. These processes are easily distinguished by the invariant mass of the lepton pair: the Z^0, J/ψ and Υ have clearly separated peaks superimposed above a Drell-Yan continuum. Equally clear in their signature are leptonic decays of the $W^\pm$ which are characterised by a high transverse momentum isolated lepton accompanied by missing transverse energy (with $|E_t^{miss}| \sim |P_t^{lepton}|$). Heavy flavour (c,b) production has been investigated by UA1 [29] by using non-isolated high-P_t muons as a flag for the semileptonic decays of heavy flavours. More than one non-isolated lepton is a tag for the double semileptonic decays of heavy flavours, and a measurement of the ratio of the number of like-sign to unlike-sign non-isolated muon pairs in UA1 [30] has suggested the possibility of $B^0\bar{B}^0$ mixing. Another possible channel for lepton production is the semileptonic decay of the predicted top quark. The lepton is then expected to be isolated because of the high mass of the top quark, though the signature is rather complex and an extraction of a top quark signal from $p\bar{p}$ data is more difficult than for the other mechanisms described above.

The above lepton studies have been carried out by UA1 predominantly using data containing a muon candidate. Although the muon acceptance in the UA1 apparatus is relatively poor compared to the electron acceptance, muon candidates can be detected down to low values of transverse momentum (down to P_t~3 GeV/c). A muon can also be identified even if it is accompanied by a jet, because any associated hadronic activity is absorbed by the central hadron calorimeters before the muon drift chambers. In contrast, stringent cuts have to be applied on the P_t and the isolation of electron candidates in order to reduce the background from electron misidentification. The muon sample is therefore more suited to studies of Drell-Yan, J/ψ and Υ production (from which the two electrons or muons have low transverse momenta) and for heavy flavour production (in which, except from decays of the predicted top quark, the electron or muon is accompanied by a jet and is not isolated).

This chapter presents an inclusive analysis of the UA1 data which satisfies the electron selection criteria described in Chapter 4.

5.2 Monte Carlo Predictions

In this analysis the properties and rates of the data were compared with predictions from the ISAJET 5.23 Monte Carlo [31] which simulates $p\bar{p}$ interactions at high energy. It is therefore instructive to begin this chapter with a description of the ISAJET Monte Carlo and of the generated Monte Carlo event samples. ISAJET was used because a large amount of software had been developed by the UA1 collaboration to tune the phenomenological models incorporated by ISAJET to match the data.

5.2.1 The ISAJET Monte Carlo

5.2.1.1 QCD Subprocesses

The first step in the event generation is to generate a primary hard scatter with the appropriate QCD cross-section, which has the general form:

$$\sigma = \sigma_0 \times F(x_1,Q^2) \times F(x_2,Q^2)$$

where

σ_0 is the cross-section of the scatter described by perturbative QCD. For Drell-Yan processes, the cross-section is calculated according to the Standard Model. For 2→2 scattering, the $O(\alpha^2)$ calculations of Combridge et al [14] are used.

$F(x,Q^2)$ is the structure function corrected for QCD scaling violations as calculated by Eichten et al [32] where x_1 and x_2 are the fraction of the proton momentum carried by partons 1 and 2, and Q^2 is the energy transfer scale. The definitions of Q^2 are shown in Figure 44.

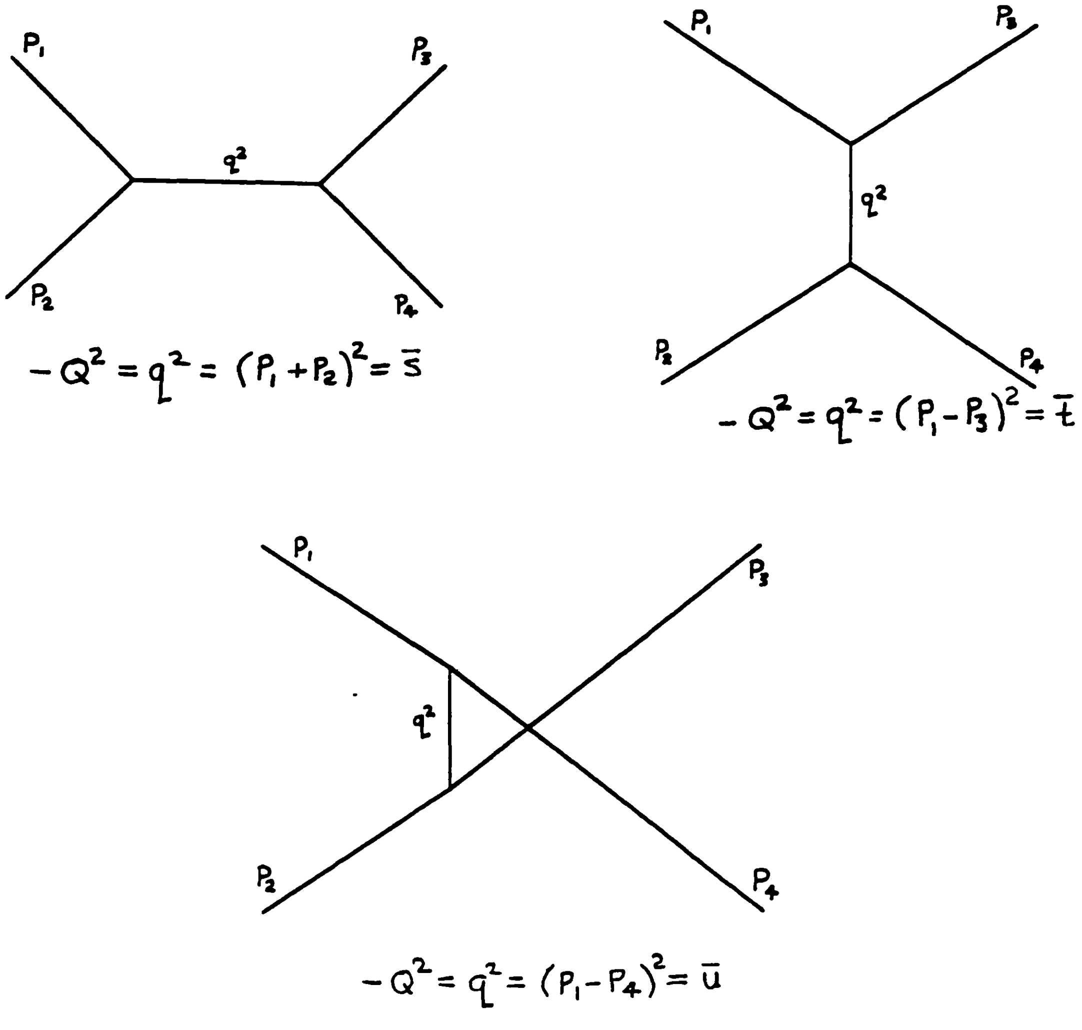

Figure 44: Definitions of Q^2

ISAJET defines Q^2 as the following convolution of the $\bar{s}$, $\bar{t}$ and $\bar{u}$ Mandelstam variables:

$$Q^2 = \frac{2\bar{s}\,\bar{t}\,\bar{u}}{\bar{s}^2 + \bar{t}^2 + \bar{u}^2}$$

5.2.1.2 Gluon Bremsstrahlung

ISAJET incorporates initial and final state gluon bremsstrahlung to allow for the possibility of more than two jets in the final state. Partons with a high virtual mass are evolved using the leading log approximation of Fox & Wolfram [33], but the cascade is terminated if the virtual mass of the parton is decreased to $m_p + 6$ GeV/c^2, where m_p is the rest mass of the parton (assumed in ISAJET to be zero for all flavours except b and t). The cut at 6 GeV/c^2 is necessary to avoid the infrared and collinear singularities discussed in Section 2.4.3, and the physics at the lower energy scale is assumed to be incorporated into the model for hadronisation. The jet multiplicity predicted using this model is in good agreement with jet data taken at SPS collider energies [34].

5.2.1.3 Jet Fragmentation

After their QCD evolution, final state quarks and gluons are on mass shell and are subsequently hadronised using the Independent Fragmentation model of Field and Feynman [15], discussed in Section 2.4.2. Mesons are produced with a mean transverse momentum of $<p_t> = .35$ GeV/c relative to the parent parton. Diquarks are generated in the cascade to account for baryon production in the jet. In order to preserve colour and flavour, a gluon is emitted at the end of the cascade as a light quark or antiquark. The fragmentation of heavy flavours (c,b) is tuned to match the parameterisation of Peterson et al [16].

5.2.1.4 The Spectator System

The spectator quarks (the remaining quarks in the proton and antiproton beams) are hadronized to produce particle multiplicity and transverse energy distributions similar in shape to those observed in minimum-bias events (events satisfying a $p\bar{p}$ interaction trigger only, without a hard scatter). The global multiplicity distribution is tuned to reproduce the multiplicity plateau in events containing high-E_t jets in the region of pseudorapidity-phi (η,ϕ) space far from the jet axis [34]. The mean transverse energy of prompt mesons is tuned using the same data. The transverse energy of electron candidates can be considered as being superimposed above the transverse energy plateau that arises from the spectator system (and a smaller contribution from soft initial state gluon bremsstrahlung), so the spectator system is important when defining the isolation of the electron candidates. Predictions using ISAJET are in good agreement [29] with the observed level of the transverse energy plateau in events containing a muon candidate and a jet, in the region of (η,ϕ) space surrounding the muon candidate. The level of the transverse energy plateau is typically about 4 GeV in the range $\Delta\eta = 1, \Delta\phi = \pi$.

5.2.2 Generation of the Monte Carlo Event Samples

A Monte Carlo generation was performed [35] for each of the physics processes that were expected to contribute to the electron data sample. Four distinct types of physics processes were generated:

1. Intermediate vector boson ($W^{\pm}, Z^0$) production with decays to all possible channels except top (Figure 17);

2. QCD production of heavy flavours ($b\bar{b}, c\bar{c}$), produced either directly by a QCD $2 \rightarrow 2$ scattering process (Figure 19) or via gluon splitting during the QCD evolution of the partons outgoing from the hard scattering process (Figure 14);

3. Top quark production[3] via either the QCD production of $t\bar{t}$ pairs, the decay of the W to $t\bar{b}$ or the decay of the Z to $t\bar{t}$. Generations were performed for top masses of 25,30,40 and 50 GeV/c^2 (except the $Z^0 \rightarrow t\bar{t}$ generations which only used top masses of 25,30 and 40 GeV/c^2);

---

[3] Hereafter any reference to $W \rightarrow t\bar{b}$ is intended to refer to both the $W^+ \rightarrow t\bar{b}$ and $W^- \rightarrow b\bar{t}$ channels

4. Drell-Yan, J/ψ and Υ production (Figures 15 and 16).

Luminosities of approximately 10pb^{-1} were generated for each process, which corresponds to a sensitivity of about ten times that of the UA1 data. The generated events were then reconstructed through a complete simulation of the UA1 detector (including a simulation of the finite resolutions of energy and drift-time measurements) so that the ISAJET events can be selected and analysed with the same software routines as the real data. To avoid wasting CPU time, only the ISAJET events which contained an electron with $P_t^e > 8$ GeV/c were reconstructed. The electron selection described in Chapter 3 was then imposed by passing the fully reconstructed events through the same selection routine as the UA1 data. A prediction of the number of events from each process that can be expected in the real data sample could then be calculated and is given by

$$N = N^{tot} \times (\mathscr{L}^{UA1}/\mathscr{L}^{mc})$$

where N^{tot} is the number of Monte Carlo events that pass the electron selection

$\mathscr{L}^{UA1}$ is the integrated luminosity of the UA1 electron data sample (= 690nb^{-1})

$\mathscr{L}^{mc}$ is the integrated luminosity represented by the Monte Carlo sample:

$$\mathscr{L}^{mc} = N_{gen} / \sigma.B$$

where N_{gen} is the total number of Monte Carlo events generated,

σ is the inclusive cross-section for the particular physics process,

B is the relevant branching ratio.

Therefore the cross-section for each of the electron production channels must be known in order to estimate the contribution from that channel.

5.2.3 Monte Carlo Cross-Sections

In this analysis, the cross-sections predicted by ISAJET were normalised whenever possible to measurements of real data. The ISAJET cross-sections for $W^\pm$ and Z^0 production were normalised to the values of $\sigma(W^\pm \rightarrow e^\pm \nu)$ and $\sigma(Z^0 \rightarrow e^+e^-)$ measured [36] by the UA1 Collaboration. Cross-sections for top quark production in the $W \rightarrow t\bar{b}$ channel were also normalised to measured values of $\sigma(W^\pm \rightarrow e\nu)$. ISAJET calculates cross-sections for QCD heavy flavour production only to $O(\alpha_S^2)$. However the contributions from gluon splitting in $O(\alpha_S^3)$ diagrams (Figure 14) can be substantial, especially for charm production when the virtuality of the gluon is not too large. Therefore the cross-sections for QCD $c\bar{c}$,$b\bar{b}$ and $t\bar{t}$ production were taken from the EUROJET Monte Carlo [38] which uses perturbative QCD cross-sections up to $O(\alpha_S^3)$, though the QCD $b\bar{b}$,$c\bar{c}$ event rate was also normalised to UA1 data using events containing a non-isolated muon and a jet [29]. The cross-sections used in this analysis for $W^\pm$, Z^0 and top quark production are summarised in Table 9 [37].

Table 9: Cross-sections for W/Z and top quark production

Process	Cross-section (nb)
$W^\pm \rightarrow$ all (except top)	5.08
$Z^0 \rightarrow$ all (except top)	1.94
QCD $t\bar{t}$, $m_{top} = 25$ GeV/c^2	12.8
QCD $t\bar{t}$, $m_{top} = 30$ GeV/c^2	5.1
QCD $t\bar{t}$, $m_{top} = 40$ GeV/c^2	1.1
QCD $t\bar{t}$, $m_{top} = 50$ GeV/c^2	0.3
$W \rightarrow t\bar{b}$, $m_{top} = 25$ GeV/c^2	1.63
$W \rightarrow t\bar{b}$, $m_{top} = 30$ GeV/c^2	1.55
$W \rightarrow t\bar{b}$, $m_{top} = 40$ GeV/c^2	1.30
$W \rightarrow t\bar{b}$, $m_{top} = 50$ GeV/c^2	1.00

The cross-section given by ISAJET for the Drell-Yan process was found to be in good in agreement with the value measured by UA1 [30] using dimuon data. ISAJET has no J/ψ or ϒ generator, so for these productions the Drell-Yan process was generated with a cut on the mass of the virtual photon of $2.9 < M_\gamma < 3.3$ GeV/c^2 and $9 < M_\gamma < 10$ GeV/c^2 respectively. Cross-sections for the J/ψ and ϒ productions were normalised to the values measured by UA1 [30] using dimuon events.

5.2.4 Contributions to the Electron Data Sample

There are 205 events in the UA1 data that satisfy the electron selection described in Chapter 3. The predicted contributions to the data sample for various processes are listed in Table 10.

The first error in each entry is the statistical error from the Monte Carlo. The second is the systematic error, which is discussed below. Errors quoted for QCD $t\bar{t}$ contributions are statistical only.

The uncertainty on the measured cross-sections is ±7% for $W^\pm$ and Z^0 production, and ±30% for Drell-Yan, J/ψ and ϒ production. In the $W^\pm$, Z^0, Drell-Yan, J/ψ and ϒ events, the rate of events in the high-P_t tails from higher order QCD corrections were normalised to data. The uncertainty in the measured event rate in the high-P_t tails of Drell-Yan, J/ψ and ϒ events is ±50%. For $W \rightarrow t\bar{b}$ production, there are higher order QCD corrections of 10-20% with an error of ±30%, in addition to the uncertainty of the W cross-section of ±7% [39]. The overall uncertainty on the $W \rightarrow t\bar{b}$ cross-section is between ±10% (light top) and ±14% (heavy top). The systematic error on QCD $b\bar{b}/c\bar{c}$ production is ±25%, which arises from the uncertainty in the relative contributions of $b\bar{b}$ and $c\bar{c}$. Finally, QCD $t\bar{t}$ production is the only process in which the cross-section cannot be normalised to measured data. The cross-section for QCD $t\bar{t}$ production therefore has a systematic error of ±15% which arises from the uncertainty on the integrated luminosity recorded by UA1.

Table 10: Contributions to the data sample

Process	Number of events in this data sample
$W \to$ all (except top)	136.3 ±2.9 ±8.7
$Z \to$ all (except top)	26.9 ±1.3 ±1.7
Drell-Yan	8.5 ±0.7 ±2.6
Υ	0.9 ±0.2 ±0.5
J/ψ	3.6 ±0.5 ±1.8
QCD $b\bar{b}/c\bar{c}$	5.6 ±0.7 ±1.4
$t\bar{t}$, $m_{top} = 25$ GeV/c^2	23.1 ±1.2
$t\bar{t}$, $m_{top} = 30$ GeV/c^2	16.4 ±1.0
$t\bar{t}$, $m_{top} = 40$ GeV/c^2	7.1 ±0.6
$t\bar{t}$, $m_{top} = 50$ GeV/c^2	3.3 ±0.4
$W \to t\bar{b}$, $m_{top} = 25$ GeV/c^2	3.3 ±0.4 ±0.3
$W \to t\bar{b}$, $m_{top} = 30$ GeV/c^2	5.6 ±0.7 ±0.6
$W \to t\bar{b}$, $m_{top} = 40$ GeV/c^2	6.6 ±0.7 ±0.7
$W \to t\bar{b}$, $m_{top} = 50$ GeV/c^2	6.9 ±0.9 ±0.8
Background ($\pi^\pm + n\pi^0$)	8.3 ±0.5 ±1.2
Background (conversions)	2.8 ±0.9
TOTAL (Monte Carlo and background, no top)	192.9 ±3.5 ±9.5
DATA	205

The sum of contributions from each process is in good agreement with the number of electron data events, without the need to include contributions from the top quark. From Table 10 it is clear that the data sample is dominated by decays of the $W^\pm$, and to a lesser extent by decays of the Z^0. The next largest contribution is expected from the overlap background, and all the non-IVB physics processes contribute a relatively small number of events. On the other hand, the number of events from top quark production (from QCD $t\bar{t}$ production and $W \to t\bar{b}$ decays) is substantial for small values of the top quark mass. The contribution from $Z^0 \to t\bar{t}$ is negligible and will not be discussed further.

5.3 A First Look at the Inclusive Data

5.3.1 Lepton Kinematics

Although the data sample seems at first glance to be overwhelmed by decays of the W and Z, these events can usually be easily identified due to their unique kinematics, specifically with the missing transverse energy and the electron transverse energy.

The presence of a high-P_t neutrino in the UA1 detector can be inferred by constructing E_t^{miss}, the vector sum of transverse energies over all calorimeter cells. With each calorimeter cell, we can define an energy vector

$$\vec{E}_i = \vec{n}_i E_i$$

where E_i is the energy in the i^{th} cell, and $\vec{n}_i$ is the unit vector pointing from the beam crossing point to the centre of the i^{th} cell. Without any non-interacting particles and for a perfect detector, E_t^{miss}, the vector sum of the components of $\vec{E}_i$ in the plane transverse to the beam axis of all calorimeter cells must be zero. A high-P_t neutrino from a $W \rightarrow e\nu$ decay passes undetected through the UA1 apparatus, so the imbalance created by the large deposition of energy in the calorimeters from the electron gives rise to a missing transverse energy vector which points along the path of the neutrino.

In general, E_t^{miss} is non-zero in the UA1 apparatus due to mis-measurements which arise from the finite resolution of the calorimeters and from leakage through gaps in the calorimeters. In UA1 a measurement of the energy imbalance in either of the two components transverse to the beam direction results in a gaussian distribution centred on zero. The width of this gaussian has been measured to be

$$\sigma(\Delta E_{y,z}) = 0.4 \times \sqrt{\Sigma E_t}$$

for minimum-bias events (requiring a beam crossing trigger only), and

$$\sigma(\Delta E_{y,z}) = 0.7 \times \sqrt{\Sigma E_t}$$

for events containing jets, in which E_t^{miss} becomes more sensitive to the finite energy resolution of the calorimeters.

Figure 45 and Figure 46 show plots of the missing transverse energy (E_t^{miss}) and the electron transverse energy (E_t^e) respectively for the inclusive data sample and for Monte Carlo predictions.

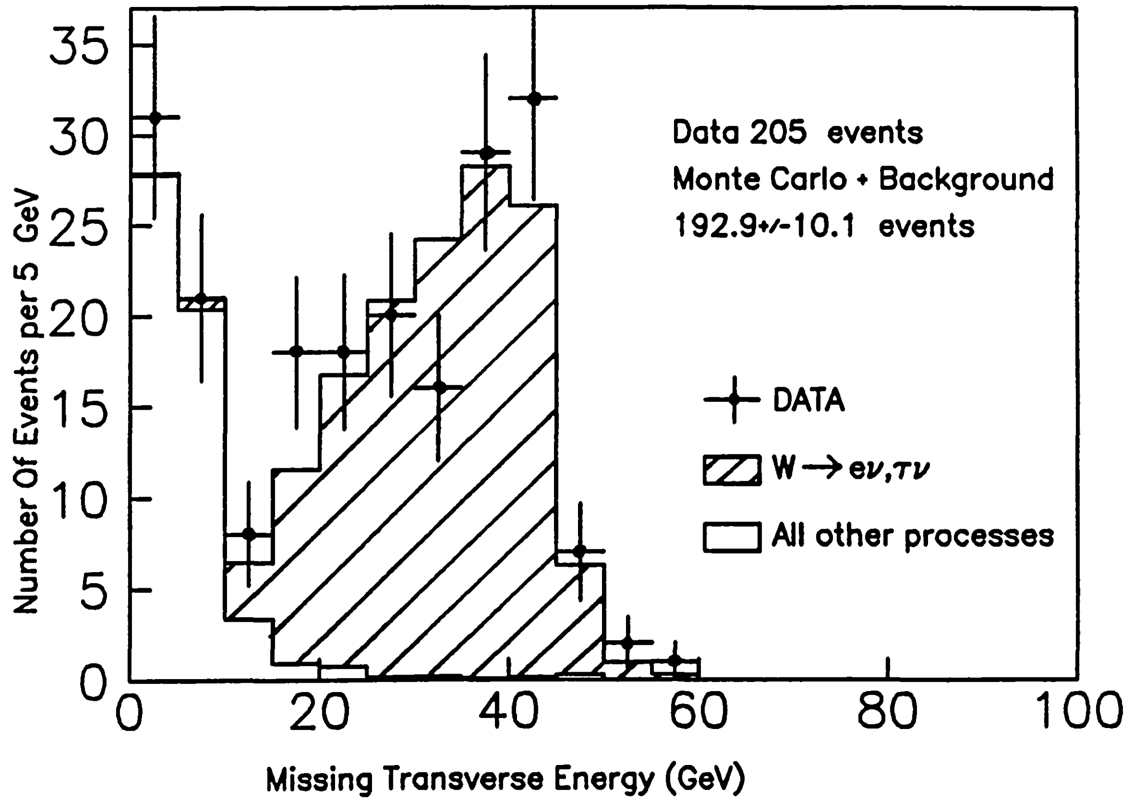

Figure 45: E_t^{miss} *distribution for the inclusive data*

The missing transverse momentum has a peak at $E_t^{miss} \simeq 40$ GeV which is associated with the Jacobian peak expected of W production and its 2-body decay to electron and neutrino. The predicted contribution from W production is shaded. The peak at low values of E_t^{miss} is due to the finite resolution of the UA1 calorimetry and therefore attributed to all other physics processes and background mechanisms because they do not

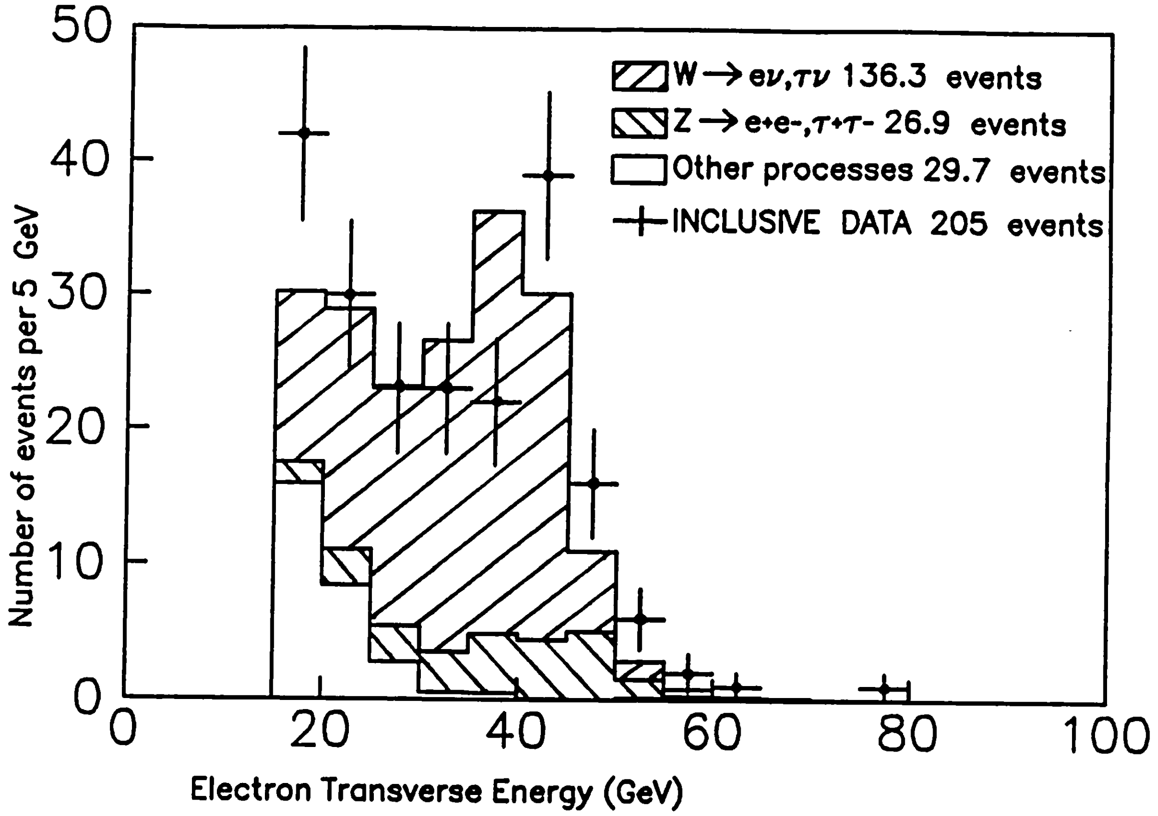

Figure 46: E_t^e distribution for the inclusive data

contain a neutrino of significant momentum. The Jacobian peak is also evident in the electron transverse energy, though the peak is degraded by the presence of high transverse energy electrons from Z^0 decays. Combining the previous two figures to form a plot of electron transverse energy against missing transverse energy (Figure 47) shows that the inclusive data forms three distinct regions.

There is a strong correlation between E_t^e and E_t^{miss} at high missing transverse energy (from $E_t^{miss} \geq 15$ GeV), which is characteristic of leptonic W decays. There is a region in which the electron has a high transverse energy but there is no significant missing en-

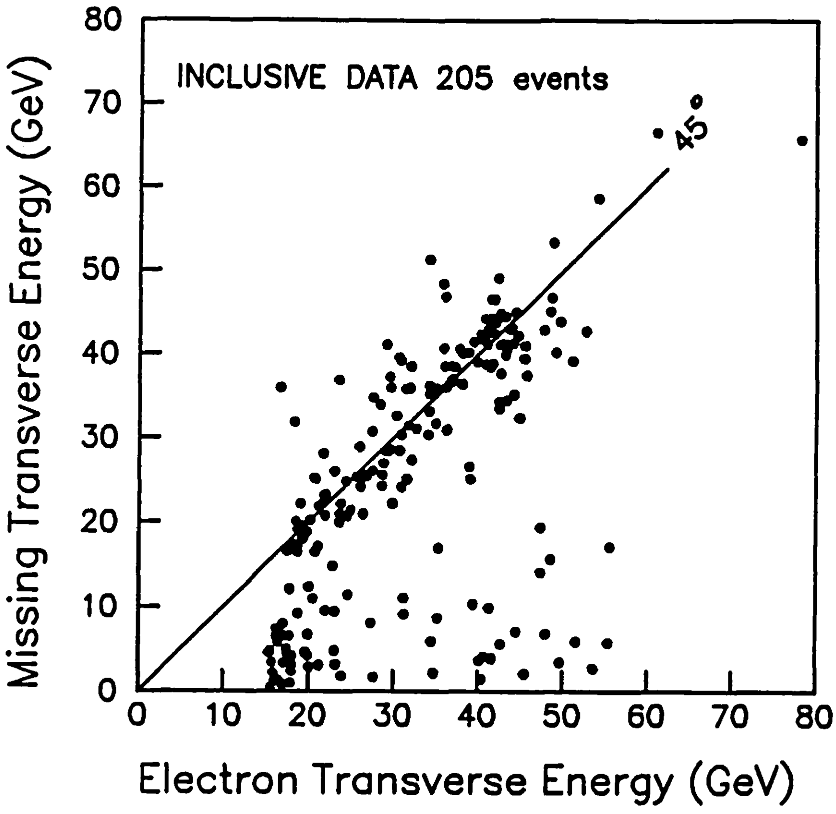

Figure 47: E_t^e *vs.* E_t^{miss} *for the inclusive data*

ergy, which is characteristic of leptonic Z^0 decays. Finally, there is a region of low E_t^e and low E_t^{miss} which are attributed to the background and all non-IVB physics processes.

5.3.2 Jets

The transverse energy and direction of jets can yield information about the p$\bar{p}$ interaction at the parton level. Jets in UA1 are defined as clusters of transverse energy in pseudorapidity-azimuth (η,ϕ) space. UA1 uses a very simple jet-finding algorithm [40] in which all the calorimeter cells are considered in descending order of E_t. The cell with the largest E_t acts as the initiator of a jet if it has $E_t > 2.5$ GeV, and if another cell is close to the jet in (η,ϕ) space ($\triangle R < 1.0$ where $\Delta R = \sqrt{(\Delta\eta^2 + \Delta\phi^2)}$ with ϕ in radians) then the energy vector corresponding to that cell is added vectorially with that jet. Otherwise, if the cell has $E_t > 2.5$ GeV, the cell acts as the initiator of a new jet. The cut at $\triangle R < 1.$ is justified by Figure 48 [41] which shows the transverse energy, transverse momentum, and charged particle multiplicity profiles as a function of pseudorapidity from the centre of the jet for 3 bins of jet E_t.

The jet is characterised by a peak in transverse energy below $|\eta| < 1$, superimposed above the flat profile of the spectator system, and the width of the jet in pseudorapidity is independent of the jet transverse energy.

The jet finding algorithm would consider the electromagnetic shower from an electron as a jet, so in this analysis the calorimeter cells associated with the electron shower are flagged and ignored by the jet finding algorithm.

Figure 49 shows the transverse energy of the highest-E_t jet in the event for the inclusive electron data. The distribution is dominated by a peak for low values of jet E_t ($E_t^{jet} < 10$ GeV) but scanning these events on the MEGATEK reveals that it is not clear at low energies whether jets found by the algorithm are valid or merely weak correlations in randomn depositions of energy. It is clear that as the transverse energy of a jet decreases, some validation becomes necessary to ensure that the jet arises directly from the fragmentation of a parton rather than from fluctuations in the transverse energy distribution of the spectator system.

In this analysis, the following procedure was adopted as a convention for jet counting:

1. The event is considered to contain at least one jet if the highest E_t jet found by the jet algorithm has a transverse energy greater than 12 GeV ($E_t^{j1} > 12$ GeV). Monte Carlo studies [42] suggest that the probability of such a jet originating from the fragmentation of a single parton is $> 85\%$;

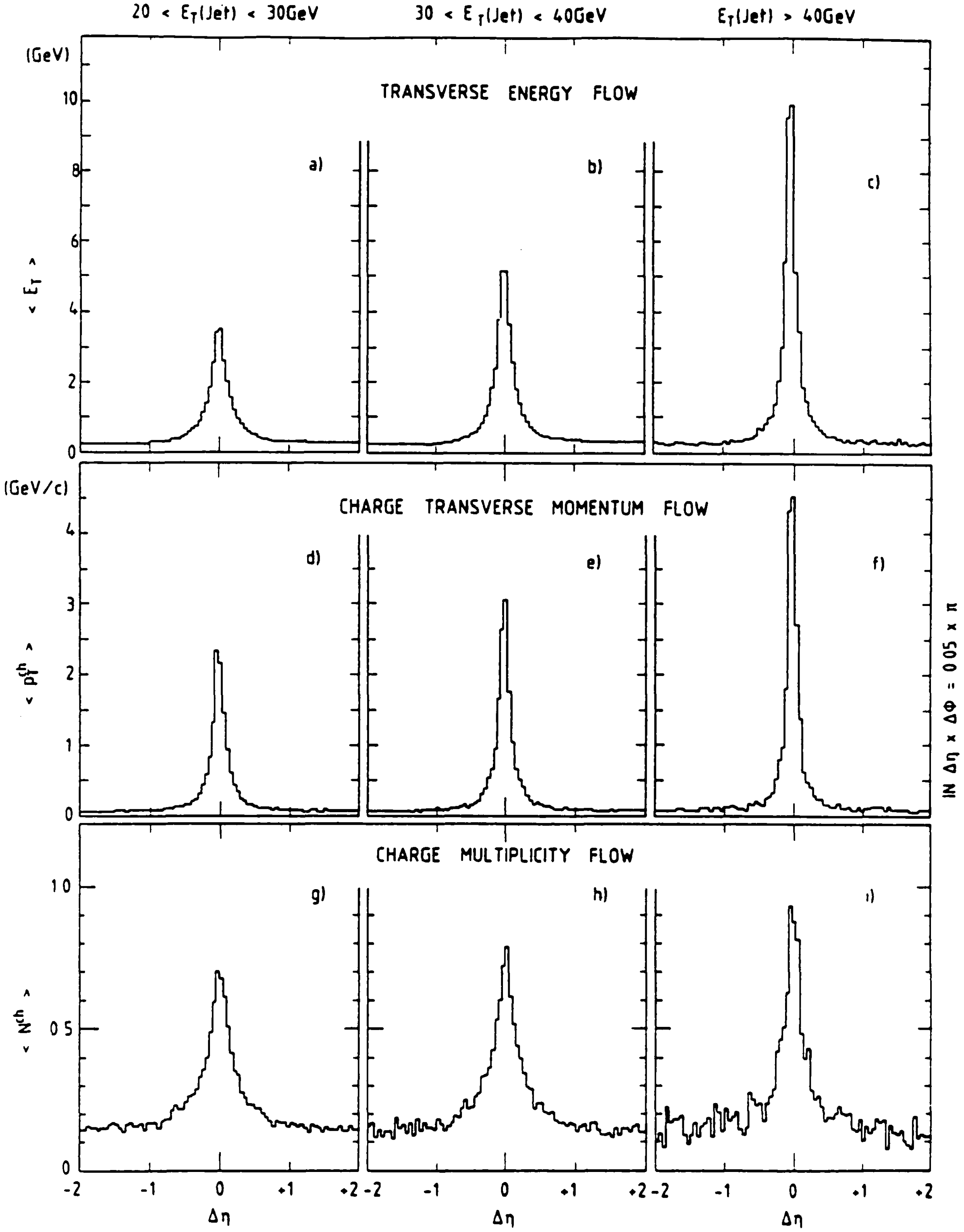

Figure 48: Jet profiles in the UA1 detector

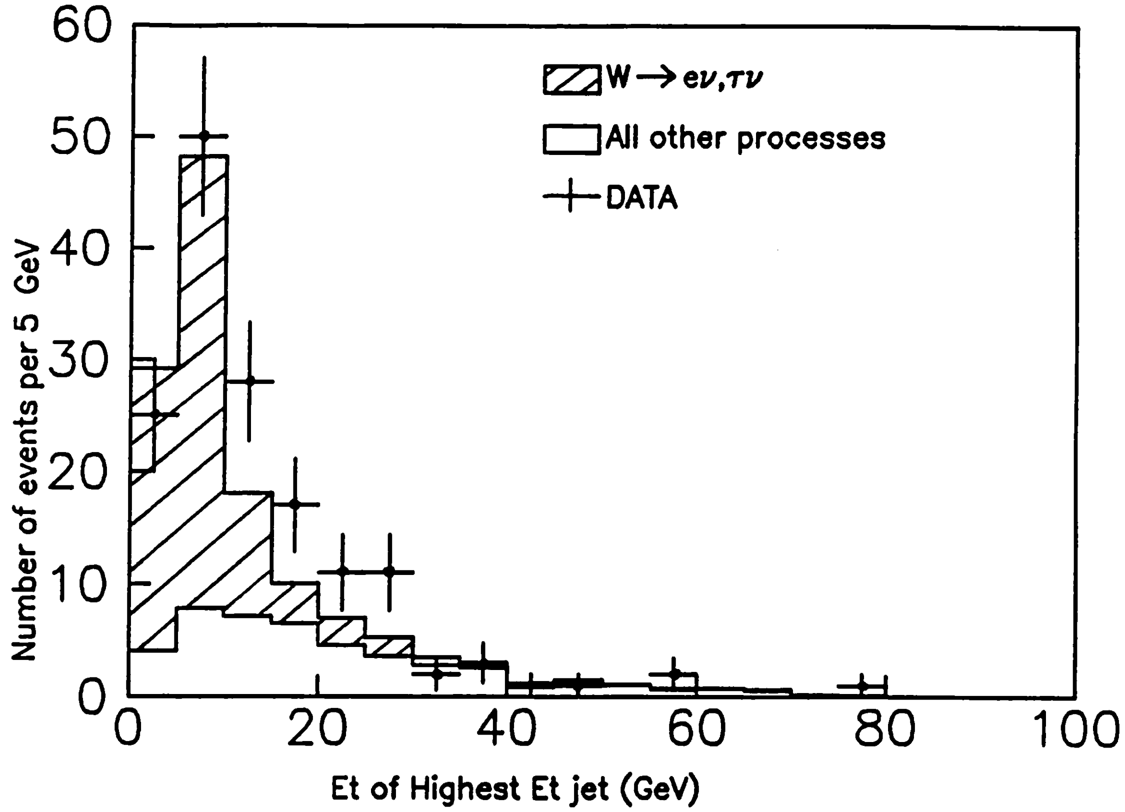

Figure 49: Transverse Energy of the highest-E_t jet

2. The lower E_t jets are only counted if they have a transverse energy greater than 7 GeV and have at least one track in the central detector with $P_t^{CD} > 0.5\mathrm{GeV/c}$ within $\Delta R < 0.4$ (where ΔR is the distance between the track and the jet axis in (η,ϕ) space, defined as $\Delta R = \sqrt{(\delta\eta^2 + \delta\phi^2)}$). Monte Carlo studies suggest the probability of such jets arising from the fragmentation of a single parton is >70%.

It is difficult to reconstruct jets that are very close to the beam axis, so jets are only counted if they are within the rapidity range $|\eta| < 2.5$, which covers the central part of the UA1 apparatus (the gondolas, bouchons, C's and I's). Table 11 shows the number of jets (defined by the validations listed above) in each event for the inclusive electron data and for Monte Carlo predictions of individual processes.

Table 11: Number of jets per event in the electron data sample

Process	$N_{jet}=0$	$N_{jet}=1$	$N_{jet}\geq 2$
$W\rightarrow$ all	125.6±8.5	9.4±1.0	1.3±0.3
$Z\rightarrow$ all	18.4±1.6	6.6±0.8	1.9±0.4
$DY+J/\psi+\Upsilon$	6.1±1.8	5.7±2.9	1.2±0.7
QCD $b\bar{b}/c\bar{c}$	1.8±0.6	1.4±0.5	2.4±0.8
Background	3.0±0.7	5.5±1.3	2.6±0.6
TOTAL	154.9±8.9	28.6±3.5	9.4±1.3
DATA	154	38	13

Most of the inclusive data events do not contain a jet: this subsample of events is clearly dominated by the lowest order Drell-Yan diagrams for $W^{\pm}$ and Z^0 production (Figure 17). Events with one or more jets have roughly equal contributions from each of the processes. Clearly jet counting alone is not sufficient to distinguish different processes.

5.3.3 Summary

There are few general features to the inclusive data sample that help to discriminate the non-IVB processes, and Monte Carlo predictions and the distinctive features of the E_t^e and E_t^{miss} distributions in the electron data suggest that the inclusive data sample is dominated by decays of the $W^{\pm}$ and Z^0 IVBs. It is therefore instructive to attempt to remove the $W^{\pm}$ and Z^0 events from the inclusive data sample before attempting a more detailed study of event topologies.

5.4 Dielectron Events

The physics processes that can give rise to events containing two electrons in the inclusive electron sample are the leptonic decay of the Z^0, the Drell-Yan process, J/ψ or Υ production, and two semileptonic decays from heavy flavours. The predicted background to the dielectron sample from electron misidentification is negligible, so the cuts applied to select the second electromagnetic cluster are less stringent than those for the primary electron. Table 12 summarises the cuts on the second electromagnetic cluster, and lists the Monte Carlo predictions of the efficiencies of these cuts on various physics processes.

The number of dielectron events in the inclusive data sample is in good agreement with predictions from the $Z^0 \rightarrow e^+e^-$ and Drell-Yan processes. All other processes contribute a negligible number of events. The 2-cluster mass for dielectron events in this data sample is shown in Figure 50, together with predictions for Z^0 decays and for the Drell-Yan mechanism.

5.4.1 $Z^0 \rightarrow e^+e^-$ *Contributions*

The dielectron mass distribution above 70 GeV/c^2 is well described by the $Z^0 \rightarrow e^+e^-$ process. The small low mass tail to the Z^0 dielectron mass distribution arises from the $Z^0 \rightarrow \tau^+\tau^-$ process followed by by $\tau \rightarrow e\nu\nu$ for both of the taus. The topology of $Z^0 \rightarrow e^+e^-$ events is that of two isolated electrons back-to-back in the plane transverse to the beam axis each carrying a large transverse momentum. A typical $Z^0 \rightarrow e^+e^-$ candidate is shown in Figure 51.

Figure 51(a) is a MEGATEK display in which the box depicts the outline of the central hadronic calorimeter, the inner cylinder depicts the Central Detector, and the outer cylin-

Table 12: Dielectron Event Selection

Variable	Cut
E_t (em cluster)	> 6 GeV
P_t (electron track)	> 5 GeV/c
Isolation:	
E_t ($\Delta R < 0.4$)	$< 15\%$ E_t(em cluster)
P_t ($\Delta R < 0.4$)	$< 15\%$ P_t(electron track)

Efficiency of dielectron selection

Process	Efficiency(%)	Number of events
$Z^0 \rightarrow$ all	79.4	20.5 ± 1.7
($Z^0 \rightarrow e^+e^-$)	(80.7)	(20.1 ± 1.7)
Drell-Yan	66.9	5.0 ± 1.8
J/ψ	2.9	0.1 ± 0.1
Υ	0.	0.
$W^\pm \rightarrow$ all	0.	0.
QCD $b\bar{b}/c\bar{c}$	1.8	0.1 ± 0.1
Background	0.	0.
TOTAL		25.7 ± 2.5
DATA		26

der depicts the gondola central electromagnetic calorimeters. Calorimeter cells which contain more than 1 GeV transverse energy are outlined. Hits in a gondola are represented by a rectangle; the width of the rectangle represents the physical width of a gondola, but the length represents the magnitude of the energy deposition. Central detector tracks which carry a transverse momentum greater than 1 GeV/c are also displayed. In Figure 55(a) two of the tracks point to depositions of energy in the gondolas, which correspond to the two electron candidates. Each electron deposits energy into two gondolas.

Figure 51(b) displays the orientation of the two electrons in the plane transverse to the beam axis (the circular display, clearly showing the back-to-back nature of the elec-

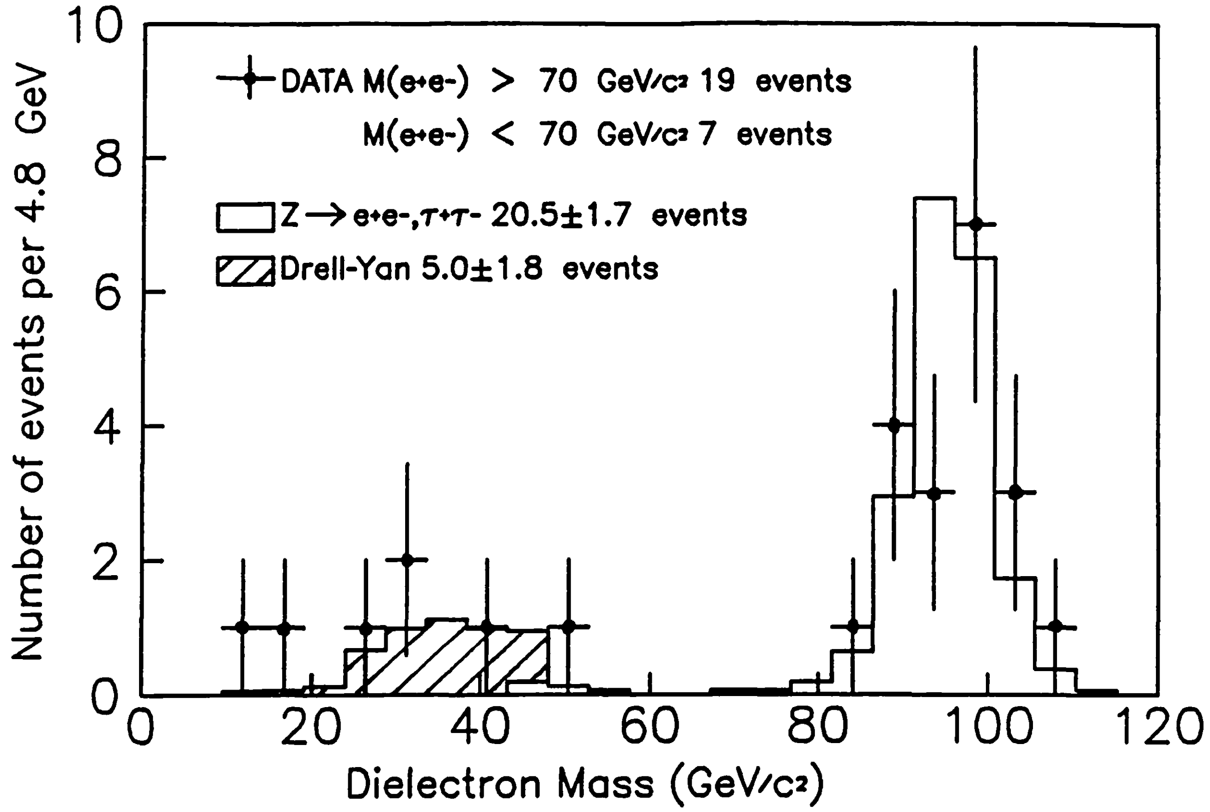

Figure 50: Dielectron mass distribution for the inclusive data

trons) and in pseudorapidity (the horizontal display). The length of each arrow represents the transverse energy, which can be calibrated against the grid intervals. Figure 51(b) also shows the direction and magnitude of the missing transverse energy vector, which is negligible in this event.

The Monte Carlo prediction of the efficiency of the dielectron selection for $Z^0 \rightarrow e^+e^-$ events is 80.7%, and 4.3±0.6 $Z^0 \rightarrow e^+e^-$ events remain after the selection. Of the remaining events, ~1 is expected in which one electron passes through the vertical gap between opposite pairs of gondolas. One such $Z^0 \rightarrow e^+e^-$ event is indeed found, and is shown in Figure 52.

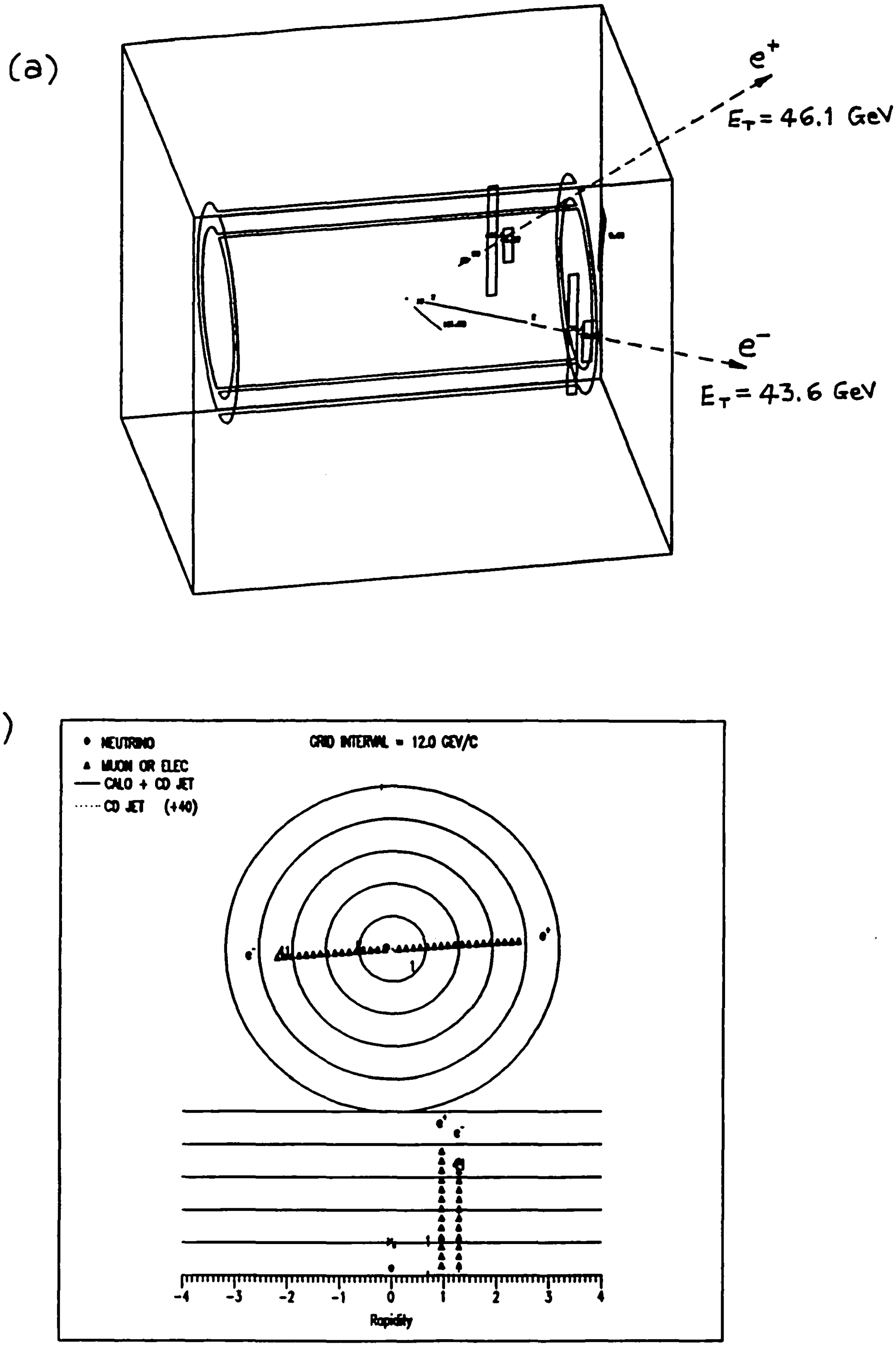

Figure 51: Run/event 15995/918. A $Z^0 \rightarrow e^+e^-$ candidate

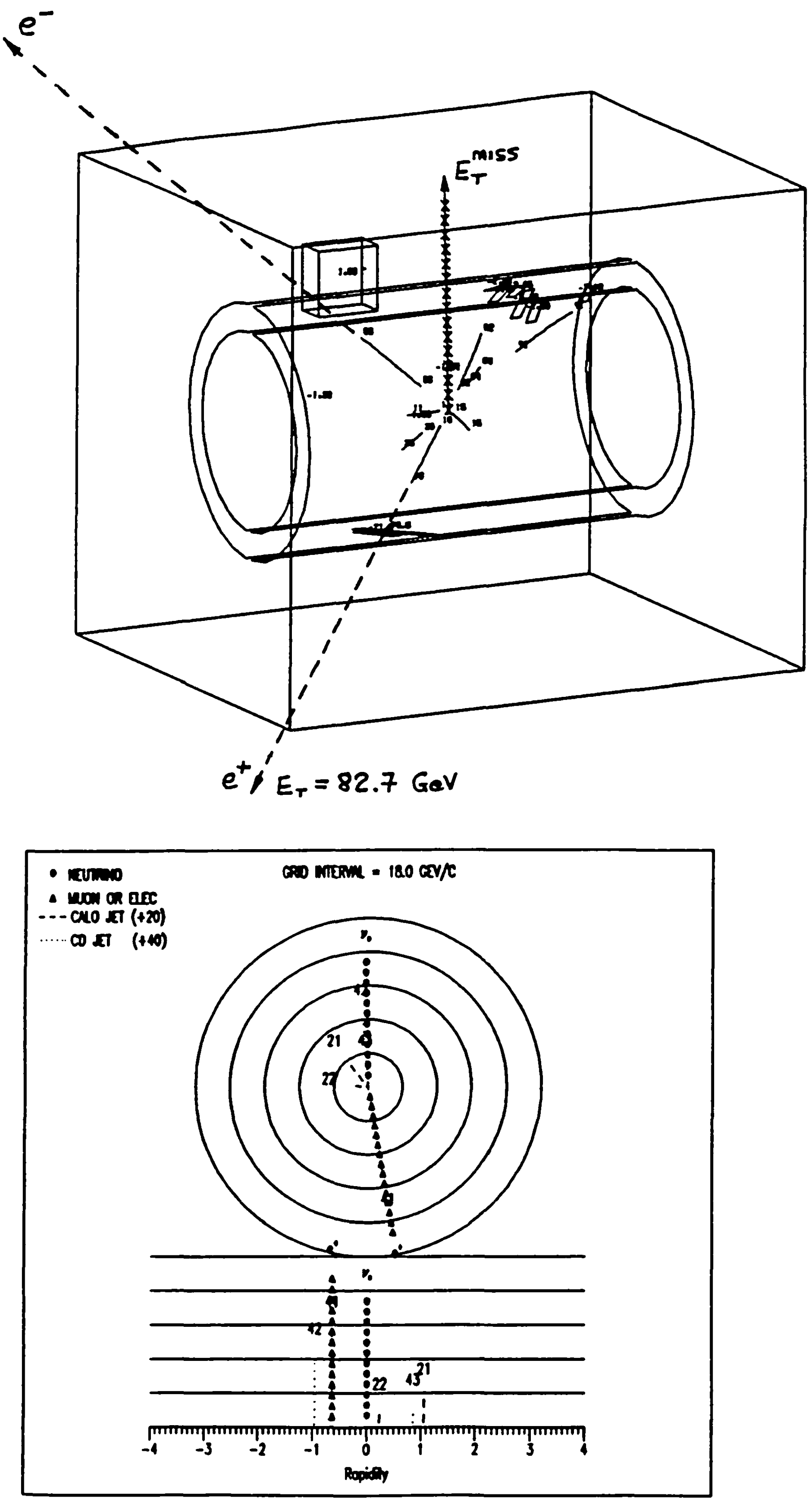

Figure 52: Run/event 13157/1186. A $Z^0 \rightarrow e^+e^-$ faking a $W^+ \rightarrow e^+\nu$

In run/event 13157/1186, the e^- passes undetected by the gondolas through the vertical gap. A vector sum of transverse energy in the calorimeters then gives rise to a large missing transverse energy vector, back-to-back with the e^+ in azimuth. The resulting topology is therefore of a $W^+ \to e^+ \nu$ candidate.

In the other $Z^0 \to e^+ e^-$ events that remain after the dielectron selection, the second electron is expected to either have some hadronic punchthrough or to be non-isolated. In both cases the apparent topology of the event is that of an electron back-to-back in azimuth with a hadronic jet. One such candidate in which the second electron has some hadronic punchthrough and is reconstructed as a jet is shown in Figure 53.

A full analysis of the $Z^0 \to e^+ e^-$ candidates from UA1 has been given elsewhere [36]. The $Z^0 \to e^+ e^-$ candidates in this thesis form only a subset of the full UA1 sample because the background to the $Z^0 \to e^+ e^-$ signal is small and UA1 uses a less stringent electron selection criteria.

5.4.2 Drell-Yan Contributions

The events containing two electron candidates with a 2-cluster mass less than 70 GeV/c^2 are well described by the lowest order Drell-Yan process of Figure 15. The topology of the dielectron Drell-Yan candidates is that of two electrons back-to-back in azimuth. One of the Drell-Yan candidates is shown in Figure 54. The dielectron selection is 66.9% efficient for Drell-Yan Monte Carlo events satisfying the electron selection criteria listed in Chapter 4.

This leaves 3.0± 1.6 Drell-Yan events which have only one visible electron. The topology of the one-electron Drell-Yan events is that of an electron back-to-back in azimuth with a jet, which is consistent with the higher order diagrams of Figure 16, in which a hard gluon bremsstrahlung imparts a large transverse momentum to the virtual photon. The photon either decays asymmetrically to produce a high-P_t electron accompanied by a soft electron invisible within the UA1 apparatus, or one of the electrons is invisible because it is contained within the jet.

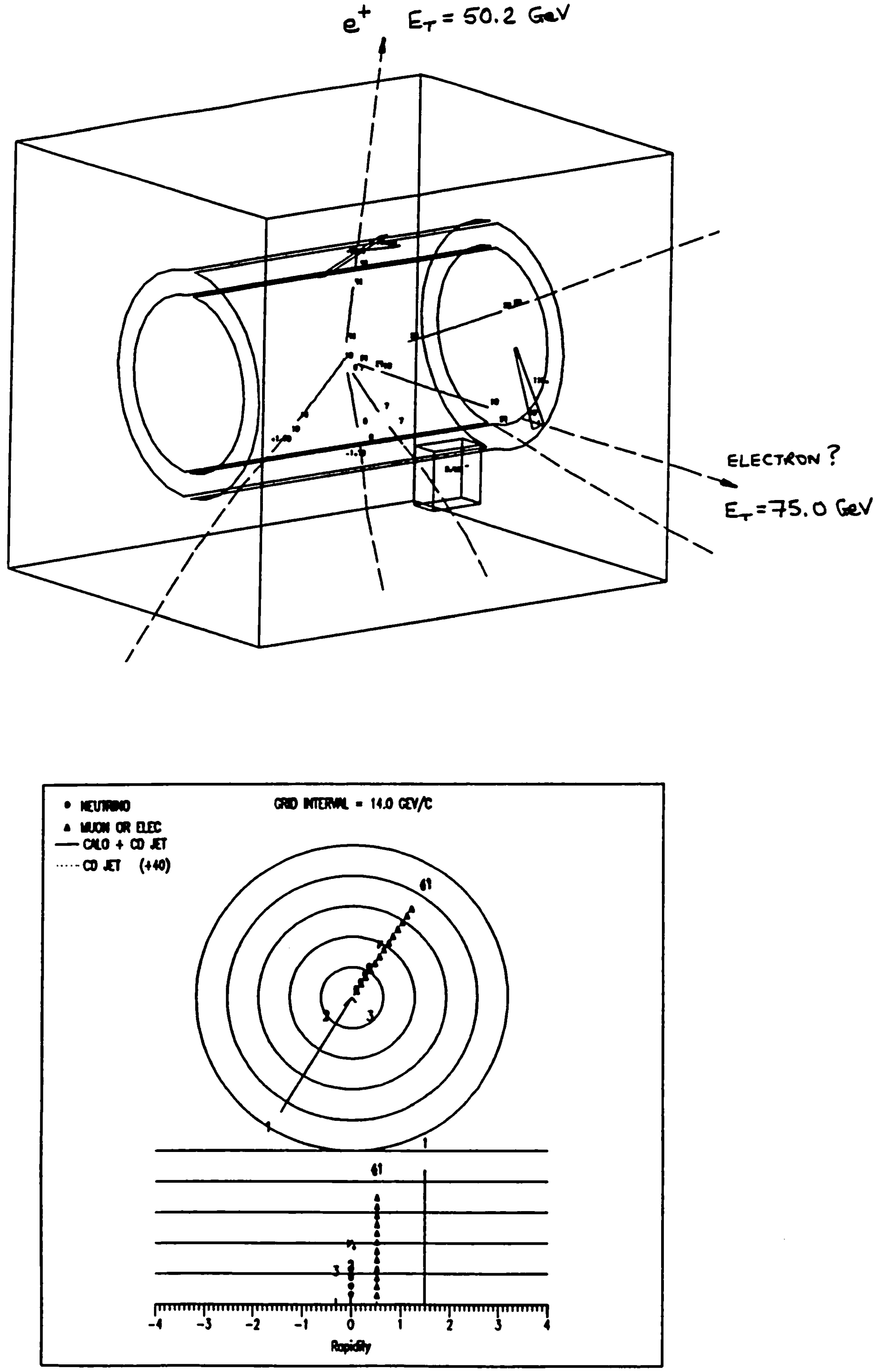

Figure 53: Run/event 15730/956. A 1-electron $Z^0 \rightarrow e^+e^-$ candidate

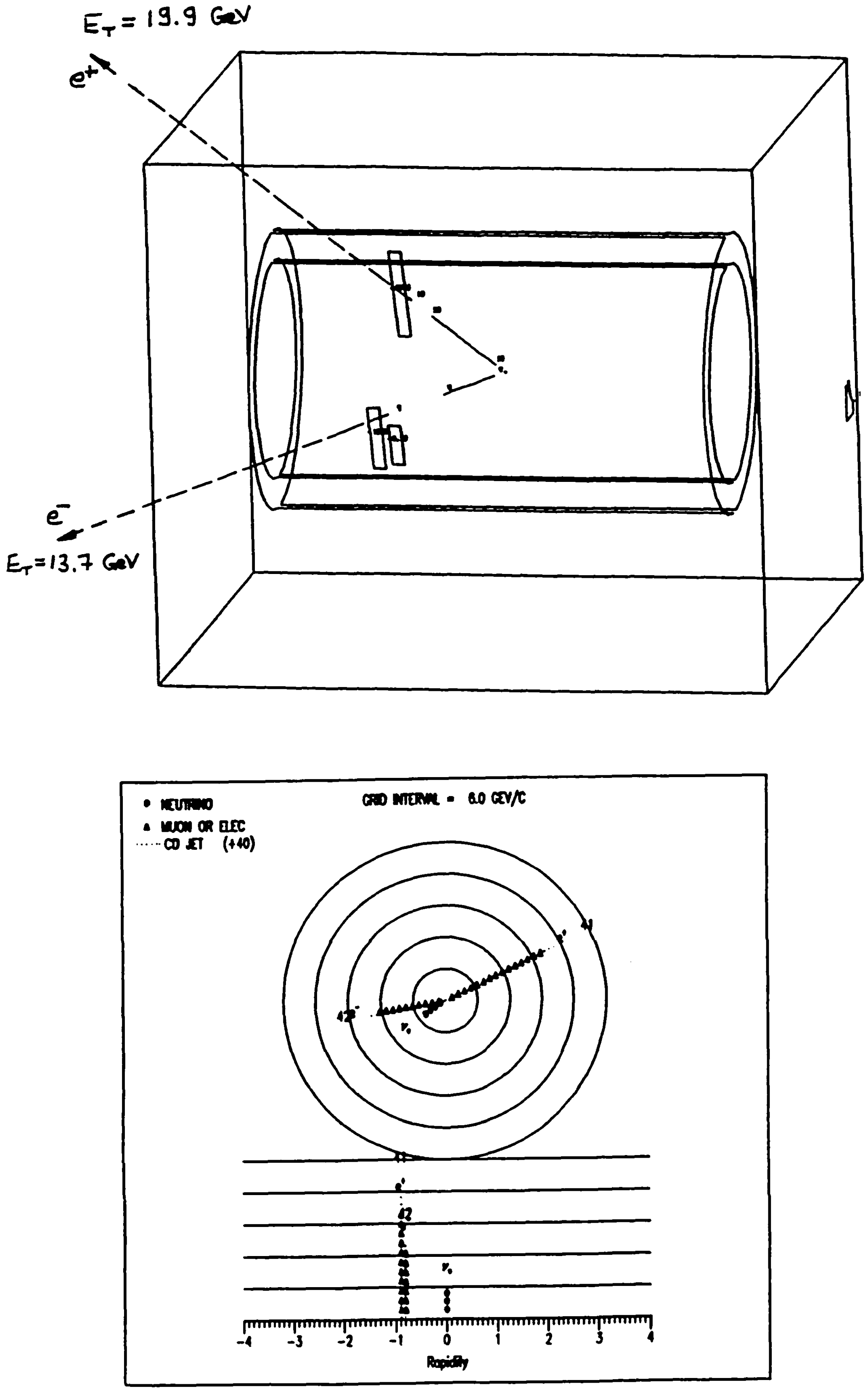

Figure 54: Run/event 7939/412. A Drell-Yan Candidate

5.5 Leptonic $W^{\pm}$ Decays

Production of the $W^{\pm}$ intermediate vector boson is expected to contribute to the data sample primarily through its decay to electrons ($W^{\pm} \rightarrow e^{\pm}\nu$), though a more limited contribution is also expected via $W^{\pm} \rightarrow \tau^{\pm}\nu_{\tau}$ followed by $\tau^{\pm} \rightarrow e^{\pm}\nu_{e}\nu_{\tau}$. The expected contributions from $W^{\pm} \rightarrow e^{\pm}\nu$ and $W^{\pm} \rightarrow \tau^{\pm}\nu$ are 128.7 and 7.6 events respectively. Such events are characterised by an isolated electron which carries a large momentum transverse to the beam direction. The neutrino(s) pass undetected through the UA1 detector, so the imbalance created by the large electromagnetic deposition of the electron gives rise to a missing transverse energy vector which is back-to-back with the electron in azimuth. A typical $W^{-} \rightarrow e^{-}\bar{\nu}$ candidate is shown in Figure 55.

Occasionally W candidates contain one or more jets which arise from the higher order QCD diagrams of Figure 16. Jets in W candidates are consistent with expectations of initial state gluon bremsstrahlung, namely that they tend to be emitted close to the beam axis. Figure 56 shows a typical W + 1jet candidate, in which the jet (represented by the solid line in Figure 56(b)) is produced at large rapidity.

A characteristic feature of W + jet candidates in this data sample is that there is no correlation between the jet and electron directions in azimuth, because the mass of the W is much greater than the transverse momentum imparted to it by gluon bremsstrahlung. This is best illustrated by figure 57 which shows a plot of $\Delta\phi$(e-jet1) (the difference in azimuthal angle between the electron and the highest E_t jet) against E_t^{miss} for the inclusive electron data. The events with $E_t^{miss} > 20$ GeV (which are predominantly $W \rightarrow e\nu$ candidates) show no clear correlation in $\Delta\phi$(e-jet1), but events that satisfy $E_t^{miss} < 20$ GeV (all other processes) are peaked towards 180^0 in $\Delta\phi$(e-jet1).

The invariant mass of the W cannot be calculated directly from the 4-vectors of the electron and neutrino because only the transverse component of the neutrino momentum is measured. However, decays of the W can be characterised by the transverse mass of the

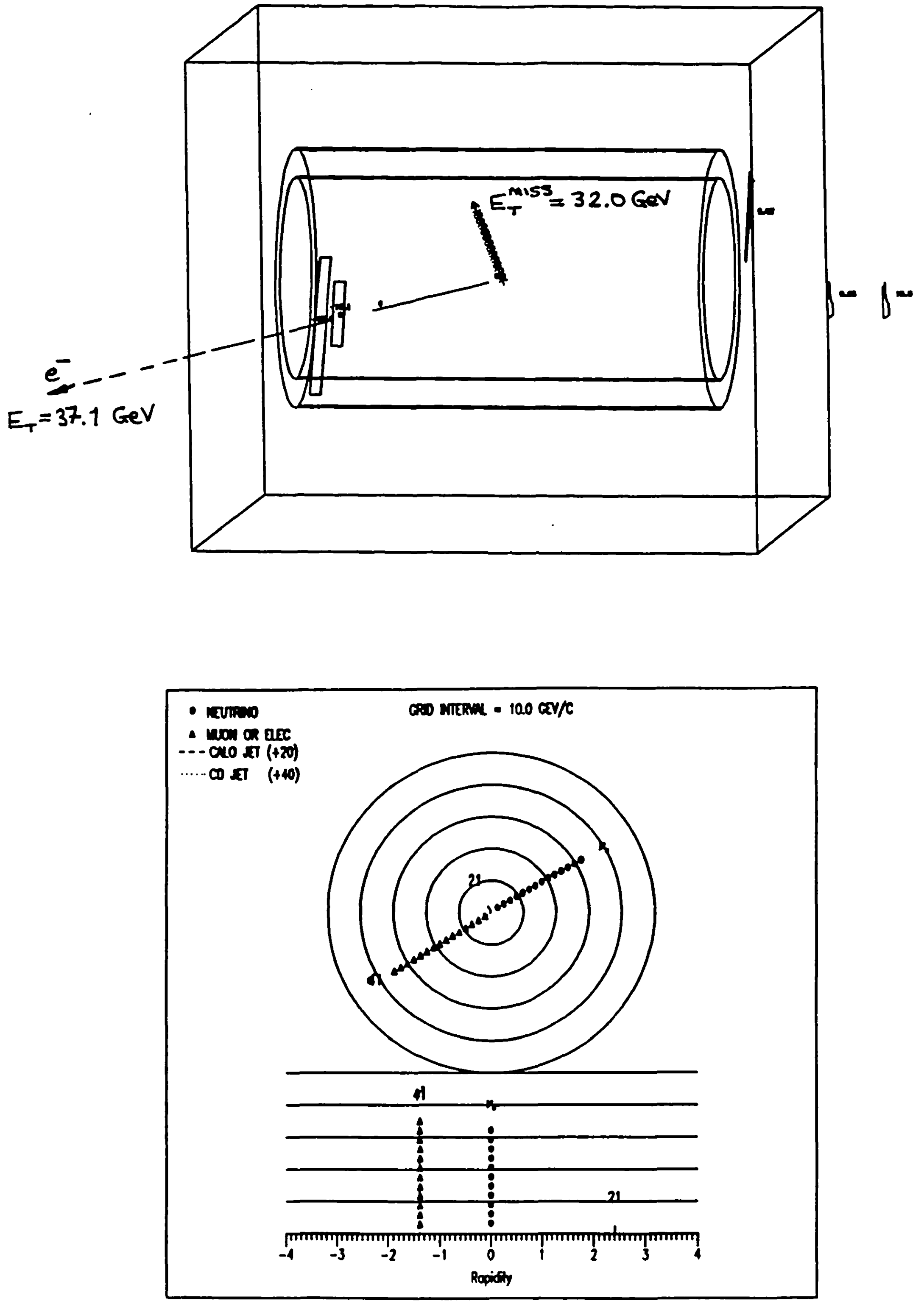

Figure 55: Run/event 12149/141. A $W^- \to e^- \bar{\nu}_e$ Candidate.

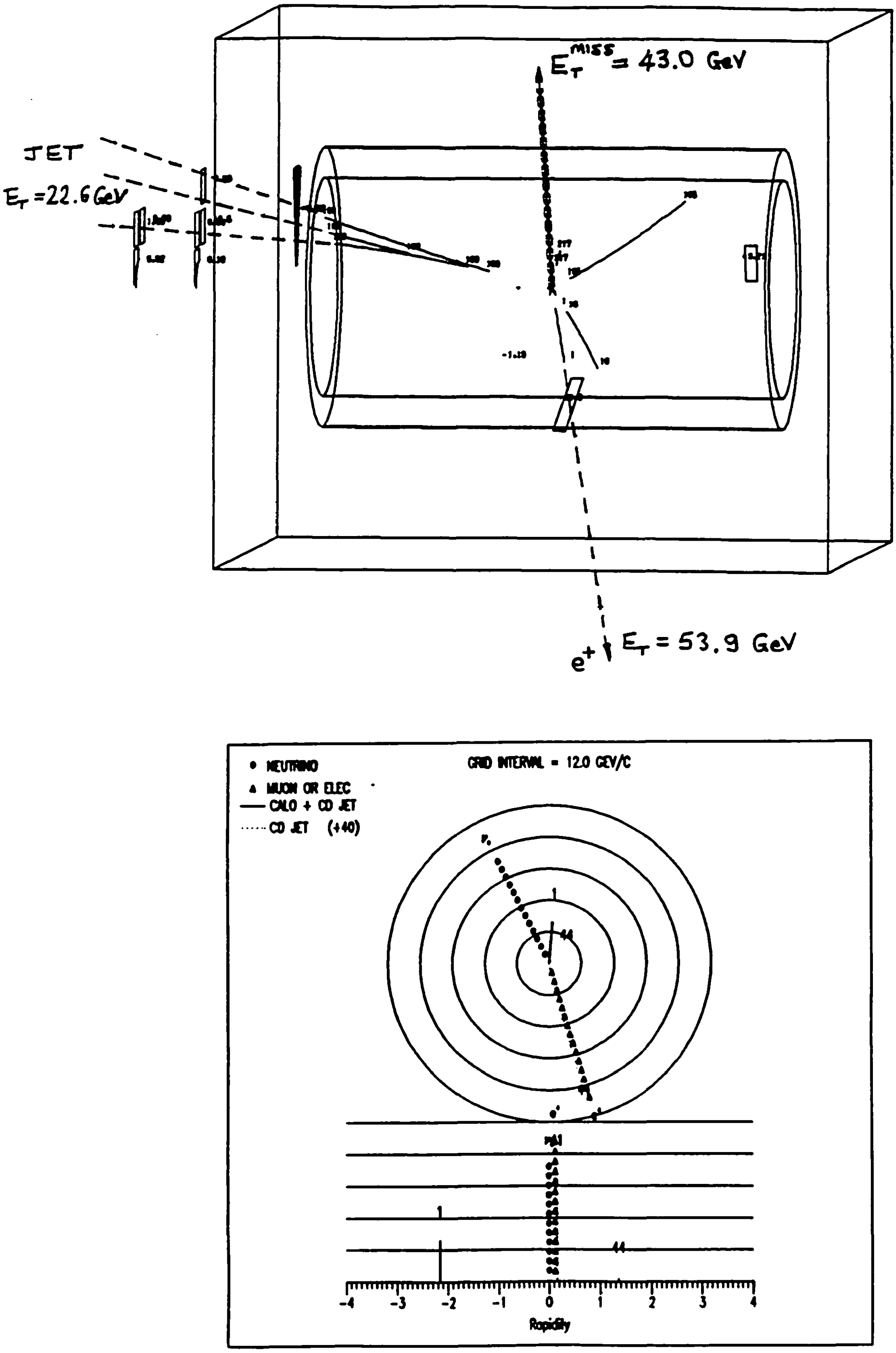

Figure 56: Run/event 11448/746. A typical W + 1jet Candidate

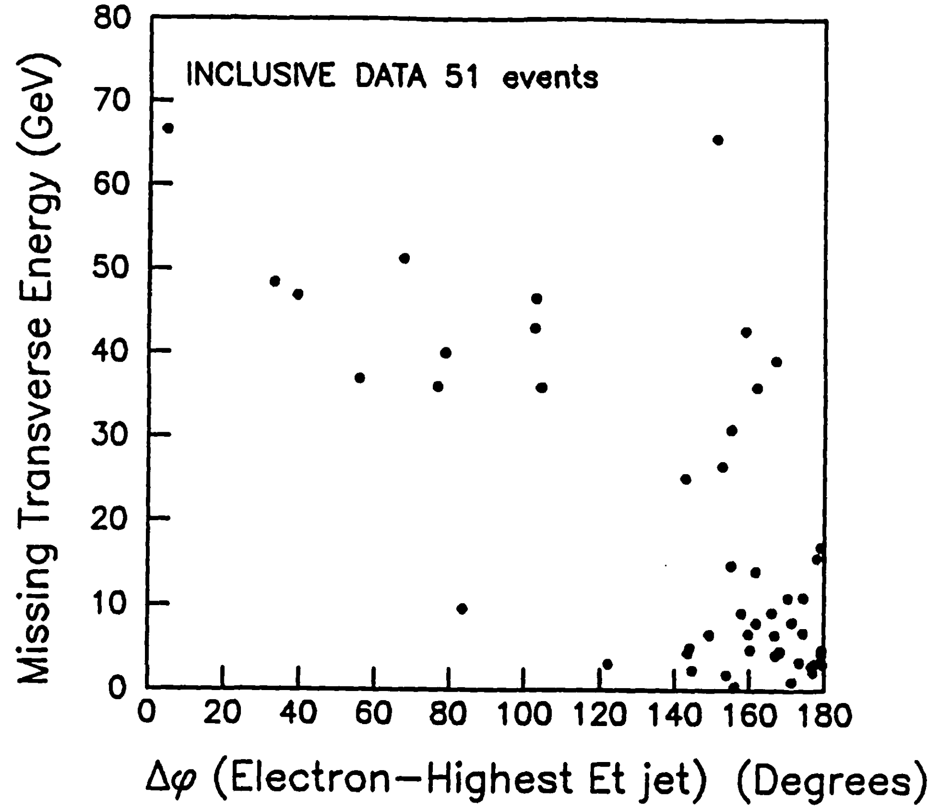

Figure 57: E_t^{miss} vs. $\Delta\phi$(e-jet1)

electron and neutrino, $M_t^{e\nu}$, which is calculated by considering only the two components transverse to the beam direction. If the transverse momentum of the W is negligible in comparison to its mass, $M_t^{e\nu}$ can be written as:

$$M_t = \sqrt{2E_t^e E_t^{miss}(1-\cos\phi)}$$

where ϕ is the difference in azimuthal angle between the electron and neutrino. The transverse mass distribution of the inclusive data and of Monte Carlo predictions for $W \rightarrow e\nu, \tau\nu$ is shown in Figure 58.

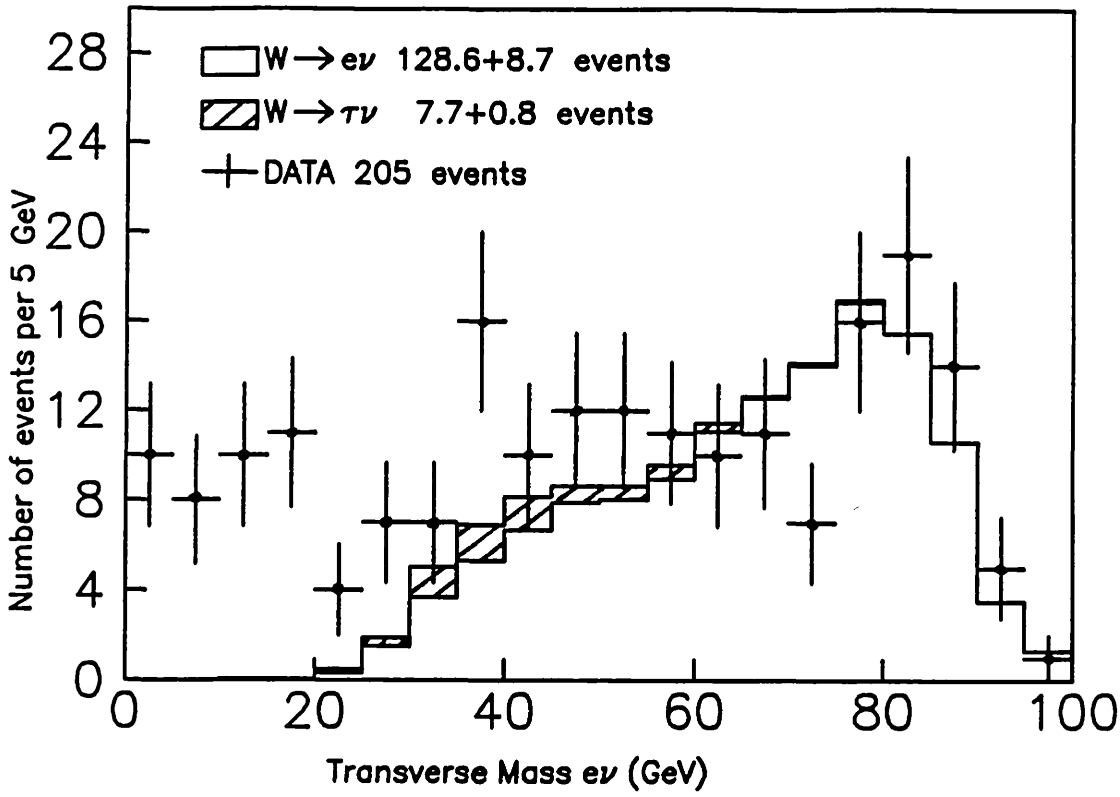

Figure 58: $M_t^{e\nu}$ for the inclusive data and for Monte Carlo predictions of W production

The $M_t^{e\nu}$ distribution for W→eν events is peaked at the W mass, and the unknown longitudinal component of the neutrino momentum manifests itself as a low energy tail. The W→τν events have a low transverse mass because the measured electron is a decay product only carrying a fraction of the τ momentum.

Given reasonable Monte Carlo statistics, the degree to which W events dominate the data sample in various kinematic variables can be determined by plotting the 'W-probability' as a function of a particular variable. For a given value ξ_i of a variable ξ, the probability that the event is a leptonic W decay is given by

$$P(W,\xi_i) = N^W(\xi_i)/(N^W(\xi_i) + N^{tot}(\xi_i))$$

where $N^W(\xi_i)$ is the number of $W \to e\nu, \tau\nu$ events predicted from the Monte Carlo for which the value of the variable ξ is within $\xi_i \pm \delta$ (δ is defined to be typically 1% of the range of the variable ξ), and $N^{tot}(\xi_i)$ is the total number of events predicted by the sum of all other Monte Carlo and background processes for which $\xi = \xi_i \pm \delta$. The W-probability distributions for the variables E_t^{miss}, $M_t^{e\nu}$ and E_t^e are shown in Figures 59,60 and 61 respectively. W events clearly dominate the data sample for $E_t^{miss} > 15$ GeV and for $M_t^{e\nu} > 40$ GeV. The W contribution is also large for $E_t^e > 25$ GeV, though there is a dip in the W-probability around $E_t^e \simeq 50$ GeV where the process $Z^0 \to e^+e^-$ makes a significant contribution.

Most of the W events were removed from the inclusive sample by removing events for which

$$\mathrm{Prob}(W,E_t^{miss}) + \mathrm{Prob}(W,M_t^{e\nu}) > 1.3$$

The efficiencies for this cut on the different physics processes are listed in Table 13.
The W selection removes 139 W candidates from the data. Monte Carlo predicts 7.3 ± 0.8 W events that still remain after the W cut; a scan of all the remaining events on the MEGATEK yielded a further 6 W candidates. These events clearly had $W \to e\nu$ or $W \to \tau\nu$ topology but had low transverse mass. The number of events selected by the W filter is negligible for all non-W physics processes except for the Z^0 channel. The Monte Carlo sample predicts that 1.3 ± 0.3 Z^0 events are removed by the W cut, and a validation scan of all events passing the cut did indeed yield one $Z^0 \to e^+e^-$ candidate, which was discussed in the previous section.

A full analysis of the W candidates in the UA1 data has been carried out elsewhere [36]. The W candidates in this thesis are a subset of the full UA1 W sample because the negligible background to the W signal allows a more relaxed electron selection criteria.

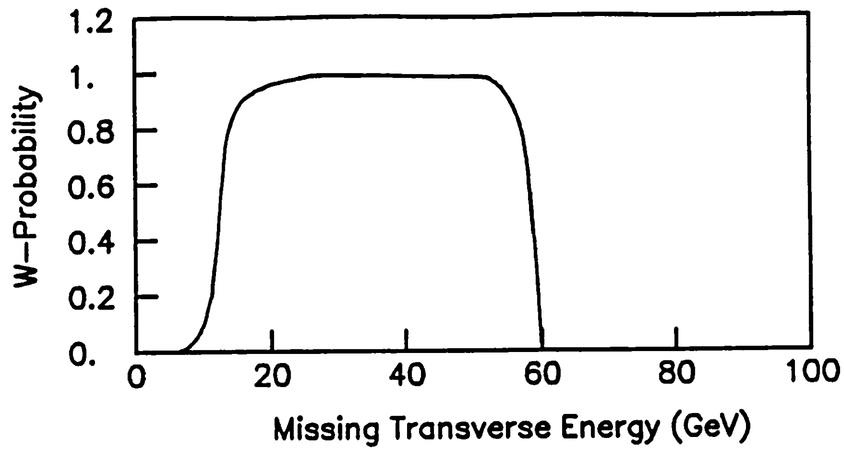

Figure 59: W Probability in E_t^{miss}

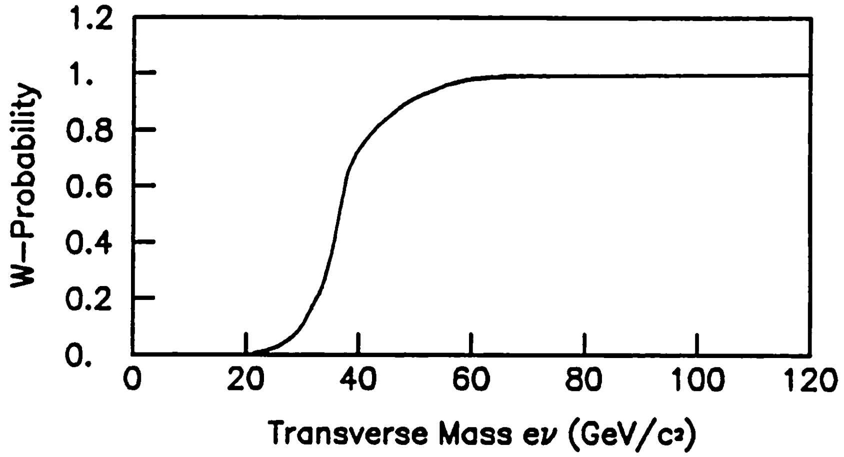

Figure 60: W Probability in $M_t^{e\nu}$

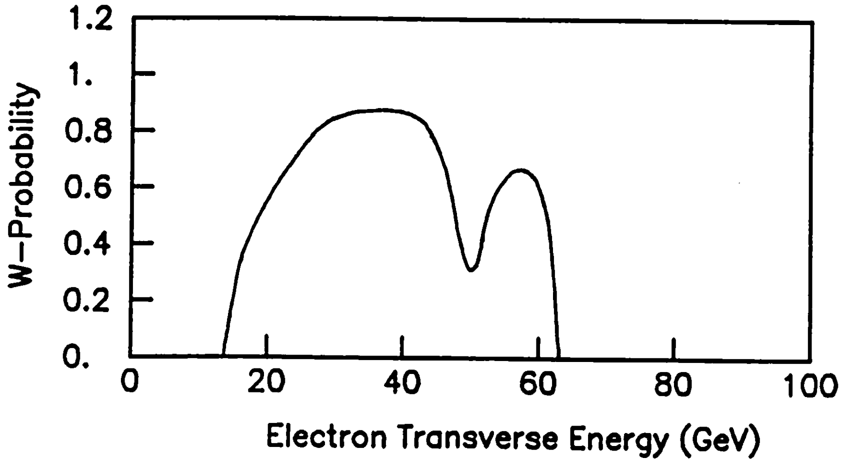

Figure 61: W Probability in E_t^e

Table 13: Efficiency of W selection on various processes

Process	Efficiency(%)	Events removed
$W^{\pm} \rightarrow$ all	94.2	128.5±8.7
$Z^0 \rightarrow$ all	5.2	1.3±0.3
$b\bar{b}/c\bar{c}$	2.3	0.1±0.1
Drell-Yan	3.8	0.3±0.2
J/ψ	0.	0.
Υ	0.	0.
Background	0.	0.
Total:		130.2±8.7
DATA:		139

5.6 Remaining Contributions

After the W candidates and the dielectron events are removed from the inclusive electron sample, 40 events remain. The predicted contribution to the remaining data from each process is listed in Table 14, which shows that the data is consistent with the rates predicted by Monte Carlo. The 0-jet events are clearly dominated by W decays, but the 1-jet events are composed of roughly equal contributions from each physics process and the overlap background. The 2-jet events are dominated by QCD heavy flavour ($b\bar{b}$,$c\bar{c}$) production and the overlap background. The general topology of these remaining events is summarised below.

Figure 62 shows the missing transverse energy distribution for the remaining events. The predicted contribution from W decays is shaded.

The data below $E_t^{miss} < 12$ GeV is explained by those processes from which the missing transverse energy is expected to arise solely from the finite resolution of the calorimeters. Above 12 GeV, the data is well described by the $W \rightarrow e\nu, \tau\nu$ events that did not satisfy the W selection described in Section 5.5. Figure 63 compares the data with Monte Carlo

Table 14: Contributions to the data sample after removal of W and dielectron candidates

Process	No. Evts	0-jet	1-jet	≥2-jet
$W^{\pm}$	7.3±0.9	6.3±0.7	0.9±0.2	0.
Z^0	5.3±0.9	0.3±0.1	4.0±0.5	1.0±0.3
QCD $b\bar{b}/c\bar{c}$	5.4±1.6	0.7±0.3	1.8±0.6	2.9±0.9
DY+J/ψ+Υ	7.0±3.6	1.6±0.9	4.5±2.3	0.9±0.5
Overlap background	8.3±1.3	2.0±0.5	4.0±1.1	2.3±0.6
Conversions	2.8±0.9	1.0±0.5	1.5±0.7	0.3±0.1
TOTAL:	36.1±4.4	11.9±1.4	16.7±2.8	7.4±1.2
DATA:	40	13	18	9
QCD $t\bar{t}$(m_t=30 GeV/c^2)	9.9	1.2	2.1	6.6
QCD $t\bar{t}$(m_t=40 GeV/c^2)	4.6	0.3	0.9	3.7
QCD $t\bar{t}$(m_t=50 GeV/c^2)	4.0	0.5	1.6	1.9
$W \rightarrow t\bar{b}$ (m_t=30 GeV/c^2)	4.3	0.5	2.0	1.8
$W \rightarrow t\bar{b}$ (m_t=40 GeV/c^2)	5.0	0.6	2.5	1.9
$W \rightarrow t\bar{b}$ (m_t=50 GeV/c^2)	4.0	0.1	1.5	2.4

predictions for the difference in azimuth between the electron and highest E_t jet, which shows a correlation at $\Delta\phi$(e-jet1) ≈ 180°. Monte Carlo predictions suggest that there are 0.9±0.2 W events that contain a jet in the remaining 40 events. The reduced missing transverse energy of the W events favours topologies in which a jet is back-to-back with the electron candidate, because the jet diminishes the imbalance in transverse energy created by the electron and the neutrino. For the Z^0 events, the highest E_t jet is either a misidentified second electron or the jet arises from the hadronic tau decay in $Z^0 \rightarrow \tau^+\tau^-$. In both cases the jet is back-to-back with the electron candidate because the transverse momentum of the Z^0 is much smaller than its mass. For all other processes, the topological bias in $\Delta\phi$(e-jet1) is a direct consequence of the cuts on the transverse momentum and isolation of the electron candidate, as discussed in the following sections. It should be noted that the events which have a $\Delta\phi$(e-jet1) of less than about 160° are predomi-

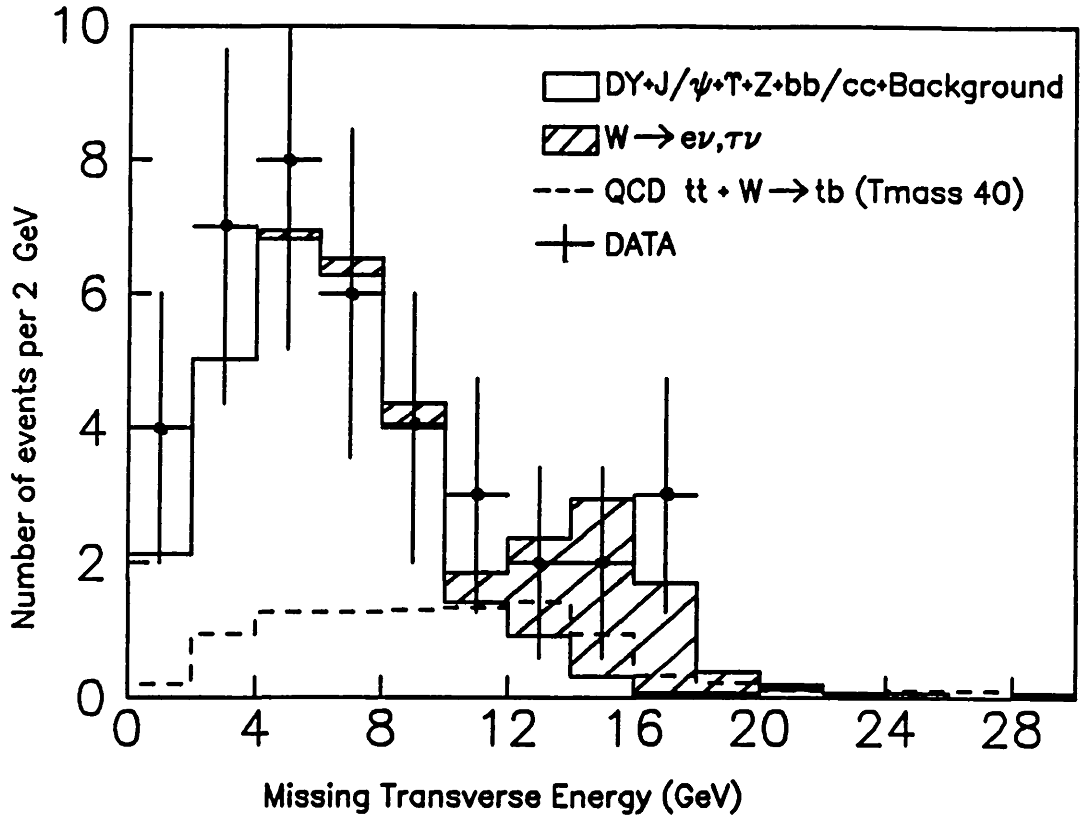

Figure 62: E_t^{miss} *for remaining contributions*

nantly 2-jet events which arise from the higher order QCD diagrams. In these events, one or more of the partons prior to the hard scatter carries a significant transverse momentum. The vector sum of the transverse momenta of the electron and jet is therefore non-zero and $\Delta\phi$(e-jet1) is reduced.

The transverse energy of the electron and the highest-E_t jet are shown in Figures 64 and 65 respectively. Unfortunately the various processes are indistinguishable in these two variables, though the remaining $Z^0 \rightarrow e^+e^-$ events (in which one electron has hadronic punchthrough and simulates a jet) give a high transverse energy tail to both distributions.

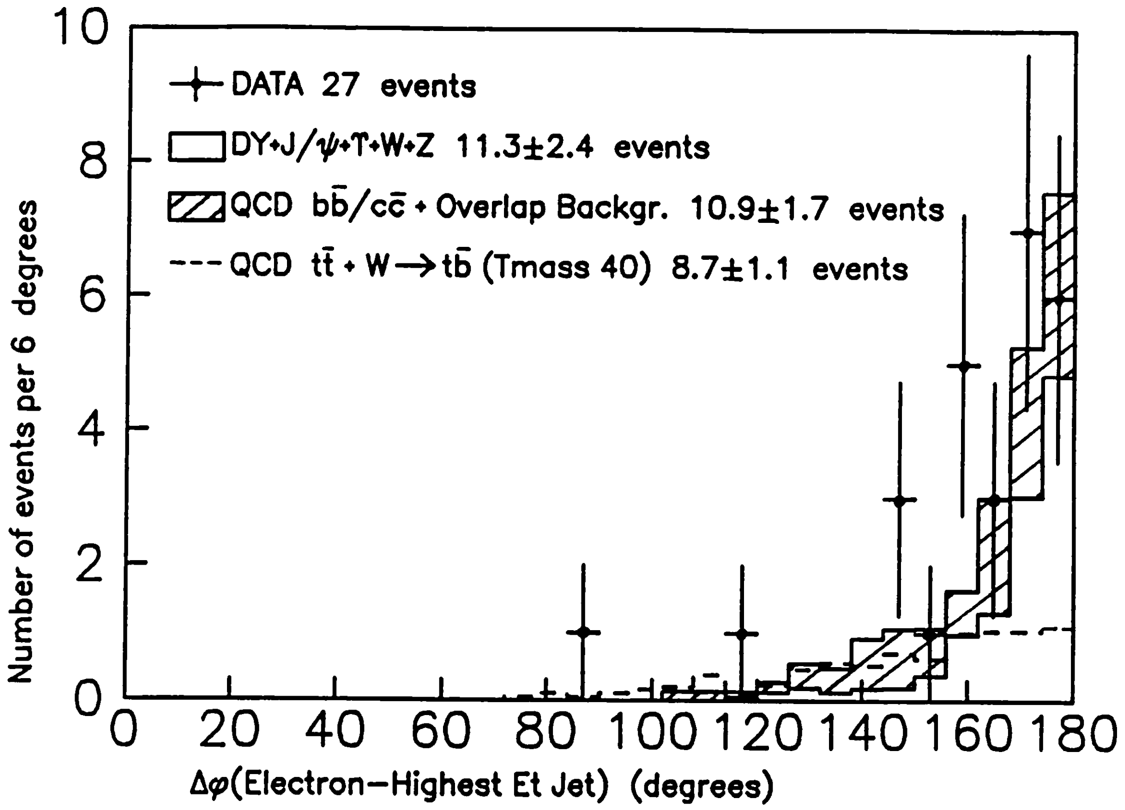

Figure 63: $\Delta\phi$*(electron-highest* E_t *jet)*

Clearly the majority of events in this data sample that remain after after removal of W and dielectron candidates consist of the electron back-to-back in azimuth with a jet. Moreover, given the poor statistics, there are no features in E_t^e, E_t^{jet1} or E_t^{miss} which can distinguish between the different processes that make up the sample.

5.6.1 $Z^0 \rightarrow \tau^+\tau^-$ *Production*

The Monte Carlo predicts that the data sample contains 2.0±0.4 $Z^0 \rightarrow \tau^+\tau^-$ events in which one of the taus decays to an electron ($\tau^\pm \rightarrow e^\pm \nu_e \nu_\tau$). The second tau may decay to

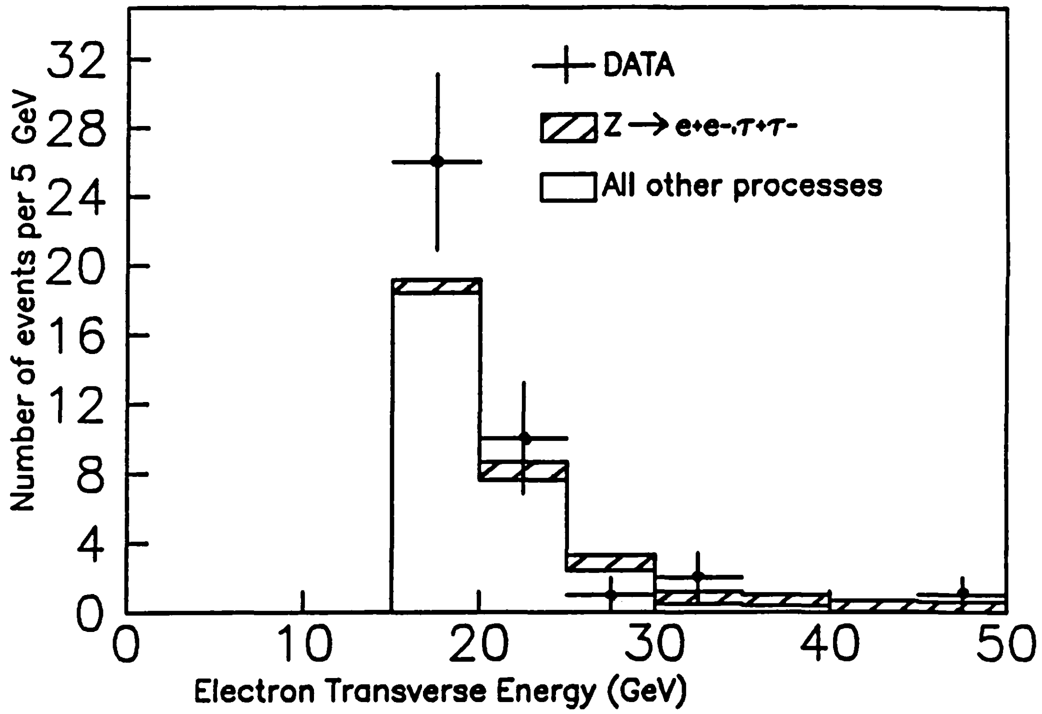

Figure 64: Electron transverse energy

an electron, a muon ($\tau^{\pm} \rightarrow \mu^{\pm} \nu_{\mu} \nu_{\tau}$) or to hadrons. Such events have an isolated electron back-to-back in ϕ with either an isolated electron, an isolated muon or a hadronic jet respectively.

The search for $Z^0 \rightarrow \tau^+\tau^-$ events in this data sample has yielded just one candidate for

$$Z^0 \rightarrow \tau^+\tau^-, \ \tau^- \rightarrow e^- \nu_e \nu_\tau, \ \tau^+ \rightarrow \mu^+ \nu_\mu \nu_\tau$$

The event is shown in Figure 66.

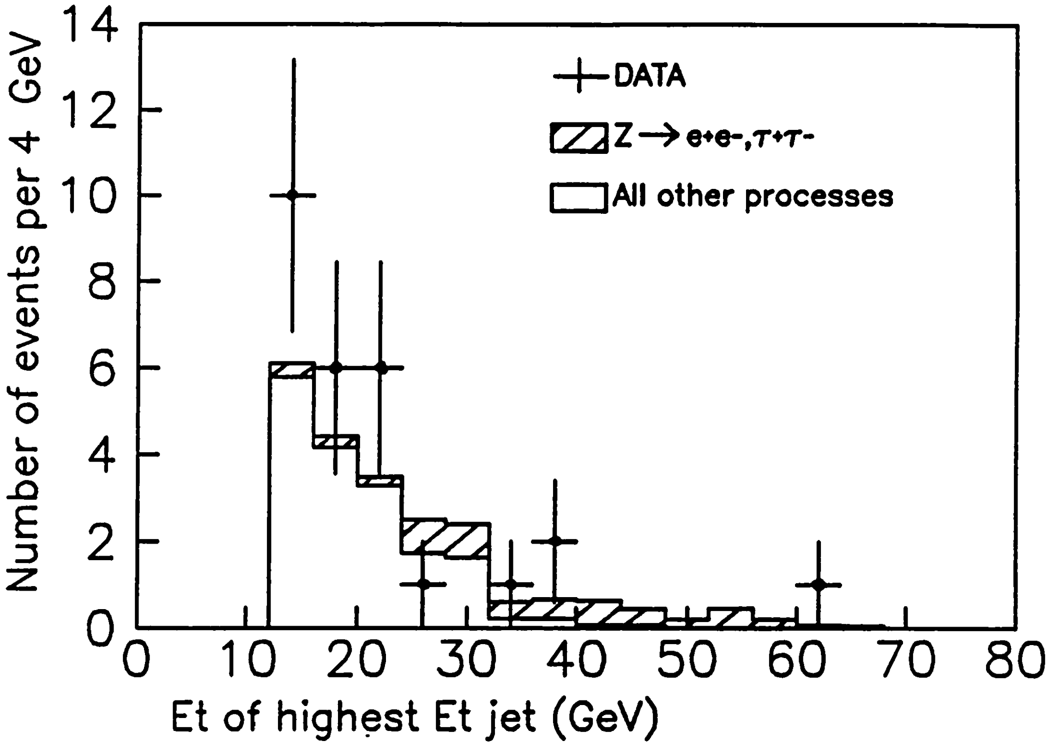

Figure 65: Transverse energy of the highest-E_t jet

The tau has a low mass so its hadronic decay will produce a jet that is both narrow and has a small charged track multiplicity. The search for $Z^0 \rightarrow \tau^+\tau^-$ candidates in which the second tau decays hadronically uses a tau-likelihood [43], L_τ, for the highest-E_t jet in each of the data events. The tau-likelihood is calculated using three variables that help to characterize the 'pencil' like nature of the tau jet:

1. $\Sigma E_t(\Delta R < 0.4)/\Sigma E_t(\Delta R < 1.)$ where ΣE_t is the sum of transverse energy contained within a radius ΔR from the jet axis in pseudorapidity-phi space ($\Delta R = \sqrt{(\delta\eta^2 + \delta\phi^2)}$);

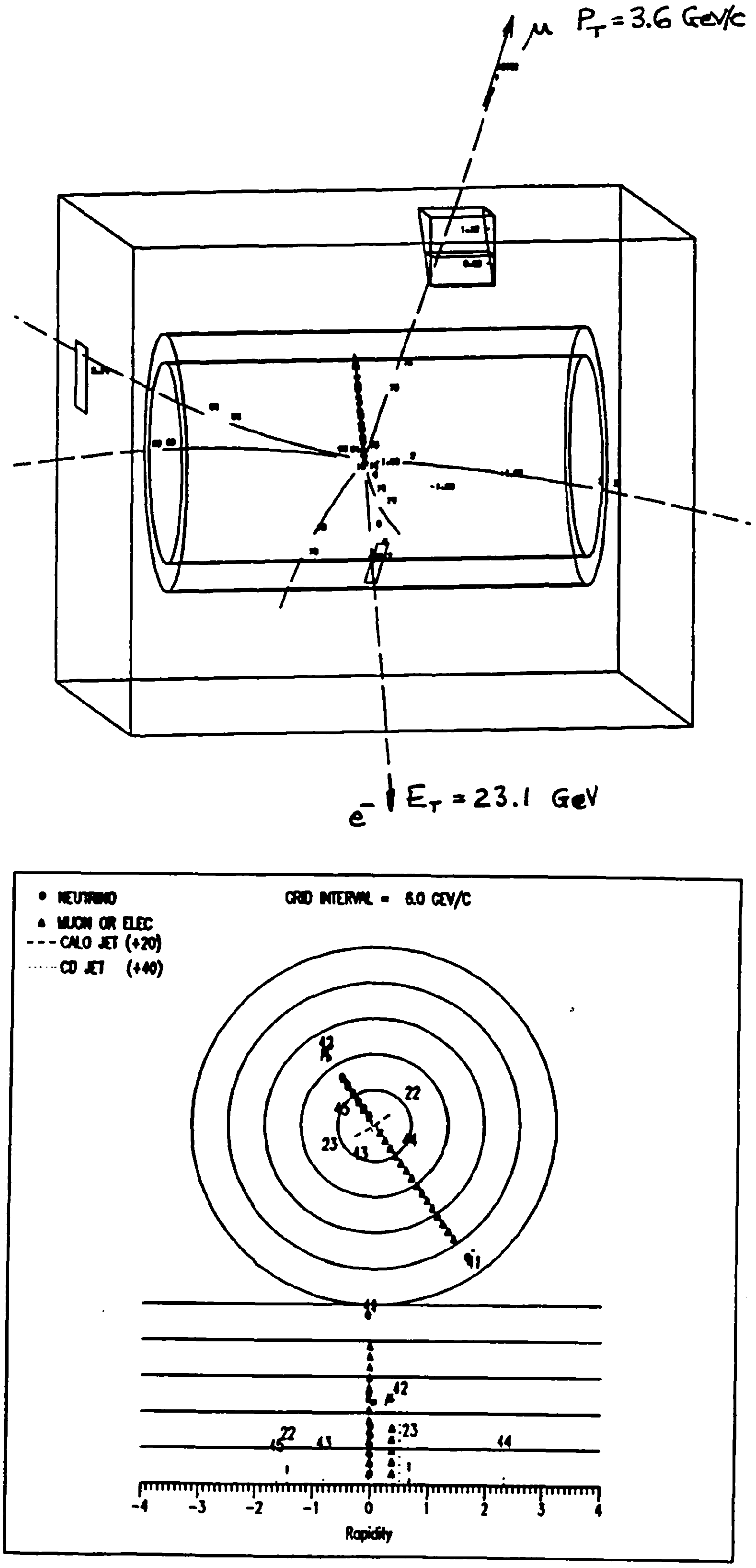

Figure 66: Run/event 17049/1000. A $Z^0 \rightarrow \tau^+\tau^-$ Candidate

2. The number of CD tracks in the jet with $P_t^{CD} > 1$ GeV/c and ΔR(track-jet axis) < 0.4;

3. ΔR between the jet axis (defined by the jet energy deposition in the calorimeters) and the highest P_t track in the jet.

Figure 67 shows the Monte Carlo prediction for the L_τ distributions for various processes.

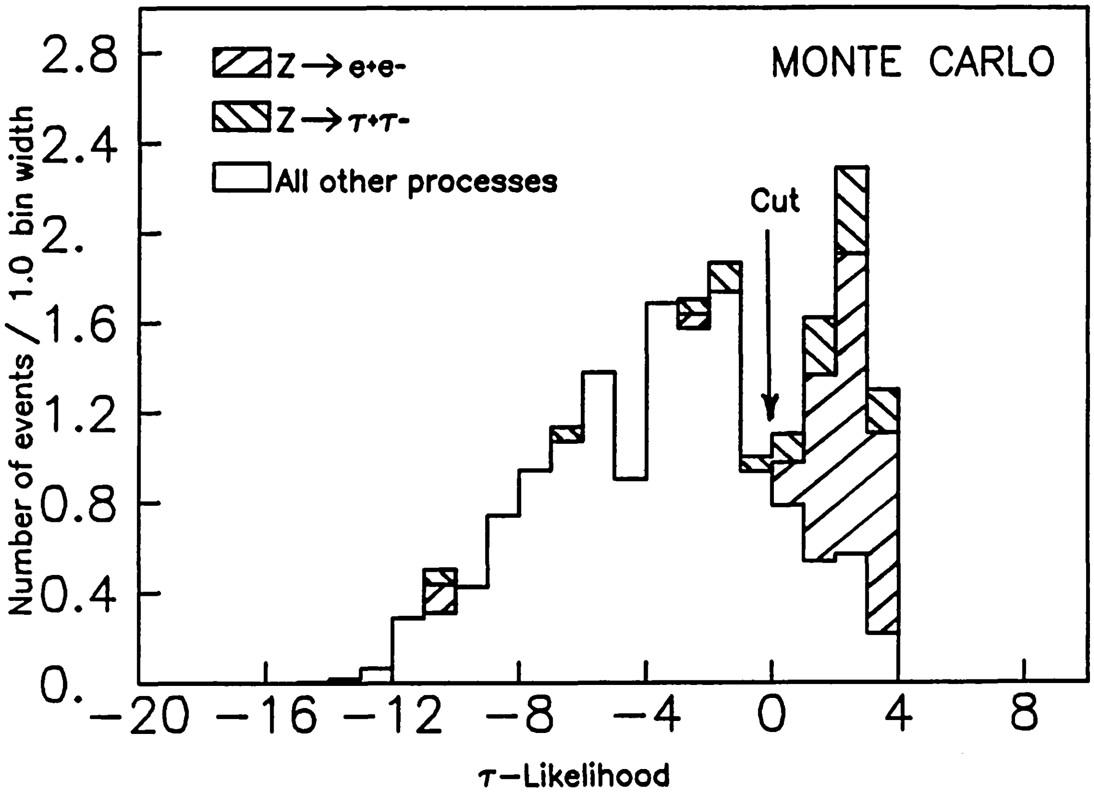

Figure 67: Tau-likelihood for various processes

There is a peak in the tau-likelihood above $L_\tau > 0$ which arises from Z^0 production. The number of events from each process with $L_\tau > 0$ is summarised in Table 15.

Table 15: Efficiency of $L_\tau > 0$ Selection

Process	Efficiency(%)	Number of events
$Z^0 \to \tau^+\tau^-$	83.5	1.0±0.3
$Z^0 \to e^+e^-$	89.5	3.2±0.4
DY+J/ψ+Υ	27.1	1.4±0.8
QCD $b\bar{b}/c\bar{c}$	5.0	0.2±0.1
$\pi^\pm + n\pi^0$	8.9	0.7±0.2
TOTAL:		6.5±1.0
DATA:		3.0

Although the selection efficiency for $L_\tau > 0$ is high for $Z^0 \to \tau^+\tau^-$ events, only one event is expected from this process. Most of the events that satisfy $L_\tau > 0$ are predicted to be $Z^0 \to e^+e^-$ events in which the misidentified second electron has some hadronic punchthrough and therefore resembles the narrow hadronic jet expected of the tau. The sum of the contributions from other physics processes and from the overlap background is also significant.

Three data events pass the $L_\tau > 0$ cut: events 9957/955, 15730/956 and 17554/1144. Event 15730/956 has been discussed in a previous section and is a candidate for $Z^0 \to e^+e^-$. The other two events are shown in Figures 68 and 69.

The two events are discussed below:

- Event 17554/1144 has an electron with $E_t^e = 17.9$ GeV back-to-back in azimuth with a jet of $E_t = 18.1$ GeV. $E_t^{miss} = 8.0$ GeV which is large but compatible with the finite resolution of the calorimeters. The jet contains

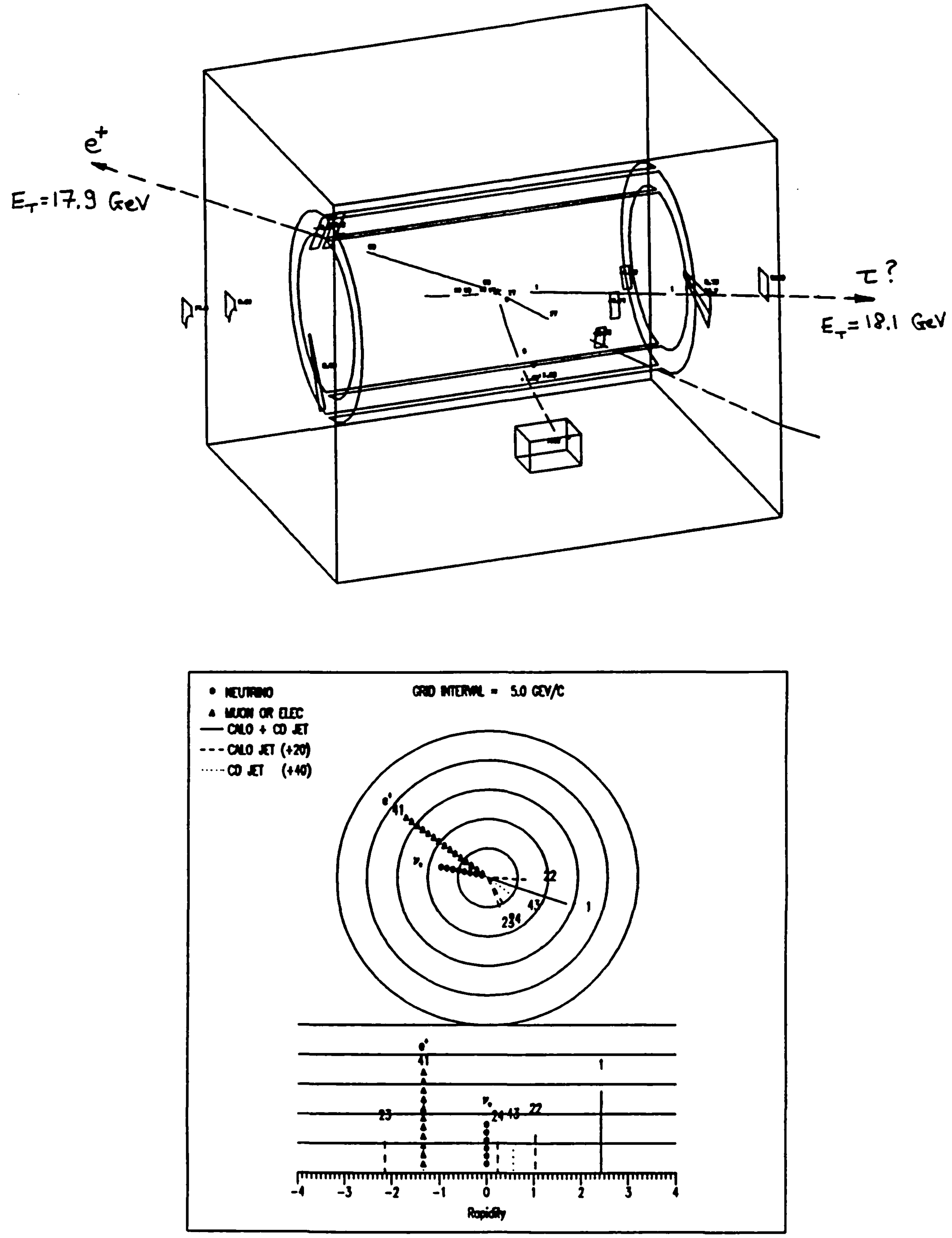

Figure 68: Run/event 17554/1144. An event with $L_T > 0$

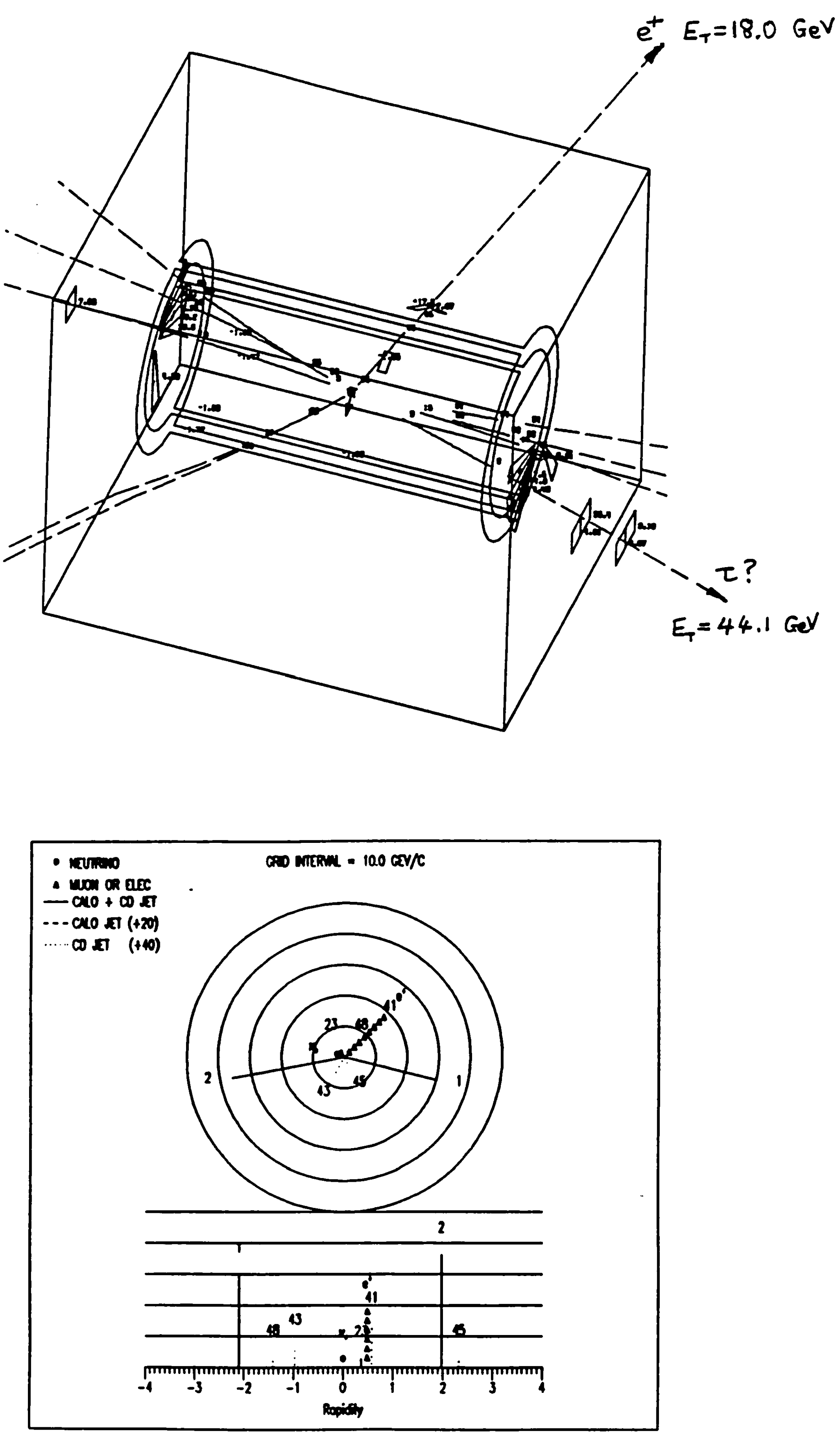

Figure 69: Run/event 9957/955. An event with $L_T > 0$

a single track with $P_t = 8.0$ GeV/c. The invariant mass of the electron and jet calculated using CD parameters is 70.7± 1.5 GeV.

- Event 9957/955 has an electron with $E_t^e = 18.0$ GeV and two high transverse energy jets ($E_t^{j1} = 44.1$ GeV, $E_t^{j2} = 36.9$ GeV).The highest-E_t jet consists of a single track with $P_t = 7.3$ GeV/c. The missing transverse energy is negligible (E_t-$^{miss} = 2.6$ GeV), and the invariant mass of the electron and jet (using CD parameters) is 21.0± 1.0 GeV.

The event 17554/1144 is a possible candidate for a Z^0 decay, given the high invariant mass of the electron and jet. However, the jet could be a misidentified electron and the event a $Z^0 \rightarrow e^+e^-$ candidate instead of $Z^0 \rightarrow \tau^+\tau^-$. Event 9957/955 seems unlikely to be a $Z^0 \rightarrow \tau^+\tau^-$ candidate given the multi-jet nature of the event and the small missing transverse energy. This event will be discussed further in the section on heavy flavours.

5.6.2 J/ψ and Υ Production

Electrons produced in the lowest order Drell-Yan diagram of Figure 15 can carry a transverse momentum of roughly half the mass of the virtual photon. The J/ψ and Υ particles have a mass of approximately 3.1 GeV/c^2 and 9.8 GeV/c^2 respectively, so electrons produced by J/ψ or Υ decays in the lowest order Drell-Yan process will not satisfy the 15 GeV cut imposed on the electron transverse energy in this data sample. However, J/ψ or Υ production may make a small contribution to the data sample by the higher order Drell-Yan diagrams of Figure 16. The J/ψ or Υ is then produced at high-P_t because it recoils against a hard gluon bremsstrahlung; if the J/ψ or Υ decays asymmetrically then one of the electrons carries most of the J/ψ or Υ transverse momentum, which may then be sufficient to pass the selection cut. The topology of J/ψ or Υ events in this data sample is therefore that of an electron back-to-back in azimuth with a hadronic jet of roughly equal P_t. The prediction for the number of events from J/ψ and Υ production in this data sample are 3.7 and 0.9 events respectively: the relatively large contribution from the J/ψ being due to the cross-section for J/ψ production being up by a factor of almost 10 compared to Υ production.

In principle, the $|\cos\theta^*|$ distribution of the jet could be used to distinguish the J/ψ and Υ events, because jets from initial state gluon bremsstrahlung are peaked towards 1 in $|\cos\theta^*|$. However, the cut on the jet transverse energy at 12 GeV introduces a bias in favour of central jets, so given the poor statistics there is no obvious peak in $|\cos\theta^*|$ for the events containing one jet.

The search for J/ψ or Υ candidates in this thesis simply requires that the high-P_t electron is accompanied by a soft track which has an opposite charge to the electron, with an invariant mass of the electron and soft track being close to either the J/ψ or Υ mass. No Υ candidates were found, but two possible J/ψ candidates are shown in Figures 70 and 71.

The features of both events are discussed below:

- Run/event 7343/1254. This event has an electron ($E_t^e = 19.3$ GeV) almost back-to-back in ϕ with a jet ($E_t^{jet} = 18.4$ GeV). The jet is consistent with initial state bremsstrahlung with $|\cos\theta^*| = 0.93$, and balances a small missing transverse energy $E_t^{miss} = 4.6$ GeV. A soft track accompanies the electron and the invariant mass of the electron and track is 3.15 ± 0.13 GeV/c^2.
- Run/event 15988/910. The event has an electron with $E_t^e = 18.3$ GeV almost back-to-back in ϕ with a jet of $E_t^{jet} = 16.6$ GeV. The jet is consistent with initial state bremsstrahlung with $|\cos\theta^*| = 0.90$, and balances a small missing transverse energy $E_t^{miss} = 6.5$ GeV. A soft track accompanies the electron giving an invariant mass of 3.15 ± 0.20 GeV/c^2.

The two events have nearly identical topologies and clearly originate from the same process. However, a drawback to the hypothesis that these events are J/ψ candidates is that

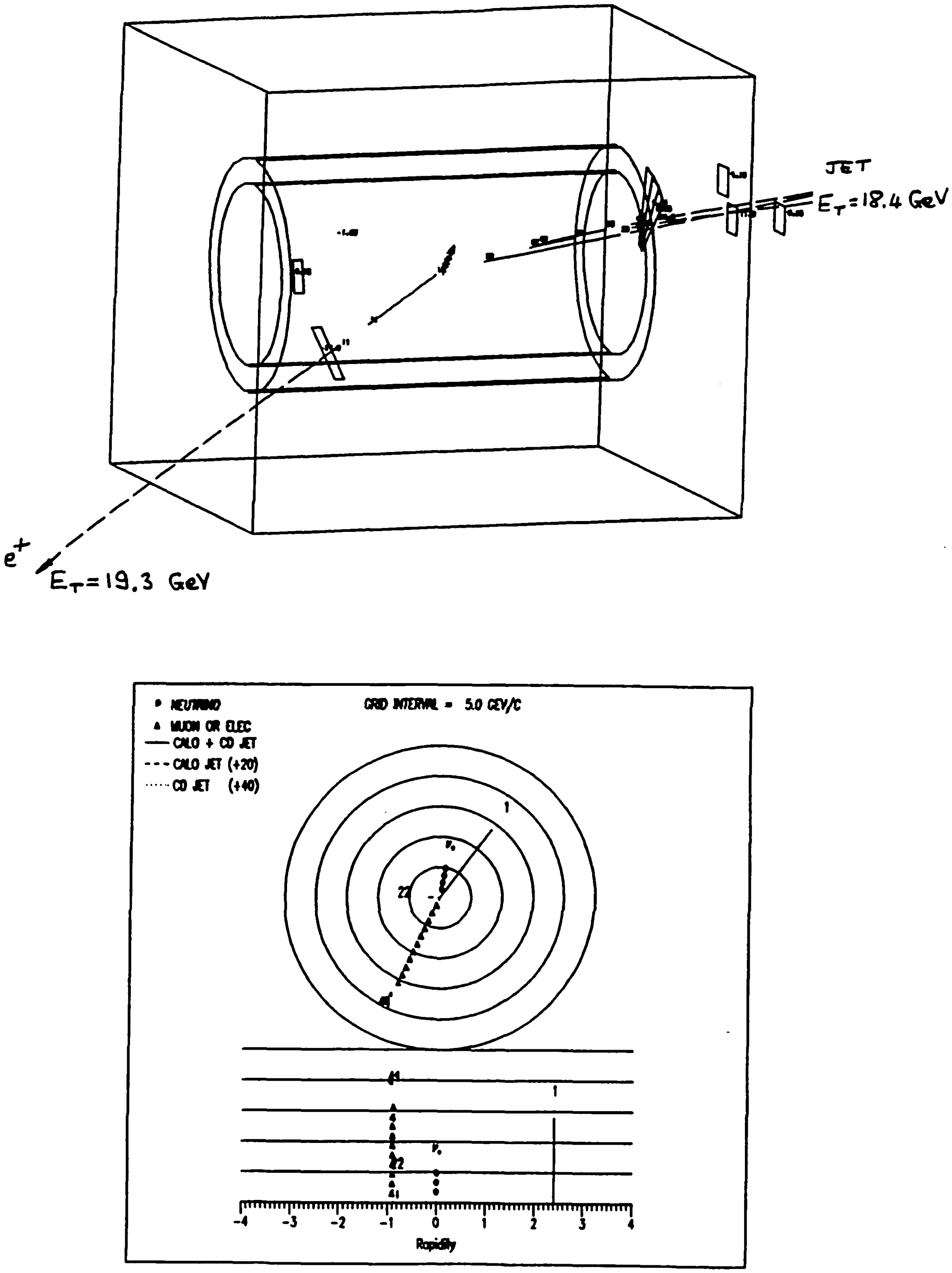

Figure 70: Run/event 7343/1254. A possible J/ψ candidate.

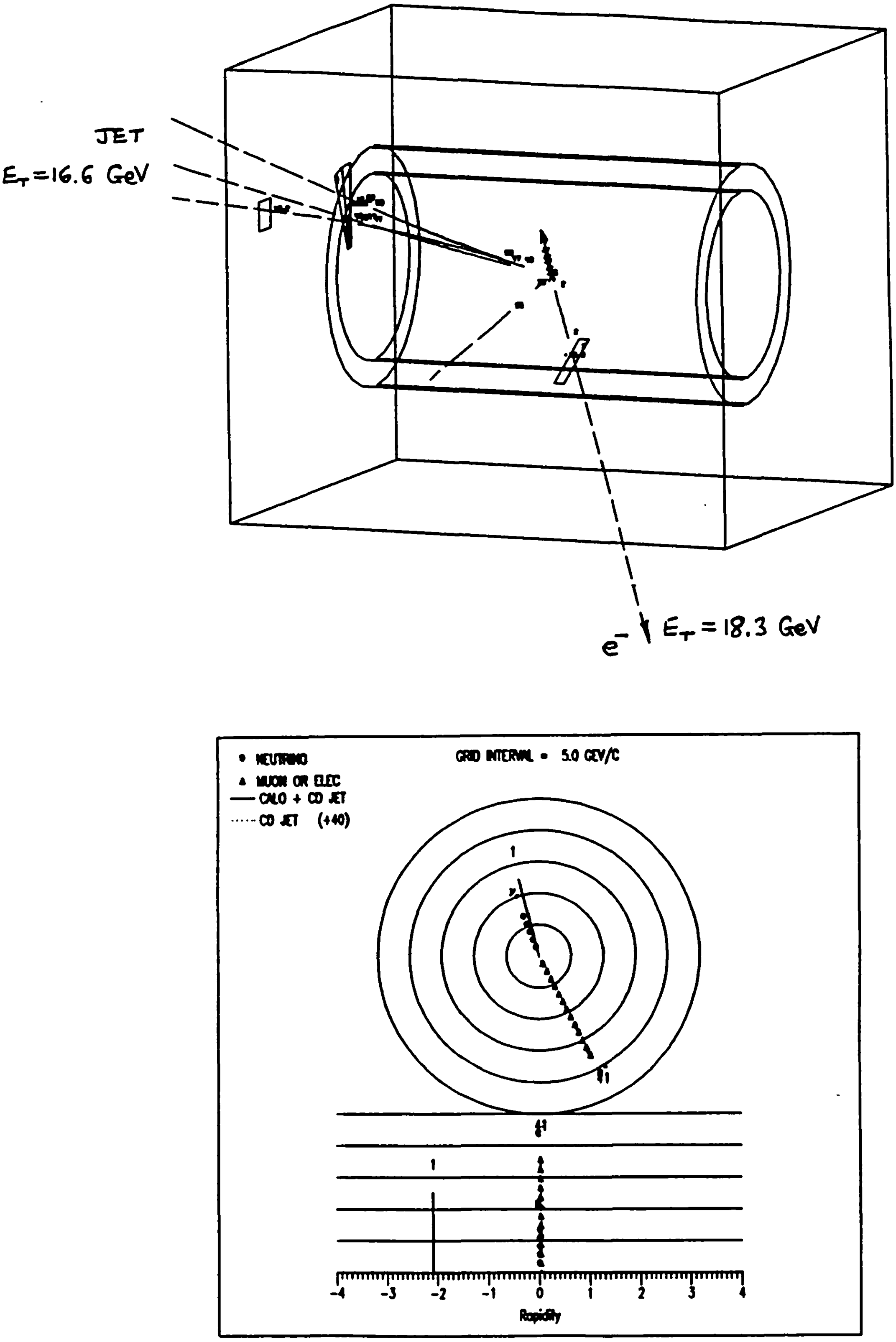

Figure 71: Run/event 15988/910. A possible J/ψ candidate.

the second electron may just be one of many soft tracks that arise from the spectator system. The alternative interpretation though is that these events are W decays, but this is unlikely given the small missing transverse energy.

5.6.3 Heavy Flavour Production

This section discusses the contribution to the electron data sample from the QCD production of heavy flavours ($b\bar{b}$,$c\bar{c}$). A search for topologies that are consistent with the expectations from top quark production is also described, though a detailed analysis of the limits on top quark production in this data sample have been given elsewhere [39].

Heavy flavours can contribute to the electron data via the 3-body semileptonic decay, $Q \rightarrow q + \ell + \nu$. The angular separation of the 3 decay products (and hence the isolation of the lepton) is sensitive to the mass of the decaying heavy flavour. An electron from b quark decay ($b \rightarrow c\ell\nu$) will, in general, be accompanied by a hadronic jet because the mass of the b is not usually sufficient to separate the electron from the fragmentation products of the c quark. The isolation cuts imposed by electron identification in the UA1 detector therefore essentially veto b or c decays from making a contribution to this sample. However, if the electron is the leading particle in the decay (which is not so unlikely given the hard fragmentation function of heavy flavours), the hadronic energy from the daughter quark may be negligible and the isolation cuts can be satisfied.

The expected topology of QCD $b\bar{b}$ or $c\bar{c}$ production by the lowest order QCD diagrams of Figure 19 is therefore an isolated electron which is back-to-back in azimuth with a central hadronic jet (from the recoiling b or c quark). Additional jets arise from the higher order QCD diagrams of Figure 14. Unfortunately, the topology of QCD $b\bar{b}$,$c\bar{c}$ events is in general indistinguishable from that of overlap background events, because both processes orginate from basic QCD $2 \rightarrow 2$ hard scatter. The difference is that for QCD $Q\bar{Q}$ production ($Q = c,b,..$), the hard fragmentation function and the semileptonic decay of the heavy quark produces the electron back-to-back with a jet; for the overlap background (QCD $q\bar{q}$ production, q = all flavours or gluons), it is the fluctuation in the charged particle multiplicity of a jet that produces the misidentified pion back-to-back with a jet.

The top quark is heavy (the top quark has not been observed at the highest energies available in e^+e^- collisions at PETRA [44] which excludes a top mass below 23 GeV/c^2) and relatively slow in the laboratory frame. The three decay products of the semileptonic decay of top therefore have a wide angular separation, and the electron from top decay is expected to be isolated. After imposing the electron selection, the contribution from the $Z^0 \to t\bar{t}$ channel is negligible but the other two production channels should still provide a substantial contribution provided $m_t < 60$ GeV/c^2 [39]. The two remaining top production channels have different kinematics. For the decay of the W intermediate vector boson into the third doublet of weak currents, $W \to t\bar{b}$ followed by $t \to \ell\nu b$, events are expected to have 2 central jets (one from the recoiling $\bar{b}$ quark and the other from the semileptonic decay of the t), an isolated electron and some missing energy. The $W \to t\bar{b}$ candidates should have several features that make them distinguishible from other sources (such as QCD $b\bar{b}$,$c\bar{c}$ production and the overlap background) of e + 2jet events:

1. The invariant mass of the ($b\bar{b}\ell\nu$) system should cluster around the W mass;
2. the invariant mass of the ($b\ell\nu$) system should cluster around the top mass;
3. the jet from the recoiling $\bar{b}$ should have a Jacobian peak in transverse energy at around M_W.

QCD $t\bar{t}$ events are expected to have a more complex multi-jet topology than that of the $W \to t\bar{b}$ process. One of the top quarks decays semileptonically to produce an isolated electron, some missing energy and a low transverse momentum hadronic jet. The second top quark could either manifest itself as a broad hadronic jet or as up to three subjets from, say, $t \to bu\bar{d}$.

Both top production channels are therefore expected to have ≥ 2 jets, so the UA1 search for top has been based on a the e + $\geq$2jet data sample, which is dominated by overlap background and QCD $b\bar{b}/c\bar{c}$ production.

Top quark production is sensitive to E_t^{out}, defined as the component of the electron transverse energy perpendicular to the plane formed by the $p\bar{p}$ axis and the highest-E_t jet. The distribution of E_t^{out} for various processes is shown in Figure 72.
E_t^{out} is large for an electron from the semileptonic decay of top because of the high top mass, but is peaked towards zero for Drell-Yan, J/ψ, Υ, W and Z events. However, QCD $b\bar{b}$,$c\bar{c}$ events and the overlap background also have a high energy tail in E_t^{out}. Unfortunately, this does not arise from the mass of the b or c quark, but indirectly from the momentum imparted to the electron and the highest-E_t jet by a hard gluon bremsstrahlung (the regions in E_t^{out} from 2-jet events are shaded in Figure 72). E_t^{out} can therefore only effectively distinguish top decays in 1-jet events, but this is difficult because of the low event rate from top.

In principle top events can be distinguished from QCD $b\bar{b}/c\bar{c}$ and overlap background by the missing transverse energy and by $\cos\theta^*$ of the second highest-E_t jet. Figure 62 shows a comparison between the data and Monte Carlo predictions for E_t^{miss} with the sum of QCD $t\bar{t}$ and $W \rightarrow t\bar{b}$ (for a top mass of 40 GeV/c^2) contributions shown as a dashed line. The large top mass can impart a significant transverse momentum to the neutrino: in particular the neutrino transverse momentum is expected to be substantial in the region where E_t^{miss} from W decays and other processes is expected to be small ($E_t^{miss} \sim$ 10-12 GeV).

The distribution of $|\cos\theta^*|$ for the second highest-E_t jet should be flat for $W \rightarrow t\bar{b}$ and QCD $t\bar{t}$ events, because the jet arises from the fragmentation of the recoiling b or t quark. In all other processes, the second jet arises predominantly from initial state gluon bremsstrahlung, so the distribution in $|\cos\theta^*|$ is peaked at 1. Figure 73 shows $|\cos\theta^*|$ of the second highest-E_t jet for the Monte Carlo, the overlap background and the data.

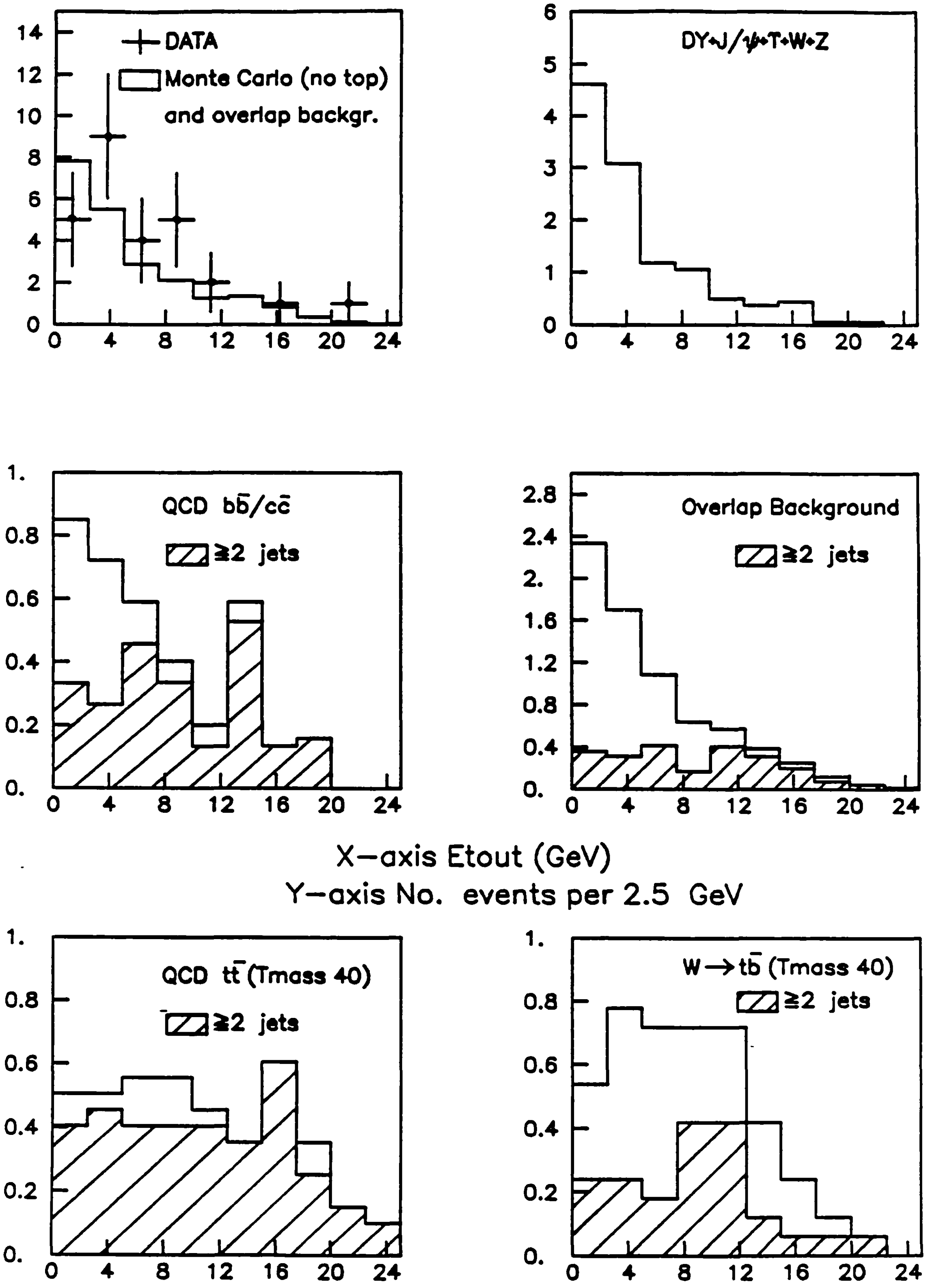

Figure 72: E_t^{out} for various processes

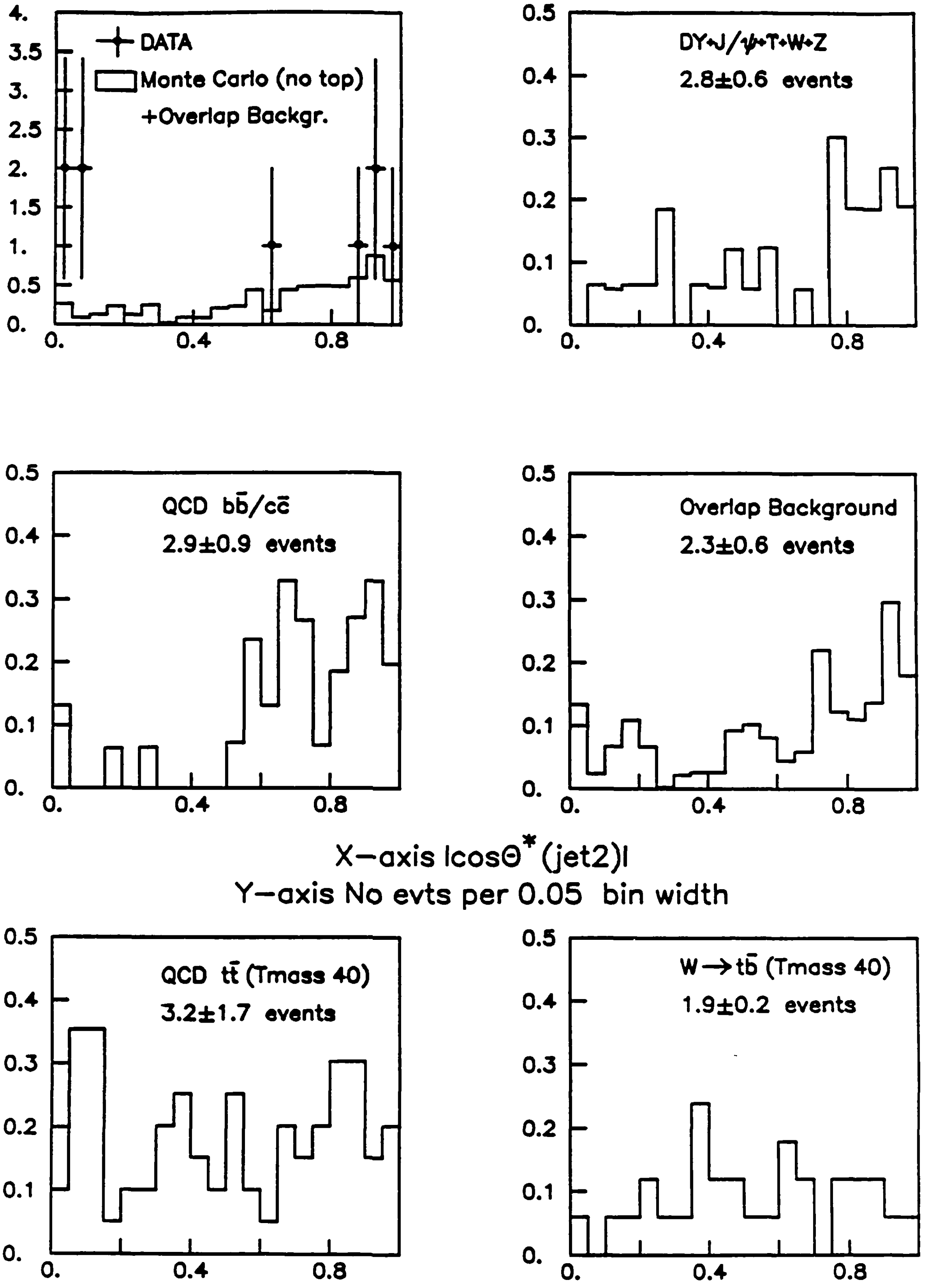

Figure 73: cosθ^* *of the second highest* E_t *jet*

Unfortunately, the number of events in the electron data is too small to draw any conclusions from $|\cos\theta^{*}(\text{jet2})|$, though it will be an effective filter for top events with larger statistics.

A lower limit on the mass of the top quark in the UA1 electron data has been derived using the above considerations in reference [39]. In particular, an analysis of the shapes of the E_t^{miss} distribution and the number of jets per event has excluded a top mass below 47 GeV/c^2 at 95% confidence level.

In this thesis, an alternative approach was used for a top search by determining the degree of isotropy of events. The large mass of the top quark suggests that top events should have a fairly isotropic final state topology. A study of the global energy flow in the calorimeters also has the benefit of removing any dependence on jet-finding algorithms.

The energy flow in the plane transverse to the beam direction for various processes after the W and dielectron cuts is shown in figure 74. The profiles show the transverse energy deposited in the calorimeters plotted as a function of the azimuthal angular separation from the electron. Calorimeter cells associated with the electron have been ignored, and the direction of rotation in azimuth from the electron is defined to be the direction in which $\Delta\phi$(electron-highest E_t jet) $< 180^0$

The azimuthal E_t profiles do not necessarily show the profile of a single event, but rather the consistency with which events conform to a given topology. For example, the Z^0 profile has a sharp peak towards 180^0 superimposed above the flat profile of the spectator system, because most Z^0 events have a high-P_t misidentified electron back-to-back with the primary electron. The Drell-Yan, J/ψ and Υ events have a similar profile because these events have a jet from gluon bremsstrahlung back-to-back with the electron. The peak is wider because it reflects the width of the jet. The peak in QCD $b\bar{b}/c\bar{c}$ events is produced by the fragmentation of the recoiling b or c quark. However, the peak is more broad because gluon bremsstrahlung often produces a second jet which reduces $\Delta\phi$(electron-jet). The gluon bremsstrahlung also accounts for the activity above the level

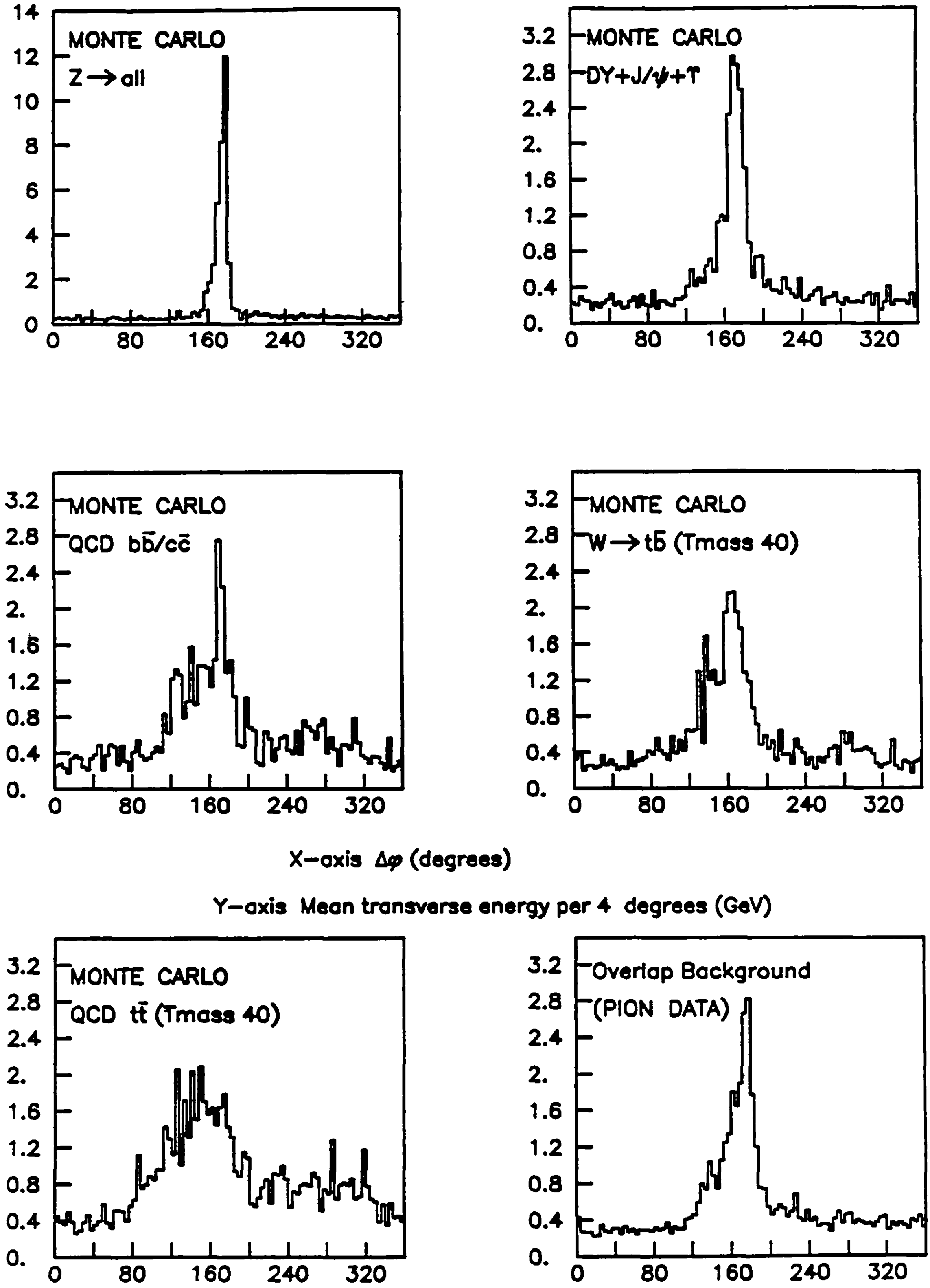

Figure 74: Transverse energy profiles in the plane transverse to the beam axis

of the spectator system for $\Delta\phi > 180^0$. A similar interpretation can be given to the overlap background events: a large peak towards 180^0 is due to the dominance of the $\pi^{\pm}+n\pi^0$ back-to-back with a single jet, but the peak has a low angle tail down to $\Delta\phi \simeq 120^0$ due to the presence of events with a second jet. The second jet from gluon bremsstrahlung has no correlation in azimuth and manifests itself as an apparent raising of the level of the spectator system above $\Delta\phi > 180^0$. The profile for QCD $t\bar{t}$ events is flatter with significant activity above the spectator system throughout the range in $\Delta\phi$, reflecting the isotropic multi-jet nature of these events.

The energy profile of an event in the plane transverse to the beam direction can be parameterised by 'circularity' which has a value of one for a perfectly circular transverse energy profile in azimuth, and approaches zero for a single energy deposition that subtends a small angle at the beam crossing point (as for example if the event contained only the energy deposition from a single electron). The direction of the circularity axis is along a line describing the net flow of energy in the azimuthal plane, and is undefined for a perfectly circular transverse energy profile. In this data sample, the circularity axis always pointed to within $\pm 5^0$ of the electron direction. Circularity is calculated in much the same way as sphericity which was developed to establish the existence of jets in e^+e^- physics [45], except that only components of energy transverse to the beam axis are considered. The 2-dimensional matrix T is constructed,

$$T_{ij} = \Sigma(E_i^t \times E_j^t)$$

where i and j refer to the two components transverse to the beam direction of the energy vector associated with a calorimeter cell, and the sum is over all calorimeter cells. Circularity is then defined as the maximum eigenvalue of the T matrix divided by ΣE_t^2, the sum of the square of the transverse energies of all calorimeter cells (which keeps the calculation dimensionless). The circularity axis is defined by the associated eigenvector. Figure 75 shows circularity distributions for various processes and the data after removing W and dielectron events.

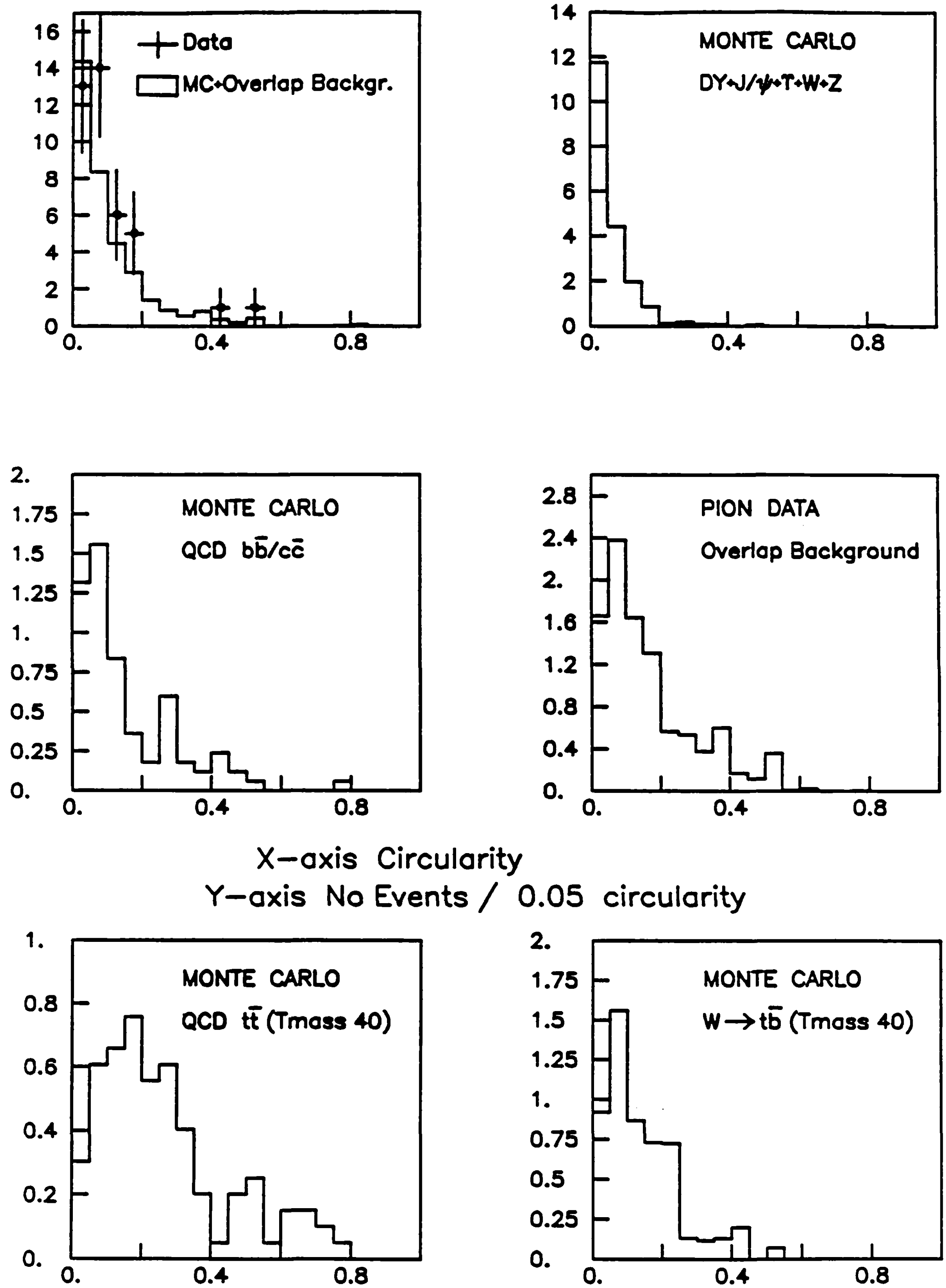

Figure 75: Circularity Distributions for various processes

Circularity appears to be effective in enhancing heavy flavour and overlap background events with respect to all other processes. The first bin (13 events, circularity < 0.05) is dominated by the Drell-Yan, J/ψ, Υ, W and Z mecanisms, but heavy flavour production and the overlap background dominate at higher values of circularity. Two data events (7443/509 and 9957/955) have anomolously high values of circularity. Event 9957/955 was shown in Figure 69, and event 7443/509 is shown in figure 76.

Parameters of the two events are summarised below:

- Event 7443/509. This event has $E_t^e = 19.2$ GeV and $E_t^{miss} = 3.1$ GeV. The event contains two jets: $E_t^{j1} = 25.5$ GeV with $|\cos\theta^*(j1)| = 0.19$, and $E_t^{j2} = 12.3$ GeV with $|\cos\theta^*(j2)| = 0.65$. $\Delta\phi$(e-jet1) = 115.6°, $\Delta\phi$(e-jet2) = 17.5°. The invariant masses of the systems (electron,neutrino,jet2) and (electron,neutrino,both jets) are 46.2 GeV/c^2 and 81.0 GeV/c^2 respectively.
- Event 9957/955. This event has $E_t^e = 18.0$ GeV and $E_t^{miss} = 2.3$ GeV. The event also contains two jets: $E_t^{j1} = 44.1$ GeV with $|\cos\theta^*(j1)| = 0.96$ and $E_t^{j2} = 36.9$ GeV with $|\cos\theta^*(j2)| = 0.98$. $\Delta\phi$(e-jet1) = 144.6°, $\Delta\phi$(e-jet2) = 59.9°. The invariant masses of the systems (electron,neutrino,jet2) and (electron,neutrino,both jets) are 98.4 GeV/c^2 and 339 GeV/c^2 repectively.

Both jets in event 9957/955 are peaked towards 1 in $|\cos\theta^*|$ and are therefore consistent with initial state bremsstrahlung, even though the transverse energy of both jets is abnormally large. The highest-E_t jet is more likely to be associated with hard scatter since it is more back-to-back with the electron in azimuth. This event is probably QCD $b\bar{b}/c\bar{c}$ or overlap background.

In event 7443/509 the two jets are fairly central. The invariant masses $M(e\nu j_2)$ and $M(e\nu j_1 j_2)$ are consistent with the process $W \rightarrow t\bar{b}$ provided the top quark mass is about 40 GeV/c^2. However, the event rate at high circularity is in good agreement with predictions from QCD $b\bar{b}/c\bar{c}$ and overlap background, and given the the lack of events with similar

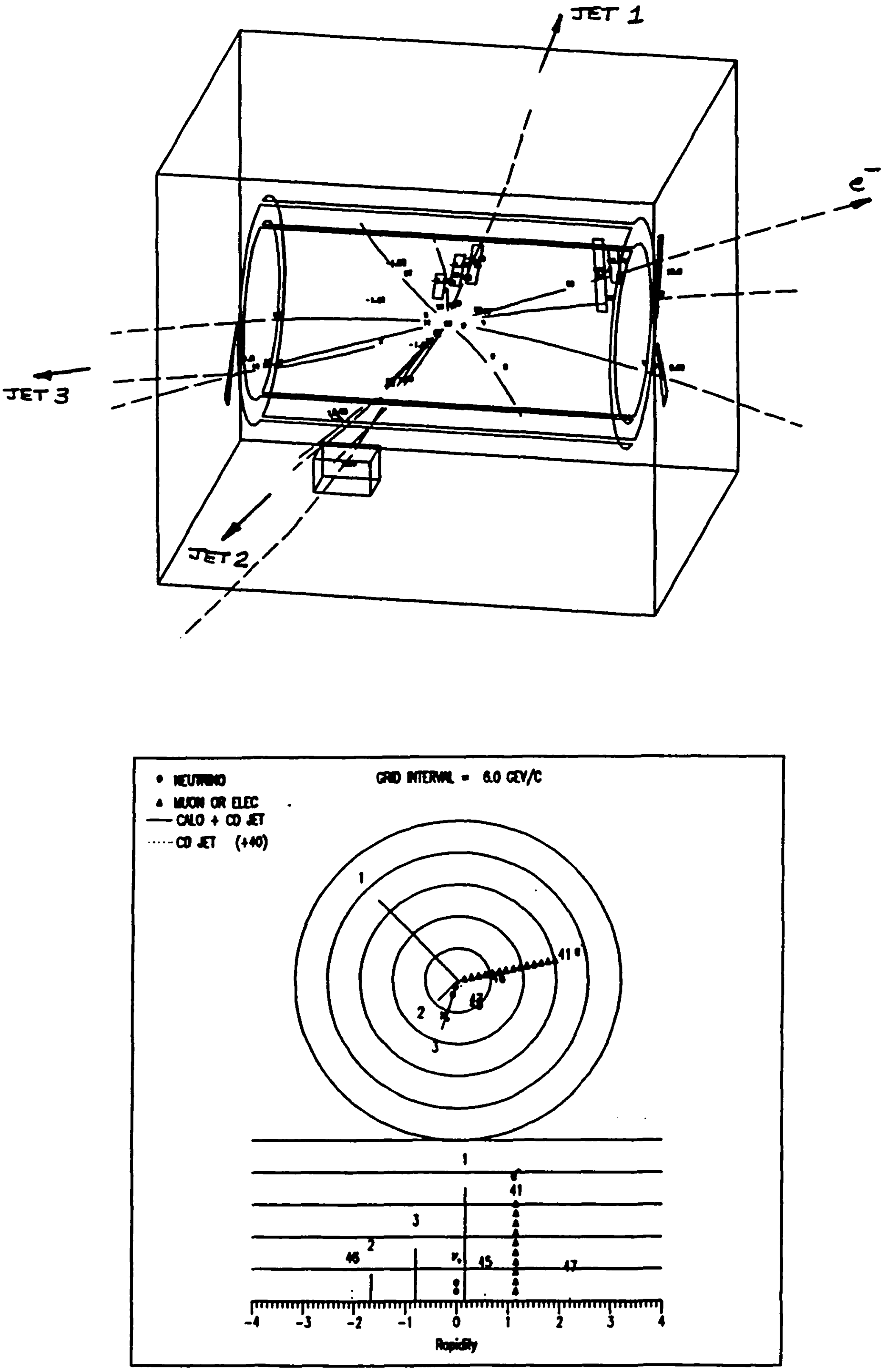

Figure 76: Run/event 7443/509. A high circularity event

topology to 7443/509 it seems more likely that this event is one of the two standard processes rather than $W \rightarrow t\bar{b}$.

Further work on circularity, for example the correlation between circularity and the transverse energy distribution in rapidity, and the effect on circularity of removing calorimeter cells associated with the electron, did not lead to any improved discrimation between heavy flavour and other processes. In addition, sphericity was calculated in much the same way as circularity except that all three components of energy in calorimeter cells are used to form a 3-dimensional matrix. After the removal of W and dielectron candidates, it was found that sphericity could not easily discriminate between processes because the highest-E_t jet has a flat distribution in $|\cos\theta^*|$ for each process. A central electron with a jet at large $|\cos\theta^*|$ from, say, a J/ψ candidate can give as high a value of sphericity as heavy flavour processes.

5.7 Summary and Conclusions

This chapter has decribed an inclusive analysis of the electron candidates recorded by the UA1 experiment that satisfy the electron selection criteria described in Chapter 4. Most of the events in the electron data sample are $W^\pm \rightarrow e^\pm \nu$ and $Z^0 \rightarrow e^+e^-$ decays, because the stringent cuts on the isolation and the transverse energy of the electron candidates introduces a bias against all other channels for electron production. Fortunately, the $W^\pm$ and Z^0 candidates can be easily identified by their distinctive final state topologies: the leptonic $W^\pm$ decay produces a high-P_t electron back-to-back in azimuth with a high-P_t neutrino, and the leptonic Z^0 decay produces two high-P_t electrons with a dielectron mass clustered around the Z^0 mass. The $W^\pm$ and Z^0 channels are background-free, but for all other channels the electron selection biases the topology to that of the electron back-to-back in azimuth with a hadronic jet. The 1-jet events are composed of roughly equal contributions from each of the electron production channels and the overlap background, but events containing a second jet from a hard gluon bremsstrahlung are dominated by QCD $b\bar{b}/c\bar{c}$ production and the overlap background.

The rate of events in the electron data sample is in good agreement with predictions for standard model processes and the background. However, the topological bias and the poor statistics for the electron production channels other than $W^{\pm}$ and Z^0 decays are such that on an event by event basis, the different production mechanisms cannot in general be distinguished from one another. In particular the electron sample is unsuited to studies of J/ψ and Υ production (because of the stringent cut on electron transverse energy) and QCD $b\bar{b}/c\bar{c}$ heavy flavour production (because identification of an electron candidate requires the electron to be isolated).

Heavy flavour ($b\bar{b}$,$c\bar{c}$) production and overlap background can be enhanced with respect to all other processes by demanding two jets. Variables that favour heavy flavour production such as E_t^{out}, $\Delta\phi$(electron-highest E_t jet) and circularity merely reflect the predominantly 2-jet nature of these events. There is no clear evidence of top quark production in the electron data sample. A study by the UA1 Collaboration of the kinematical variables expected to be most sensitive to top quark production in the electron channel has yielded [39] a lower limit on the top mass of 47 GeV/c^2 at 95% confidence level.

APPENDIX A

THE UA1 COORDINATE SYSTEMS

Descriptions of the UA1 apparatus use the cartesian coordinate system defined in Table 16.

Table 16: The UA1 Cartesian Coordinate System

x	Points horizontally along the beam axis in the $\bar{p}$ direction of motion
y	Points upwards along the vertical axis
z	Points horizontally outwards from the centre of the SPS
θ	Angle with respect to the $\bar{p}$ axis
ϕ	Azimuthal angle around the beam axis, measured from the horizontal plane

The angles used in the cartesian coordinate system are shown schematically in Figure 77.

The cartesian coordinate system is not suitable for describing kinematical properties, because the multiplicity of particles produced in minimum bias data ($p\bar{p}$ collisions without a hard scatter) is not flat with respect to the polar angle, θ. Instead we use the azimuthal angle, ϕ, and the rapidity, defined as

$$y = 0.5 \log_e[\frac{E+p_l}{E-p_l}]$$

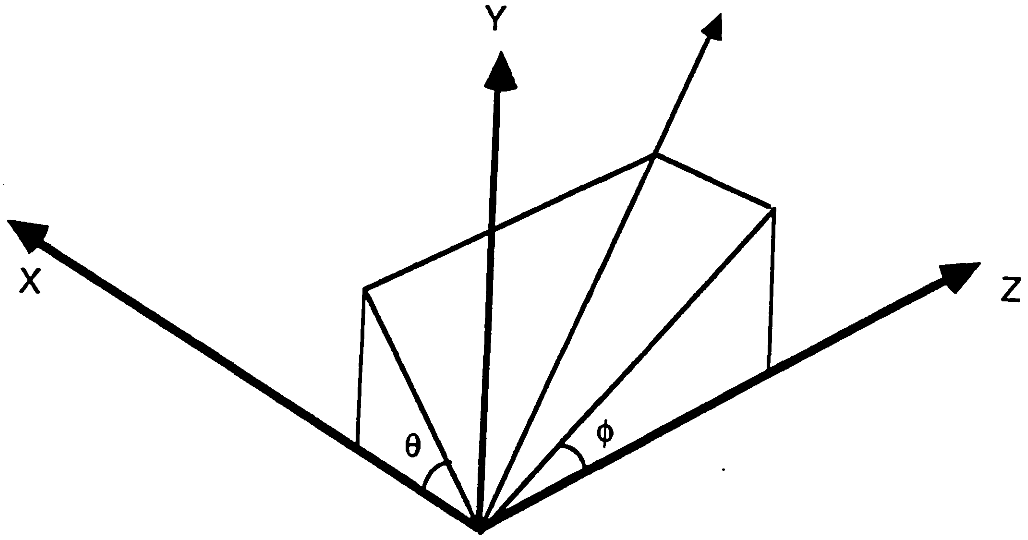

Figure 77: Definition of θ and ϕ in the UA1 cartesian coordinate system

where E is the energy of the particle and p_l is the component of the particle momentum parallel to the beam axis. If the mass of the particle is negligible relative to its momentum, this reduces to the pseudorapidity:

$$\eta = -\log_e[\tan(\theta/2)]$$

Differences in η and ϕ are invariant under boosts along the beam axis, and the track multiplicity and transverse energy distributions are flat in (η,ϕ) space in the central part of the detector for minimum bias data. Any significant deviations in this level of background can then be said to come from the hard scatter.

REFERENCES

[1] C.Rubbia, P.McIntyre and D.Cline. Producing Massive Intermediate Vector Bosons with Existing Accelerators. Proc. of the International Neutrino Conference: Aachen 1976.

[2] A.Astbury et.al. A 4π solid angle detector for the SPS used as a Proton-Antiproton collider at a centre of mass energy of 540 GeV. CERN/SPSC/78-061978.

[3] S.Glashow. Nuclear Physics 22 (1961) 579.

S.Weinberg. Physics Review Letters 19 (1967) 1264

A.Salam. 1968 in Elementary Physics Theory. Relativistic groups and Analyticity (Nobel Symposium No.8), edited by Svartholm, Almquist and Wiksell, Stockholm.

[4] J.D.Dowell, The UA1 Experiment with ACOL, CERN-EP/86-193, 20 November 1983, and talk given at the 6th Topical Workshop on Proton-Antiproton Collider Physics, Aachen, 30 June-4 July 1986.

[5] G.Hall, D.Robinson, I.Siotis. Evaluation of the Performance of Silicon Photodiodes in Combination with Plastic Scintillators. Nuclear Instruments and Methods A245 (1986) 344-350.

[6] G.Hall, D.Robinson, C.Seez, I.Siotis. Electromagnetic Shower Position Detection with a Scintillator-Photodiode Hodoscope. Nuclear Instruments and Methods A253 (1987) 491-499.

[7] M.G.Albrow et al., A Uranium Scintillator Calorimeter with Plastic-Fibre Readout. Nuclear Instruments and Methods A256 (1987) 23-37.

[8] M.G.Albrow et al., Performance of a Uranium/Tetramethylpentane Electromagnetic Calorimeter. CERN-EP/87-55. Submitted to Nuclear Instruments and Methods.

vsics. Addison-Wesley Publishing

Inc..

[12] M.Gell-Mann,

mesons.

[13] G.Zweig, CERN 8182/TH401 and 8419/TH412.

[14] B.Combridge,J.Kripganz and J.Ranft. Hadron Producti erse Momentum and QCD. Phys. Lett. 70B (1977) 234.

[15] R.D.Field and R.P.Feynman. A Parameterization of the Properties of Quark Jets. Nucl. Phys. B136 (1978) 1.

[16] C.Peterson,D.Schlatter,I.Schmitt and P.M.Zerwas. Scaling Violations in Inclusive e^+e^- Annihilation Spectra. Phys. Rev. D27 (1983) 105.

[17] C.W.Fabjan and T.Ludlam. Calorimetry in High-Energy Physics. Ann. Rev. Nucl. Part. Sci. 1982. 32:335-89.

[18] S.Van der Meer. Stochastic cooling and the accumulation of antiprotons. Reviews of Modern Physics, 57 3 part 1 (1985).

[19] M.Calvetti,J.Timmer,Y.G.Xie. Measuring dE/dx in the Central Detector. UA1/TN83-80 1983.

[20] C.Cochet et al. The Central Electromagnetic Calorimetry in UA1, Nuclear Instruments and Methods A243 (1986) 45.

[21] B.Aubert et al. The Bouchons End Cap Electromagnetic Calorimeters of UA1, LAPP.EXP.85-10 July 1985.

[22] M.J.Corden et al. Central Hadron Calorimeter of UA1, Nuclear Instruments and Methods A238 (1985) 273.

[23] C.Bacci et al., A Calorimeter with Wavelength Shifter Read-out for Particles at Small Angles in Proton-Antiproton Collisions, Nuclear Instruments and Methods 200 (1982) 195.

[24] A.Astbury et al. The Calorimeter Trigger. Nuclear Instruments and Methods A238 (1985) 288.

[25] R.Bock,E.Pagiola,J.Zoll. HYDRA Systems Manual, CERN publication, March 1972.

[26] I.Wingerter. Estimation du Bruit de Fond aux Electrons de $E_t > 15$ GeV Produits par Interaction $P\overline{P}$ a $\sqrt{s} = 540$ GeV dans le Detecteur UA1 du CERN, These de Doctorat 1985.

[27] J.P.Lees,I.Wingerter. UA1 Technical Note UA1 TN87-53.

[28] C.Ghiglino et al. UA1 Technical Note UA1 TN87-52.

[29] C.Albajar et al.(UA1 Collaboration), Study of Heavy Flavour Production in Events with a Muon Accompanied by jet(s) at the CERN Proton-Antiproton Collider. CERN-EP/87-189. Submitted to Zeitschrift fur Physik.

[30] C.Albajar et al.(UA1 Collaboration), Phys. Lett. 186B (1987) 237 and 247.

[31] F.Paige and S.D.Protopopescu. ISAJET Monte Carlo, BBNL 38034 (1986).

[32] E.Eichten et al., Rev. Mod. Phys. 56 (1984) 579.

E.Eichten et al., Rev. Mod. Phys. 58 (1986) 1065.

[33] G.C.Fox and S.Wolfram. A Model for Parton Showers in QCD. Nucl. Phys. B186 285.

[34] C.Albajar et al.(UA1 Collaboration), Analysis of the Highest Transverse Energy Events Seen in the UA1 Detector at the $Sp\bar{p}S$ Collider. RAL 87-037 (1987). Submitted to Zeitschrift fur Physik.

[35] D.Charlton et al., UA1 Technical Note UA1/TN 86-97.

[36] G.Arnison et al.(UA1 Collaboration), Lett. Nuovo Cimento, 44 (1985) 1.

See also:

C.Albajar et al.(UA1 Collaboration). Studies of the W and Z^0 properties at the CERN Proton-Antiproton Collider, paper in preparation.

[37] J.P.Revol. UA1 Technical Note UA1/TN/86-61.

[38] A.Ali,E.Pietarinen,B.Van Eijk. EUROJET, A Monte Carlo Program for Jet Simulation, CERN EP/85-121.

[39] C.Albajar et al.(UA1 Collaboration), Search for New Heavy Quarks at the CERN Proton-Antiproton Collider. CERN-EP/87-190. Submitted to Zeitschrift fur Physik.

[40] G.Arnison et al.(UA1 Collaboration), Phys. Lett., 123B (1983) 115.

[41] G.Arnison et al.(UA1 Collaboration), Phys. Lett., 132B (1983) 214.

[42] M.Della Negra. Heavy flavour production in μ + jet events and limits on the top mass, Talk given at the UA1 Physics Meeting, 20 May 1987.

[43] C.Albajar et al.(UA1 Collaboration), Phys. Lett., 185B (1987) 233.

[44] See for example, M.Althoff et al., (TASSO Collaboration), Phys. Lett., 138B (1984) 441.

[45] G.Hanson et al., Phys. Lett. Rev., 35 (1975) 1609.